# Multi-physics and Multilevel Fidelity Modeling and Analysis of Olympic Rowing Boat Dynamics

Andrea Mola

Dissertation submitted to Virginia Polytechnic Institute and State University
in partial fulfillment of the requirements for the degree of

Doctor of Philosophy
in
Engineering Mechanics

Muhammad R. Hajj, Chairman
Michael L. Madigan
Leigh S. McCue-Weil
Shane D. Ross
Mark A. Stremler

June 4, 2010
Blacksburg, Virginia

Keywords: Rowing Boats, Dynamics, Fluid Mechanics, Sensitivity Analysis

# Multi-physics and Multilevel Fidelity Modeling and Analysis of Olympic Rowing Boat Dynamics

Andrea Mola

(ABSTRACT)

A multidisciplinary approach for the modeling and analysis of the performance of Olympic rowing boats is presented. The goal is to establish methodologies and tools that would determine the effects of variations in applied forces and rowers motions and weights on mean surge speed and oscillatory boat motions. The coupling between the rowers motions with the hull and water forces is modeled with a system of equations. The water forces are computed using several fluid dynamic models that have different levels of accuracy and computational cost. These models include a solution of the Reynolds Averaged Navier–Stokes equations complemented by a Volume of Fluid method, a linearized 3D potential flow simulation and a 2D potential flow simulation that is based on the strip theory approximation. These results show that due to the elongated shape of the boat, the use of Sommerfeld truncation boundary condition does not yield the correct frequency dependence of the radiative coefficients. Thus, the radiative forces are not computed in the time-domain problem by means of a convolution integral, accounting for flow memory effects, but were computed assuming constant damping and added mass matrices. The results also show that accounting for memory effects significantly improves the agreement between the strip theory and the RANS predictions. Further improvements could be obtained by introducing corrections to account for longitudinal radiative forces, which are completely neglected in the strip theory.

The coupled dynamical system and the multi-fidelity fluid models of the water forces were then used to perform a sensitivity analysis of boat motions to variations in rowers weights, exerted forces and cadence of motion. The sensitivity analysis is based on the polynomial chaos expansion. The coefficients of each random basis in the polynomial chaos expansion are computed using a non-intrusive strategy. Sampling, quadrature, and linear regression methods have been used to obtain the these coefficients from the outputs generated by the system at each sampling point. The results show that the linear regression method provides a

very good approximation of the PCE coefficients. In addition, the number of samples needed for the expansion, does not grow exponentially with the number of varying input parameters. For this reason, this method has been selected for performing the sensitivity analysis.

The sensitivity of output parameters to variations in selected input parameters of the system are obtained by taking the derivatives of the expansion with respect to each input parameter. Three test cases are considered: a light-weight female single scull, a male quad scull, and a male coxless four. For all of these cases, results that relate the effects of variations in rowers weights, amplitudes of exerted forces and cadence of rowing on mean boat speed and energy ratio, defined as the ratio of kinetic energy of the forward motion to that of the oscillatory motions, are presented. These results should be useful in the design of rowing boats as well as in the training of rowers.

*I leave a white and turbid wake;*
*pale waters, paler cheeks, where'er I sail.*
*The envious billows sidelong*
*swell to whelm my track;*
*let them; but first I pass.*

– Herman Melville (*Moby Dick*)

# Acknowledgements

I would like to express my gratitude to my advisor Dr. Muhammad Hajj for offering me the opportunity to work with him in this department. His enthusiasm and optimism helped me in the years spent here, just as much as his careful and experienced guide helped me improving all the aspects of my research.

I would also like to thank the faculty members who served in my committee, Dr. Madigan, Dr. McCue, Dr. Ross and Dr. Stremler, for the interest they have shown in my research with their questions and precious advice. A particular recognition goes to Dr. McCue, as my research benefited from her knowledge on ship dynamics and from her many suggestions.

I also want to express my admiration and gratitude to Dr. Ali Nayfeh. Many concepts and theories learned in his courses were very useful in this dissertation, and will be even more useful in my professional career.

A special mention goes to all the people in Politecnico di Milano who helped me and supported me in these years. Among the others, particular acknowledgment go to my Italian PhD advisor, Luca Formaggia, for the freedom and the support I constantly enjoyed while working with him, and Nicola Parolini, for the priceless help given me in these years.

I want to thank Alessandro Placido of Filippi Lido s.r.l., producer of competition rowing boats, for the help and for the data on the boats geometry provided us. I am also very grateful to Laura Milani, lightweight single scull vice World Champion, who contributed to the validation of the rowing boat model in the framework of her Bachelor Degree final project in Politecnico di Milano, and that helped us setting up the simulations discussed with realistic values of world class athletes.

My gratitude goes also to all the people who contributed to my work with suggestions and

data: the team of Chiarella Sforza at Università Statale di Milano, for the availability of the rowers motion experimental data; Edie Miglio, Luca Del Grosso and Antonio Montano, for the early development of the dynamical model and of the C++ software; Matteo Pischiutta, for his help with the RANS model simulation; Enric Xargay and Chris Mesrobian for their precious suggestions on the rowers control and rudder modeling respectively; Mehdi Ghommem for having introduced me to the polynomial chaos expansion, and for contributing to my work with many important suggestions and interesting discussions.

I need to thank all my colleagues at the Department of Engineering Science and Mechanics, in particular my office mates Giovanni Sansavini, Giancarlo Bordonaro, Giulio Romanelli and Abdessattar Abdelkefi. Through many conversations and hours spent together, they helped me solving problems and improving my work. For this, and for their friendship, I am most thankful.

I also thank all the staff members of the Department of Engineering Science and Mechanics. In particular, I want to acknowledge Lisa Smith, for the precious help given me me with paperwork and beureaucracy and Tim Tomlin, who helped me in the setup of the simulations on the Linux Cluster of the Department.

Finally, but most importantly, I owe a big thank you to my family, for the love, the serenity and the support that I could always find at home during these years.

# Contents

# List of Figures

# List of Tables

# Chapter 1

# Introduction

## 1.1 Motivation for study of rowing boats

Rowing is a sport with a long tradition, where best performance is based on athletic gestures and boat shapes and elements configurations. The boats are narrow and long with nearly semicircular cross sections designed to reduce drag to a minimum. The shells are usually made of carbon-fiber reinforced materials to increase the stiffness and reduce the weight. In rowing configurations (see Fig. 1.1), the rowers sit in the boat facing backwards (towards the stern). They use oars that are attached to the boat at pinned points (oarlocks) to propel the boat forward (in the direction of the bow). The oarlocks are held from outriggers away from the hull; thereby, reducing its cross sectional area. By sitting on sliding seats, the rowers are able to apply more power to the oars and increase the distance they can pull with each stroke. Furthermore, by using their legs to slide along the seat rails, they add their leg power to the stroke. Clearly, rowing involves coupled complex dynamics that span across many fields including fluid dynamics, rigid body dynamics, and biomechanics.

Developments over the past decades in the fields of composite materials, geometric modeling and computing power and methodologies have contributed to improving the design of rowing boats. More recently, rowing athletes and coaches started to consider with growing interest muscoloskeletal mechanics as a part of the training process to improve overall performance (4; 5). While advancements made in individual fields can contribute to performance enhancement of rowing boats, the multidisciplinary nature of rowing necessitates the devel-

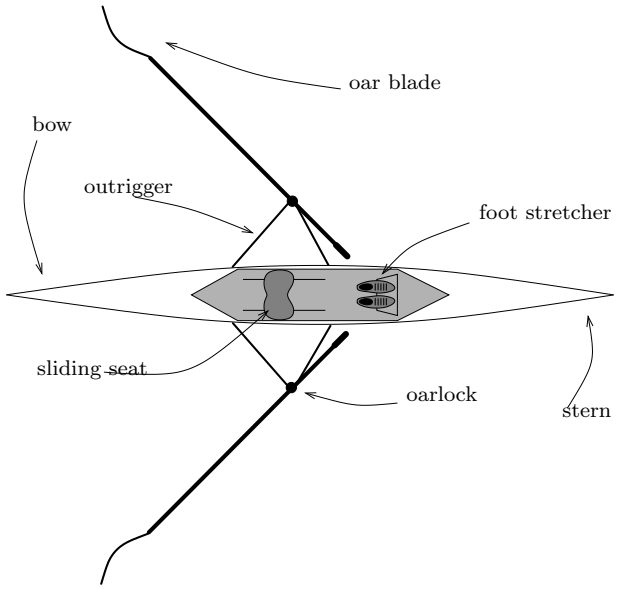


Figure 1.1: A single scull with its main components.

opment of modeling and analysis tools that couple the different disciplines and would be used to optimize the boat and rowers performance.

For determining hydrodynamic forces of steady state (primary) flows around boats moving at constant speeds, there exist nowadays well established design tools. However, the varying forces at the oars and, more importantly, inertial forces due to the movement of the rowers, superimpose complex secondary motions to the primary one, which, to a first approximation, may be considered periodic. These secondary motions induce additional drag mainly due to generated gravity waves, which radiate from the boat and dissipate energy. As such, it is not possible to conclude that a hull shape optimized under steady state flow assumptions, would be optimal when considering secondary motions. Furthermore, conditions for a rower's best performance on a rowing machine are not the same conditions of a race, where more complex dynamics are involved. These arguments motivate the development of multi-fidelity models that account for the coupled complex dynamics of rowing boats and address sensitivity of their motions to amplitudes and frequencies of oarlock forces as exerted by the rowers, the rowers weights and motions, and other input parameters.

## 1.2 Multi-physics modeling of rowing boats

Since the early works of F.H. Alexander (6), the topic of rowing boats dynamics has been widely investigated, although most of the reports produced so far have been published only on the world wide web. Some of the most interesting contributions are those by W.C. Atkinson (7), A. Dudhia (8) and M. van Holst (9). In (10), L. Lazauskas provides a rather complete mathematical model for boat dynamics. However, in all of these studies, the focus has been on horizontal forward motions only. Dissipative effects were modeled using empirical relations. Contributions of the vertical (heaving) and lateral (sway) motions and angular rotations of the boat were neglected. A few essays on stroke dynamics have been published in the context of the design of rowing machines. Of particular interest are the works of Elliott et al. (11), and Rekers (12), whose aim was to try to reproduce realistic rowing motions in indoor rowing machines. Again, only the horizontal motions were considered.

A rowing boat dynamics model accounting for the full three dimensional rowing boat motions is used in this work. A schematic of the different aspects of this model is presented in Fig. 1.2. The properties (mass and inertia) of the rowing boat are determined by the boat material and geometry and by the rowers positions and weights. The forcing terms in the equations of motions include forces applied at the oarlocks and the rowers motions. The hydrodynamic and hydrostatic (water) forces are computed by solving the fluid dynamic governing equations around the boat hull. With different approximations, one could use different approaches to determine these forces.

Given the high Reynolds numbers and turbulent regimes characterizing flows around and behind the boat, numerical models that are based on solving the Navier–Stokes equations, such as Direct Numerical Simulations (DNS), Large Eddy Simulations (LES) or Reynolds Averaged Navier–Stokes (RANS) equations may be the most suitable. In particular, the latter model may be the most preferred option to perform high fidelity simulations, as it represents a good balance between computational costs and needed level of details. Still, due to the required large number of degrees of freedom, such simulations have a very high computational cost. This cost hinders the implementation of any sensitivity analysis whereby the influence of variations in input parameters on forward speed and overall efficiency or

performance could be assessed.

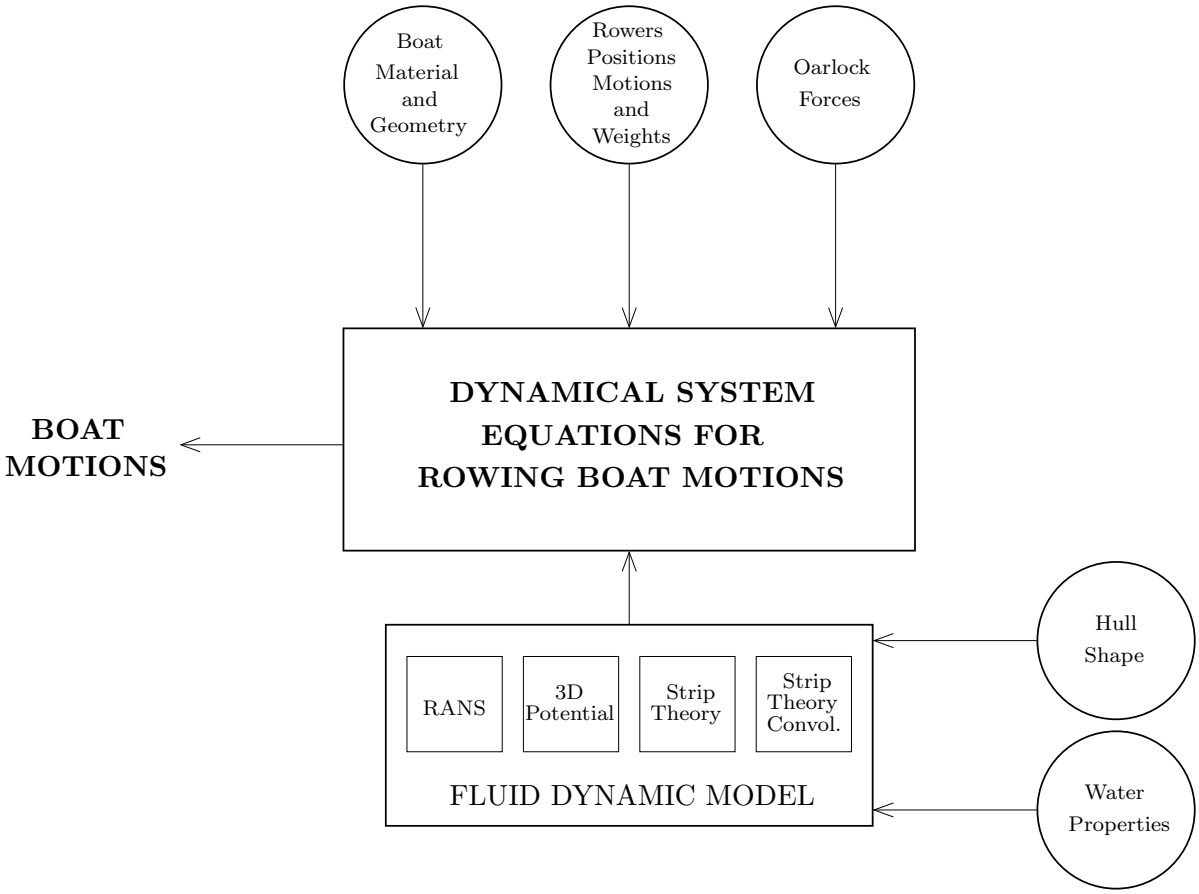


Figure 1.2: Multi-physics representation and modeling of rowing boat dynamics.

Low fidelity simulations that are based on reduced-order fluid dynamic models can be used as an assessment tool in the preliminary design stages of racing boats. Furthermore, if it incorporates the rowers motions with sufficient details, a reduced-order model could be used by trainers to understand the effects of different rowing styles or crew compositions. In this work, a reduced-order model, based on the irrotational flow assumption and velocity potential, is obtained by linearization of the free surface boundary conditions applied at the water free surface. In a linear framework, the flow potential is conveniently decomposed into its contributions due to the boat mean (primary) and oscillatory (secondary) motions.

For the sake of computational efficiency, the effects of shape, wave and viscous drag, due to the mean motion of the boat, are simulated by standard algebraic equations. As for the secondary motion effects, the hydrostatic forces, which depend on the wetted surface, are dynamically computed, while the dissipative effects of waves generated by the secondary motions are computed by solving a linear radiation problem which results in damping and added mass matrices to be introduced into the dynamical model. The radiation matrices are obtained using two different approaches. In the first approach the three-dimensional radiative potential equations are solved (13) while applying a far field Sommerfeld condition on the truncation boundary of the domain. In the second approach, the strip theory (14), which makes use of the assumption of a slender body, is used. The three-dimensional potential problem is decomposed into a set of two-dimensional radiation problems resulting in a lower computational cost. The damping and added mass matrices obtained depend on the boat frequency of oscillation of the boat, and are introduced in the time-dependent rowing boat motion equations, by means of a convolution integral. However, assuming that the boat motions are dominated by the frequency of the rowers action, the waves radiation forces can be obtained by adding constant damping and added mass coefficients to the time domain system. Both strategies are considered and implemented in this work.

## 1.3 Objectives and methods

The overall goal of this work is to establish methodologies and tools for modeling and analysis of rowing boat motions. Particularly, the interest is in tools that would determine variations in mean surge and oscillatory motions to small variations in magnitude and frequencies of applied forces, or in the boat geometry. Such tools could be used by trainers to understand the effects of different rowing techniques or crew compositions, and by boat designers, to evaluate the performance of new hull shapes.

The complexities involved in high fidelity modeling of rowing boat motions lead to high computational cost that necessitate the multi-level modeling and validation. As such, the first objective is to compare the results of simulations of rowing boat motions that are performed with different fluid dynamic models. Particularly, the performance of the low fidelity

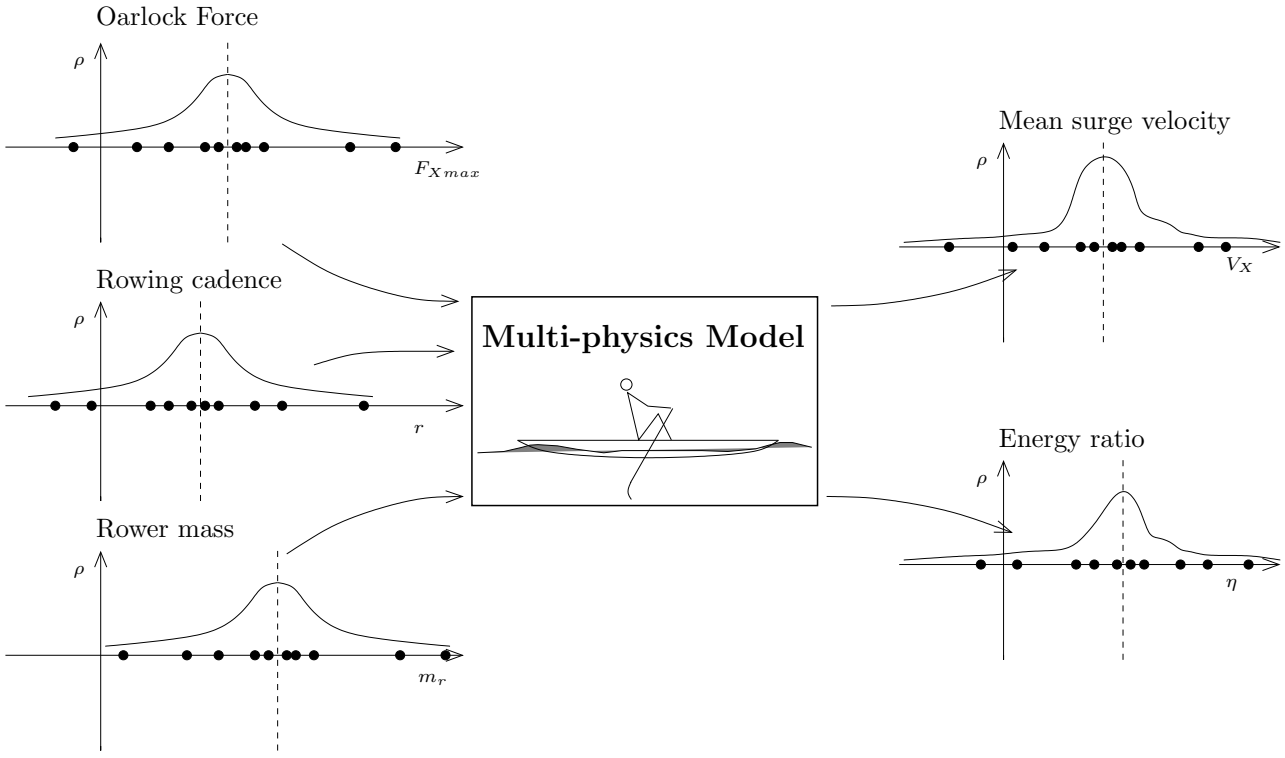


Figure 1.3: A representation of the sensitivity analysis applied to the rowing boat dynamical system. First, the input parameters are varied following a Gaussian distribution. The rates of variation of the output parameters distribution to variations in input parameters are used to quantify the system sensitivities.

reduced-order models is assessed against those of high fidelity ones. The second objective is to apply different sensitivity analysis tools to the model of rowing boat dynamics to determine variations in mean surge and oscillatory motions to small variations in input parameters, such as magnitude and frequencies of applied forces or rowers weights and size. The sensitivity analysis is carried out by means of a non-intrusive polynomial chaos technique. First, variations are introduced in input parameters such as rowers weight, forces, and frequency of motion, and propagated through the reduced-order model dynamical system (see Fig. 1.3). Then, the rates of variations of output parameters such as the mean forward velocity or energy ratio of the rowing action with variations in input parameters are determined.

Due to the number of simulations required, the sensitivity analysis is more conveniently applied to the reduced-order fluid dynamic models, which simulate a rowing race in minutes. Thus, a final objective is to compare the sensitivity analysis results obtained by implementing a reduced-order fluid dynamic model with those obtained when implementing the high fidelity model. This cross validation is performed on a simple benchmark case in which variations are introduced only to few parameters, and a low the number of realizations is needed for the sensitivity analysis. Yet, the results obtained will help in determining if trends indicated by the low fidelity model are correct and help assessing the level of confidence in the sensitivity analysis performed with the reduced order models.

# Chapter 2

# Multi-physics modeling of rowing boat dynamics

In rowing boats (see Fig. 1.1), the rowers sit in the central part of a slender hull with their back pointing towards the advancing direction of the boat. The seats slide on rails, whereas the rowers feet are secured to foot stretchers (or footboards). The oars are linked to the hull by means of oarlocks mounted on lateral supports named outriggers (or just riggers). The two most common types of rowing boats, which reflect the two major rowing techniques, include sweep rowing and sculling. In sweep boats each rower has one oar, and holds it with both hands. Left and right hand rowers are sitting on the boat in an alternate fashion. In a scull, each rower uses two oars (left and right), moving them synchronously. Sometimes shells have a coxswain, that is a person who steers the shell using a small rudder and urges the rowers on.

The rowing boat dynamics model that has been developed and is described in this chapter is completely general. This model can simulate the dynamics of rowing boats of any desired class. The output consists of full three dimensional motions of the boat. The model can consider both sweep rowing and sculling. It can also account for the presence of a coxswain, and consider any number of rowers, with any weight and height, and rowing with different forces and paces. Finally, the model can account for different boat geometries and hull shapes. In this chapter, the equations describing the model will be are presented. Details on

the modeling of the rowers inertial, oar and control forces are given. Further details on the derivation of the model equations can be found in (15), in which the first 2D version of the model is presented, and in (16; 17), where the full three dimensional version of the model is described.

## 2.1 The boat and rowers dynamical system

In the boat dynamical model, the hull is treated as a rigid body of known mass and angular inertia. The goal of the simulations is to compute the motions of the hull in all six degrees of freedom, *i.e.*: the translations in the surge, sway, and heave directions, and the yaw, pitch and roll Euler angles. The rowers (whose mass is always larger than that of the hull) are represented by a set of point masses corresponding to their main body parts, which move according to motion laws that are specified in the local reference frame of the boat. The last component of the dynamical system is that of the oars, which are assumed to act as perfect levers and have negligible masses. Under such assumption, the forces at handles, oarlocks and oar blades only differ by scaling factors depending on the oar geometry. The oarlocks are represented as perfect spherical joints.

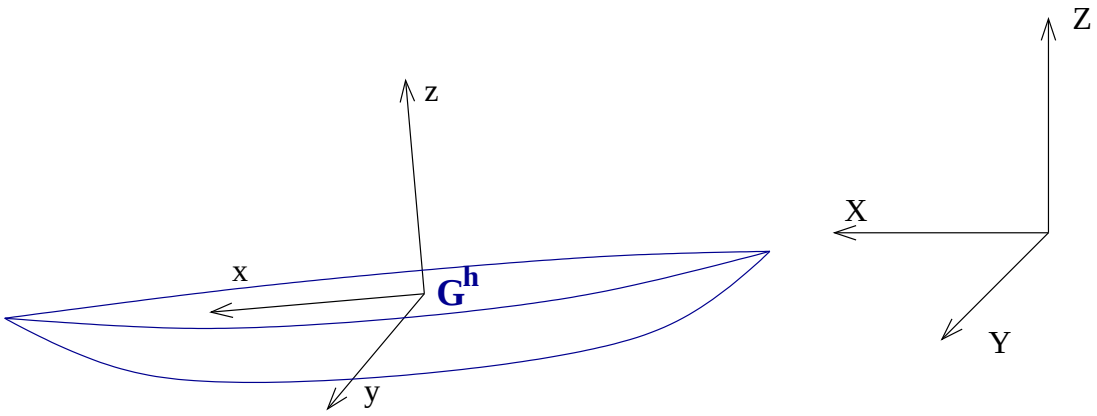


Figure 2.1: Rowing boat with relevant reference frames. The hull reference system is centered at hull center of mass.

In modeling the dynamics of the rowing boat, we start from an accurate geometrical description; more precisely, the actual values for footboards, seats and oarlocks positions, oars

lengths, etc. The boat motions are conveniently described in an inertial frame of reference $(\mathbf{O}; X, Y, Z)$. This system, as illustrated in Fig. 2.1, is fixed with the race field and is denoted with the unit vectors $\mathbf{e}_X$, $\mathbf{e}_Y$ and $\mathbf{e}_Z$. We refer to it as the *absolute* reference. The $X$ axis is horizontal, parallel to the undisturbed water free surface, and oriented along the direction of progression of the boat. The $Z$ axis is vertical and pointing upwards, while $\mathbf{e}_Y = \mathbf{e}_Z \times \mathbf{e}_X$. By convention, the origin $\mathbf{O}$ is set at the starting point of the race and the undisturbed water free surface is placed at the constant value $Z = 0$. A second reference system is attached to the boat and is referred to as the *hull coordinate system*, $(\mathbf{G}^h; x, y, z)$). The axes of this system, whose unit vectors are $\mathbf{e}_x$, $\mathbf{e}_y$ and $\mathbf{e}_z$, are defined so that $\mathbf{e}_x$ and $\mathbf{e}_z$ identify the hull symmetry plane with $\mathbf{e}_x$ directed from stern to bow, $\mathbf{e}_z$ directed from bottom to top, and $\mathbf{e}_y = \mathbf{e}_z \times \mathbf{e}_x$. It should be noted that the hull reference system is centered in the hull center of mass $\mathbf{G}^h$ and not in the center of mass arising from hull and rowers system composition; the latter being not fixed due to the rowers motions. Points in the absolute reference are here indicated with uppercase letters, while the lowercase letters indicate points in the hull reference frame. The Euler angles $\psi$, $\theta$, $\phi$ allow for the transformation of vectors from the absolute reference frame to the hull frame, by means of the rotation matrix $\mathcal{R}(\psi, \theta, \phi)$ (18). With the conventions used, the yaw angle $\psi$ is positive if the bow of the boat moves towards left, while the pitch angle $\theta$ is positive when the bow moves downwards; finally, a positive roll angle $\phi$ results in a lift of the left side of the boat.

To account for the inertial forces that are caused by the rowers periodic displacements, each rower body is decomposed into $p = 12$ parts of known masses, as illustrated in Fig. 2.2. The motions of these masses —in the hull reference frame— is imposed, with a set of parametric curves obtained from fitting experimental data (16). The use of inverse dynamics allows for the computation of a set of inertial terms in the system equations representing transport, centrifugal and Coriolis accelerations for each of the body parts. We also assume that the oar is a rigid and weightless lever of length $L$, and that the distance between the rowers hands and the oarlock $r_h$ is constant. Under these assumptions, the translation vector $\mathbf{G}^h$ and angular velocity $\boldsymbol{\omega}$ of the boat hull, are governed by the following system of ordinary differential equations (see (16) for the full derivation)

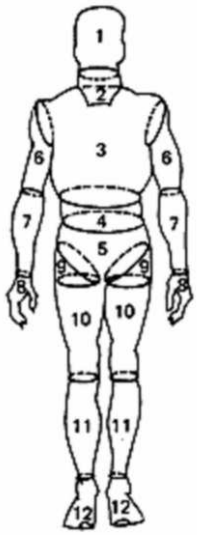


Figure 2.2: The 12 anatomical parts used to subdivide the body mass.

$$
\begin{aligned}
M_{Tot}\ddot{\mathbf{G}}^h + \dot{\boldsymbol{\omega}} \times \sum_{i,j} m_{ij}\mathcal{R}^T\boldsymbol{x}_{ij} &= \frac{r_h}{L}\sum_j(\boldsymbol{F}_{ol_j} + \boldsymbol{F}_{or_j}) - \sum_{i,j} m_{ij}\mathcal{R}^T\ddot{\boldsymbol{x}}_{ij} - \sum_{i,j} m_{ij}\boldsymbol{\omega}\times\boldsymbol{\omega}\times\mathcal{R}^T\boldsymbol{x}_{ij} \\
&- \sum_{i,j} m_{ij} 2\boldsymbol{\omega}\times\mathcal{R}^T\dot{\boldsymbol{x}}_{ij} + M_{Tot}\boldsymbol{g} + \mathbf{F}^w \qquad (2.1a) \\
\sum_{i,j} m_{ij}\mathcal{R}^T\boldsymbol{x}_{ij}\times\ddot{\mathbf{G}}^h + \mathcal{R}I_G\mathcal{R}^{-1}\dot{\boldsymbol{\omega}} &+ \sum_{i,j} m_{ij}\mathcal{R}^T\boldsymbol{x}_{ij}\times\dot{\boldsymbol{\omega}}\times\mathcal{R}^T\boldsymbol{x}_{ij} = -\boldsymbol{\omega}\times\mathcal{R}I_G\mathcal{R}^{-1}\boldsymbol{\omega} \\
&- \sum_{i,j} m_{ij}\mathcal{R}^T\boldsymbol{x}_{ij}\times\mathcal{R}^T\ddot{\boldsymbol{x}}_{ij} - \sum_{i,j} m_{ij}\mathcal{R}^T\boldsymbol{x}_{ij}\times\boldsymbol{\omega}\times\boldsymbol{\omega}\times\mathcal{R}^T\boldsymbol{x}_{ij} \\
&- \sum_{i,j} m_{ij}\mathcal{R}^T\boldsymbol{x}_{ij}\times 2\boldsymbol{\omega}\times\mathcal{R}^T\dot{\boldsymbol{x}}_{ij} + \sum_{i,j}\mathcal{R}^T\boldsymbol{x}_{ij}\times m_{ij}\boldsymbol{g} + \mathbf{M}^w \\
&+ \sum_j\left[\left(\boldsymbol{X}_{ol_j} - \mathbf{G}^h\right) - \frac{L-r_h}{L}\left(\boldsymbol{X}_{hl_j} - \mathbf{G}^h\right)\right]\times\boldsymbol{F}_{ol_j} \\
&+ \sum_j\left[\left(\boldsymbol{X}_{or_j} - \mathbf{G}^h\right) - \frac{L-r_h}{L}\left(\boldsymbol{X}_{hr_j} - \mathbf{G}^h\right)\right]\times\boldsymbol{F}_{or_j} \qquad (2.1b)
\end{aligned}
$$

where $m_{ij}$ denotes the mass of body part $j$ of rower $i$, $M_{Tot}$ is the total mass of rowers and hull, and $I_G$ is the matrix of inertia of hull. The indices $i$ and $j$ in $\sum_{i,j}$ vary from 1 to $p$ and 1 to the number of rowers $n$, respectively. We point out that a coxswain can be represented in this model as a pointwise mass fixed to the hull, which adds to $M_{Tot}$ and modifies the hull matrix of inertia $I_G$.

To close equations (2.1), one needs to model the time law for the motions of the rowers body parts, $\boldsymbol{x}_{ij}(t)$, the left and right oarlock forces, $\boldsymbol{F}_{ol_j}$ and $\boldsymbol{F}_{or_j}$ respectively, and the water forces and momenta, $\mathbf{F}^w$ and $\mathbf{M}^w$ respectively. The modeling of these quantities is discussed next.

## 2.2 Modeling of rowers motions

As mentioned, we represent the mass distribution of an athlete of given characteristics (weight, gender, height) by subdividing the body into the $p = 12$ parts illustrated in Fig. 2.2. We infer the masses $m_{ij}$ from anthropometric tables taken from (19). Each part is then considered as concentrated in its own center of mass $\mathbf{x}_{ij}$, i.e. we neglect the angular inertia. The motions of each center of mass is obtained from the analysis of experimental data made available by the group of Prof.ssa Chiarella Sforza, of Dipartimento di Morfologia Umana, in Università statale di Milano. In these experiments, passive light-reflecting markers were applied on an athlete's body, in correspondence to the main articulations. The athlete was then filmed by a set of digital cameras while rowing on a rowing machine. The position of the markers at any time $t$ can be reconstructed by triangulation from the images that the different cameras have recorded. More details on the recording technique may be found in (20).

A further step consists in reconstructing each marker's motion by means of special analytical functions. This procedure is not strictly needed for our mechanical model, but it gives the possibility to parametrize the rowers motion to analyze the effect of each parameter considered on the inertial forces, and it also allows to carry on time differentiation in a simple and computationally efficient way. As an example, Fig. 2.3 depicts the reconstruction of the wrist marker path and $x$ position time history.

Through the use of the standard human anthropometric model (19), it is possible to reconstruct, from the marker trajectory, the law of motion of the center of mass of each body part, i.e. the $\mathbf{x}_{ij}$, $\dot{\mathbf{x}}_{ij}$ and $\ddot{\mathbf{x}}_{ij}$ needed in equation (2.1). The position of the barycenter of each body part is obtained by means of interpolation and extrapolation of the reconstructed marker positions.

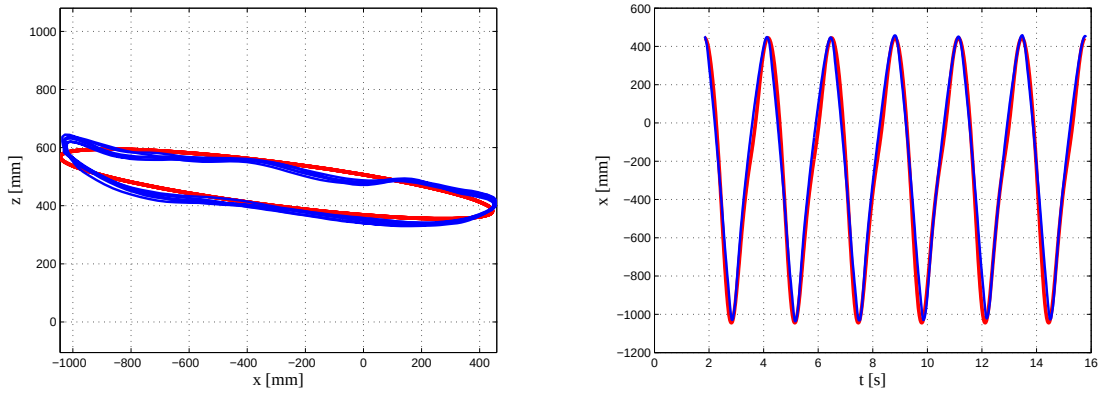


a) b)

Figure 2.3: Measured (—) and reconstructed (—) motion of the wrist marker. Plot a) represents the marker path in the rower's sagittal plane. Plot b) shows the time history of the $x$ component of the marker displacement .

## 2.3 Modeling of oar forces

The oarlock forces are relatively easy to measure, and experimental data are available in the literature (21). Here, the horizontal component of the oarlock force is modeled by (see Fig. 2.4)

$$f_X^{o^i} = \begin{cases} c_{3X}t^3 + c_{2X}t^2 + c_{1X}t + c_{0X} & \text{for} \quad 0 < t < \tau_a \\ k_{2X}t^2 + k_{1X}t + k_{0X} & \text{for} \quad \tau_a < t < T \end{cases} \tag{2.2}$$

where the $c_{iX}$ and $k_{iX}$ coefficients depend on the specific athletes maximum and minimum rowing force, $F_{Xmax}$ and $F_{Xmin}$ respectively, and on the active phase of the stroke length $\tau_a$. The vertical component of the oarlock force, is modeled using the same functions, and the corresponding $c_{iZ}$ and $k_{iZ}$ coefficients are determined by the specified values of $F_{Zmax}$ and $F_{Zmin}$.

## 2.4 Modeling of rowers active control

The three dimensional rowing boat dynamics model described above is inherently unstable. If we consider the free body diagram for the roll degree of freedom presented in Fig. 2.5, we

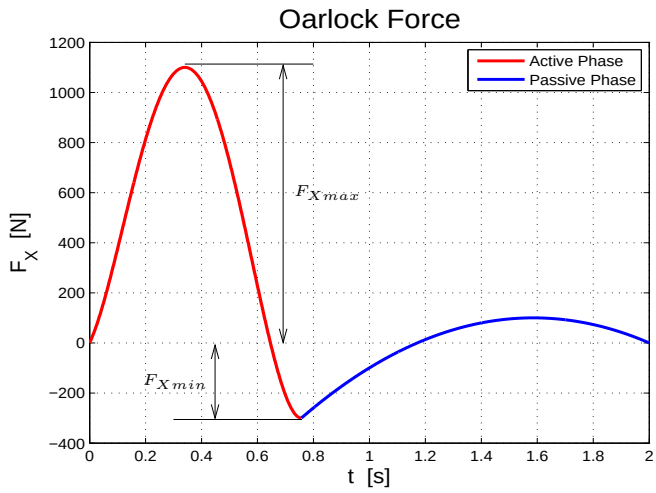


Figure 2.4: Time history of the oarlock force horizontal component. The red portion represents the force exerted by the rower during the active phase of the stroke. The blue portion represents the force exerted during the recovery phase.

note that, for these boats the hydrostatic buoyancy force is applied in a pressure center which is lower than the boat gravity center. The resulting torque grows as the roll angle increases, and makes the roll motion of the boat unstable. In addition, possible non-symmetric oarlock forces (typical of sweep boats) might increase this instability. Conversely, due to the lack of a yaw component in the hydrostatic force, the equilibrium about this degree of freedom is indifferent (see Fig. 2.6 ). Thus, if non-symmetric forces are applied at the oarlocks, the resulting torque will not be countered by any restoring term, and the boat will rotate, moving in a direction which adds to the distance from the finish line.

During their rowing action, the athletes constantly apply an active control to the boat, in order to stabilize the roll motion and keep the boat moving straight towards the finish line. In the following sections, we will illustrate how these controls are represented in the rowing boat model.

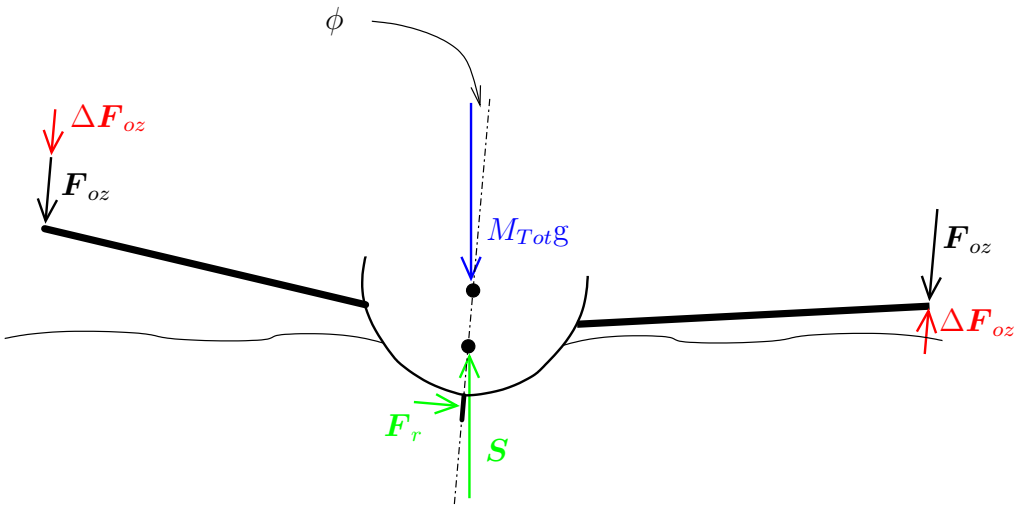


Figure 2.5: A front view of the boat with the vertical forces applied to the hull. The control forces on the hull are indicated by the red color.

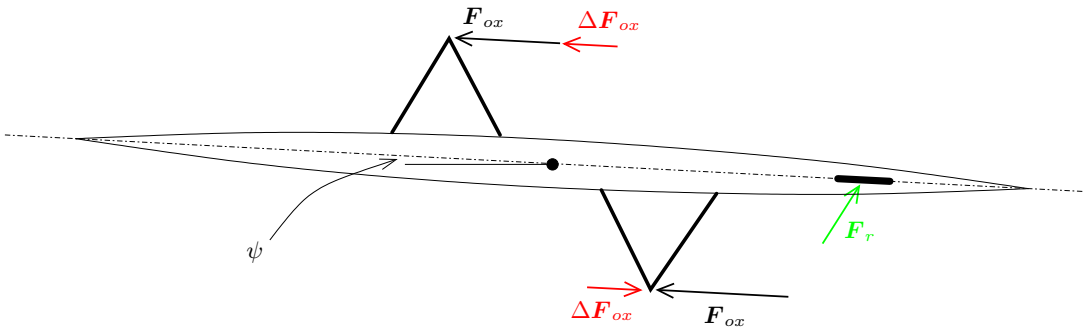


Figure 2.6: A top view of the boat with the longitudinal forces applied to the hull. The control forces on the hull are indicated by the red color.

### 2.4.1 The roll control

As illustrated in Fig. 2.5, we assume that the rowers keep the boat in the equilibrium position by exerting opposite vertical forces on the left and right oarlocks. These forces produce a restoring moment which stabilizes the boat whenever it is not perfectly vertical. This action is modeled by letting the restoring oarlock forces be proportional to the roll angle; *i.e.*:

$$\Delta \boldsymbol{F}_{oz} = \pm k_{\text{Roll}} \phi,$$

where $k_{\text{Roll}}$ is the gain coefficient of the roll proportional control. The oarlock forces needed to keep the boat vertical are usually small. The rowers generate them by moving slightly up or down the oar handles. As such, this control is acting also during the recovery phase of the stroke, when the oars are not in the water.

### 2.4.2 The yaw control

The control of the yaw degree of freedom is usually achieved by a rudder placed towards the stern of the hull. This small fin is usually a flat plate characterized by a surface area $S_r$ and an aspect ratio $\lambda_r$. The force due to such submerged appendage is a part of the fluid dynamic forces $\mathbf{F}^w$ in equation (2.1) but, due to its importance for the boat control, we will describe its modeling in the present section.

The drag and lift coefficients of the rudder are written as (22)

$$C_{Lr} = 2\pi \frac{|\alpha_r|}{1 + 1/(\lambda_r)}, \qquad C_{Dr} = \frac{{C_{Lr}}^2}{2\lambda_r},$$

where the rudder angle of attack $\alpha_r$ is given by

$$\alpha_r = -\psi + \arcsin\left(\frac{\dot{G}_y^h - \omega_x d_z + \omega_z d_x}{|\dot{\mathbf{G}}^h|}\right).$$

Here, $d_x$ and $d_z$ are respectively the longitudinal and vertical distances between the rudder pressure center and the hull center of gravity.

The rudder force in the relative reference frame is written as

$$\boldsymbol{f}_r = \frac{1}{2}\rho_w |\dot{\mathbf{G}}^h|^2 S_r \left\{ \begin{array}{c} (-C_{Dr}\cos\alpha_r + C_{Lr}|\sin\alpha_r|) \\ \frac{\alpha_r}{|\alpha_r|}\left(C_{Lr}\cos\alpha_r + C_{Dr}|\sin\alpha_r|\right) \\ 0 \end{array} \right\}$$

It is important to note that this force acts as a (non linear) damper for the yaw motion. Nevertheless, it does not provide the restoring force that is needed to keep the boat moving straight towards the finish line. During a race, such a restoring force is provided by the rowers, who modulate their oar forces on the right and left side of the boat in order to prevent it from progressively turning sideways.

In our model, we consider that the yaw control is only active during the active phase of the stroke. At the beginning of each stroke, the rower evaluates the instantaneous yaw angle $\psi_0$ and modulates the longitudinal maximum force of the stroke according to

$$F_{x\,C}^{max} = F_x^{max} \pm \Delta F_x^{max} = F_x^{max} \pm k_{\mathrm{Yaw}}\psi_0,$$

where $k_{\mathrm{Yaw}}$ is the gain coefficient of the yaw control.

The resulting controlled longitudinal force at the oarlock is given by

$$f_x^{o^i} = (F_x^{max} \pm k_{\mathrm{Yaw}}\psi_0)\sin\left(\frac{\pi t}{\tau_a}\right).$$

The assumption that the rowers decide at the beginning of each stroke how to control the boat yaw is based on the fact that for the rowers it is very difficult to modulate the strength of the stroke during the active phase, as the latter is usually a short and intense pulling motion. On the other hand, they can exploit the recovery phase to decide how to adjust the strength of the next stroke in order to keep the boat moving in the right direction.

## 2.5 Time advancing scheme

Boat motions are obtained by numerically solving the system of Equations (2.1). To obtain a numerical solution, this system is modified as a system of first-order ordinary differential equations. To do so, we first express the cross products on the left hand side of system (2.1) in a matrix form. For that, we define the following skew-symmetric matrices

$$A = -\sum_{i,j} m_{ij} \begin{bmatrix} 0 & -v_{ij\ 3} & v_{ij\ 2} \\ v_{ij\ 3} & 0 & -v_{ij\ 1} \\ -v_{ij\ 2} & v_{ij\ 1} & 0 \end{bmatrix}, \quad B = -\sum_{i,j} m_{ij} \begin{bmatrix} 0 & -v_{ij\ 3} & v_{ij\ 2} \\ v_{ij\ 3} & 0 & -v_{ij\ 1} \\ -v_{ij\ 2} & v_{ij\ 1} & 0 \end{bmatrix}^2$$

where

$$\boldsymbol{v}_{ij} = \mathcal{R}^T \boldsymbol{x}_{ij}.$$

We then write

$$\mathcal{M}(t) = \begin{bmatrix} M_{Tot} I & A \\ -A & \mathcal{R} I_G \mathcal{R}^{-1} + B \end{bmatrix}$$

where $I$ is the identity matrix of order 3. The right hand side of system (2.1) is then written in vector form as $\boldsymbol{f} = \boldsymbol{f}^i + \boldsymbol{f}^w$, where

$$\boldsymbol{f}^i(\dot{\mathbf{G}}^h, \mathbf{G}^h, \boldsymbol{\omega}) = \left\{ \begin{array}{l} \frac{r_h}{L} \sum_j \boldsymbol{F}_{o_j} - \sum_{i,j} m_{ij} \mathcal{R}^T \ddot{\boldsymbol{x}}_{ij} - \sum_{i,j} m_{ij} \boldsymbol{\omega} \times \boldsymbol{\omega} \times \mathcal{R}^T \boldsymbol{x}_{ij} \\ - \sum_{i,j} m_{ij} 2\boldsymbol{\omega} \times \mathcal{R}^T \dot{\boldsymbol{x}}_{ij} + M_{Tot} \boldsymbol{g} \\ \\ - \boldsymbol{\omega} \times \mathcal{R} I_G \mathcal{R}^{-1} \boldsymbol{\omega} - \sum_{i,j} m_{ij} \mathcal{R}^T \boldsymbol{x}_{ij} \times \mathcal{R}^T \ddot{\boldsymbol{x}}_{ij} \\ - \sum_{i,j} m_{ij} \mathcal{R}^T \boldsymbol{x}_{ij} \times \boldsymbol{\omega} \times \boldsymbol{\omega} \mathcal{R}^T \boldsymbol{x}_{ij} \\ - \sum_{i,j} m_{ij} \mathcal{R}^T \boldsymbol{x}_{ij} \times 2\boldsymbol{\omega} \times \mathcal{R}^T \dot{\boldsymbol{x}}_{ij} + \sum_{i,j} \mathcal{R}^T \boldsymbol{x}_{ij} \times m_{ij} \boldsymbol{g} \\ + \sum_j \left[ \left( \boldsymbol{X}_{o_j} - \mathbf{G}^h \right) - \frac{L - r_h}{L} \left( \boldsymbol{X}_{h_j} - \mathbf{G}^h \right) \right] \times \boldsymbol{F}_{o_j} \end{array} \right\}. \tag{2.3}$$

and

$$\boldsymbol{f}^w = \left\{ \begin{array}{c} \boldsymbol{F}^m \\ \boldsymbol{M}^m \end{array} \right\} + \mathcal{S}^s \boldsymbol{u}$$

where $\boldsymbol{u} = \left\{ \begin{array}{c} \dot{\mathbf{G}}^h \\ \boldsymbol{\omega} \end{array} \right\}$. The system of Equations (2.1) is then recast in the following form

$$\left( \mathcal{M}(t) + \mathcal{M}^s \right) \dot{\boldsymbol{u}} = \boldsymbol{f}(\boldsymbol{u}, t).$$

This system is further modified to obtain a first order non-linear ODE system that is more amenable for a numerical solution. Defining

$$M(t) = \begin{bmatrix} [I] & 0 \\ 0 & [\mathcal{M}(t) + \mathcal{M}^s] \end{bmatrix}, \qquad \boldsymbol{y} = \begin{Bmatrix} \mathbf{G}^h \\ \boldsymbol{u} \end{Bmatrix}, \qquad \boldsymbol{F}(\boldsymbol{y}, t) = \begin{Bmatrix} \dot{\mathbf{G}}^h \\ \boldsymbol{f} \end{Bmatrix}$$

we can finally write the system

$$\dot{\boldsymbol{y}} = (M(t))^{-1} \boldsymbol{F}(\boldsymbol{y}, t). \tag{2.4}$$

which is solved by means of a Runge–Kutta–Fehlberg 45 time advancing scheme (23).

For each time step, it is necessary to compute the rotation matrix $\mathcal{R}$ appearing in the motion equations, that is needed to deform the mesh used in the computation of the hydrostatic forces. To do this, the rotation matrix $\mathcal{R}$ is employed, once the unit vectors describing the orientation of the hull at the new time step $n+1$ are obtained by means of the Crank–Nicolson method, namely

$$\begin{aligned} \boldsymbol{e}_{x_{n+1}} &= \boldsymbol{e}_{x_n} + \frac{\Delta t}{2}(\omega_{n+1} + \omega_n) \times \boldsymbol{e}_{x_n} \\ \boldsymbol{e}_{y_{n+1}} &= \boldsymbol{e}_{y_n} + \frac{\Delta t}{2}(\omega_{n+1} + \omega_n) \times \boldsymbol{e}_{y_n} \\ \boldsymbol{e}_{z_{n+1}} &= \boldsymbol{e}_{x_{n+1}} \times \boldsymbol{e}_{y_{n+1}}. \end{aligned}$$

Finally, it is also useful to compute the three Euler angles, for monitoring the boat motions. This is done using the following equations

$$\begin{aligned} \psi_{n+1} &= \arcsin\left((\boldsymbol{e}_X \times \boldsymbol{e}_{x\ aux}) \cdot \boldsymbol{e}_Z\right) \\ \theta_{n+1} &= \arcsin\left((\boldsymbol{e}_{x\ aux} \times \boldsymbol{e}_{x_{n+1}}) \cdot \boldsymbol{e}_{y\ aux}\right) \\ \phi_{n+1} &= \arcsin\left((\boldsymbol{e}_{y\ aux} \times \boldsymbol{e}_{y_{n+1}}) \cdot \boldsymbol{e}_{x_{n+1}}\right). \end{aligned}$$

where the auxiliary unit vectors are given by

$$\begin{aligned} \boldsymbol{e}_{x\ aux} &= \frac{\boldsymbol{e}_{x_{n+1}} - (\boldsymbol{e}_{x_{n+1}} \cdot \boldsymbol{e}_Z)\boldsymbol{e}_Z}{|\boldsymbol{e}_{x_{n+1}} - (\boldsymbol{e}_{x_{n+1}} \cdot \boldsymbol{e}_Z)\boldsymbol{e}_Z|} \\ \boldsymbol{e}_{y\ aux} &= \boldsymbol{e}_Z \times \boldsymbol{e}_{x\ aux}. \end{aligned}$$

# Chapter 3

# Multi-fidelity modeling of water forces

The closure of the rowing boat dynamical model, represented by Equation (2.1), requires a suitable modeling of the fluid dynamic forces $\mathbf{F}^w$ and moments $\mathbf{M}^w$. Modeling the fluid flow past a competition rowing boat presents several complications. First, modeling the viscous effects is important for an accurate estimation of the skin friction force. Second, modeling the air-water interface and its interaction with the hull is crucial for accurate estimation of the fluid-structure interaction forces, as the water waves induced by the motion of the boat constitute a significant part of the rowers energy that is dissipated to the surrounding fluid. Finally, a rowing boat is a body with a complex geometry, in the sense that its shape cannot be conveniently defined by means of an analytical formula, but is typically generated by means of a Computer-aided design (CAD) tool. Thus, the models and model equations should be based on a discretized representation of the hull, that might have to be compatible with the one of a CAD tool. In this chapter, we present a multi-fidelity approach for modeling the water forces. The reason for taking this approach is that the governing equations, namely the Navier–Stokes equations, are not readily solvable on complex geometries such as that of a rowing boats.

## 3.1 Multi-fidelity modeling

A first model reduction of the Navier–Stokes equations would be based on their discretization. Adequate discretization of the Navier–Stokes equations requires the simulation of the flow up to the smallest turbulent scales. Because of the high Reynolds numbers associated with the flow past rowing boats, such a simulation will require an impractically high number of degrees of freedoms. As such, further model reduction is needed to account for turbulence effects without having to simulate the flow up to the smallest turbulent scales. Typically, this reduction is obtained by filtering or averaging the Navier–Stokes equations, in order to only solve explicitly for the mean motion and for the largest turbulent scales, and model the effect of the smaller scales on the mean flow. The resulting fluid dynamic model, is then complemented with an adequate strategy such as a front capturing Volume of Fluid method, for the computation of the water free surface evolution. A numerical fluid dynamic model of this kind would be an ideal high fidelity model for our studies, as it would be able to simulate the viscous behavior of the fluid (in particular in the boundary layer region developing in proximity of the boat surface), to predict the motion of the water free surface, and to consider non analytical boat geometries.

Flow simulations employing the model described above can take several days, and given the quantity of numbers processed and the level of detail that characterizes them, they would require additional time to analyze and interpret the results. This would be acceptable if the simulations are used in the very last stages of the boat design, in which the effects of small changes in the hull geometry need to be assessed. On the other hand, reduced-order models that stress important physical considerations would be very useful in the earlier stages of the design to provide a quick estimation of few set of performance indices. Such reduced-order models on boats, ships, and other water piercing objects are usually based on the irrotational flow assumption. In presence of an incompressible fluid such as water, and of a simply connected domain, the irrotational flow assumption results in a velocity field admitting a scalar potential function, which is governed by the linear Laplace equation. This model does not account for viscous effects, which are recovered by other means, that usually involve coefficients or equations derived from simulations performed with the high

fidelity model. Typically, the Laplace equation is only solved in the water domain and two time dependent nonlinear boundary conditions are applied on the water free surface. The first condition is a kinematic boundary condition expressing the fact that the fluid velocity is always parallel to the free surface, and allows for the computation of the water surface time evolution. The second condition is derived from Bernoulli's equation and is used to compute the evolution of the velocity potential on the free surface. Due to the need to satisfy these nonlinear boundary conditions, the resulting flow potential problem is nonlinear, and cannot benefit from the application of the principle of superimposition of motions, which, in the case of a rowing boat would have allowed for a very useful decomposition of the flow into components due to the boat's mean and secondary motions. On the other hand, assuming that the oscillatory motions of the boat and the generated water waves are small, it is possible to linearize the free surface boundary condition. With this assumption, one can implement a low fidelity linear model. This model makes use of algebraic relationships obtained with offline steady-state RANS computations that estimate the water forces due to the boat mean motions. The forces due to the secondary motions are estimated by solving a radiation problem for the boat set in harmonic oscillations in still water. This low fidelity reduced order model is able to simulate a complete race in few minutes, and is ideal for the evaluation of the performance of a hull or of a crew in a reasonable time. In the following sections, we will discuss the implementation of different fluid dynamic models and results from their coupling with the rowing boat dynamical model. Particularly, we will compare results obtained with the different models to cross validate them.

## 3.2 A high fidelity model based on the solution of RANS equations

The motion of a viscous incompressible fluid is governed by the incompressible Navier–Stokes equations, which are written as

$$\begin{cases} \boldsymbol{\nabla} \cdot \boldsymbol{u} = 0 \\ \rho \dfrac{\partial \boldsymbol{u}}{\partial t} + \rho \boldsymbol{\nabla} \cdot (\boldsymbol{u} \otimes \boldsymbol{u}) - \boldsymbol{\nabla} \cdot \boldsymbol{T}(\boldsymbol{u}, p) = \rho \boldsymbol{g} \end{cases} \quad \text{in } \Omega \tag{3.1}$$

where $\boldsymbol{u}(\boldsymbol{X},t)$ and $p(\boldsymbol{X},t)$ indicate the unknown velocity and pressure fields respectively, $\boldsymbol{g}=(0,0,g)^T$ is the gravity acceleration vector and $\boldsymbol{T}(\boldsymbol{u},p)=\mu(\boldsymbol{\nabla u}+\boldsymbol{\nabla u}^T)-p\boldsymbol{I}$ is the stress tensor. $\rho$ and $\mu$ are, respectively, the fluid's density and dynamic viscosity. These equations form a set of nonlinear partial differential equations in which the four independent variables are the three space coordinates and time. The computational domain, $\Omega$, in which these equations are solved is a three-dimensional region surrounding the boat hull, as illustrated in Fig. 3.1.

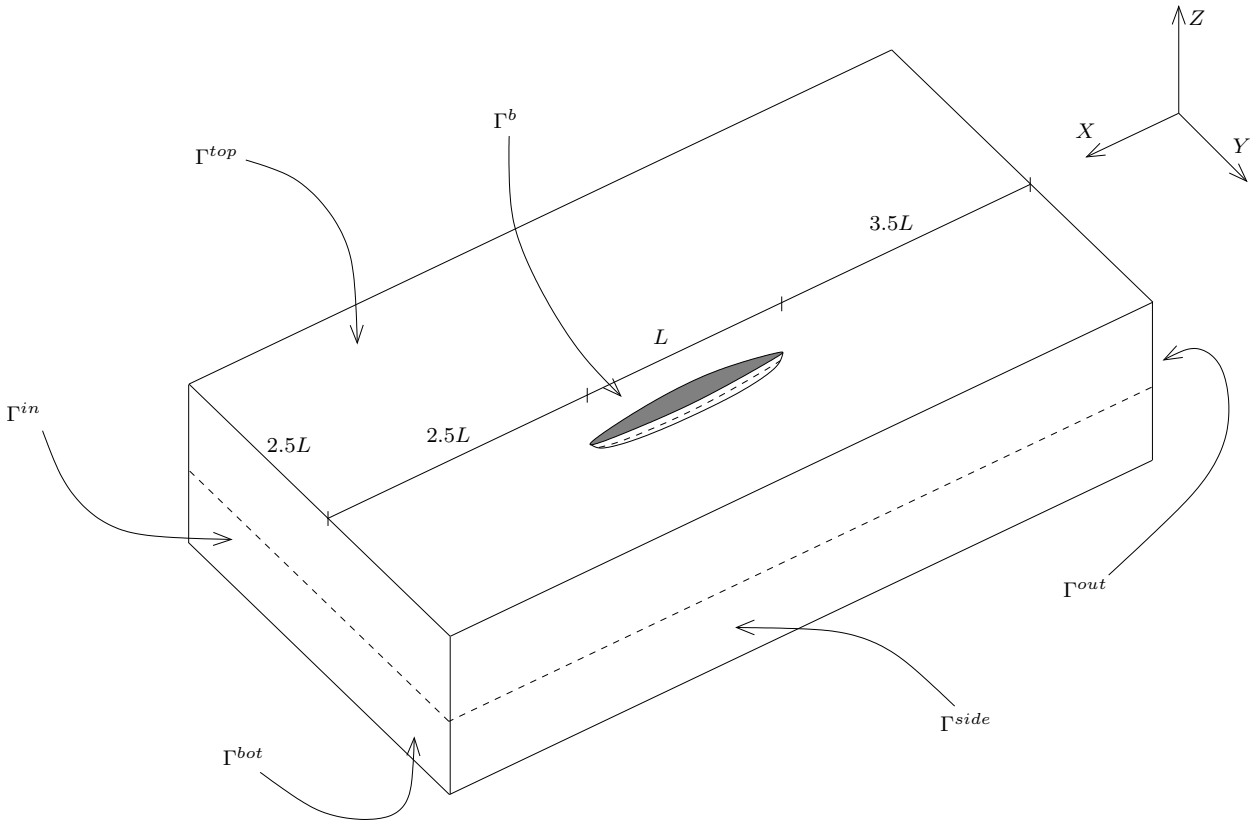


Figure 3.1: The computational domain, $\Omega$, for the RANS simulations.

The above equations are complemented by the initial condition

$$\boldsymbol{u}=\boldsymbol{u}_0, \qquad \text{in } \ \Omega \ \text{ for } t=0, \tag{3.2}$$

and by a suitable set of boundary conditions on the hull surface and on the boundaries of

the computational domain. The normal and tangential components of the fluid velocity on the boat surface $\Gamma^b$ are obtained from non homogeneous Dirichlet boundary condition which is written as

$$\boldsymbol{u} = \dot{\mathbf{G}}^h + \boldsymbol{\omega} \times (\boldsymbol{X} - \mathbf{G}^h) \qquad \text{on } \Gamma^b.$$

As for the inflow boundary, we apply a non homogeneous Dirichlet boundary condition, namely

$$\boldsymbol{u} = \boldsymbol{V}_\infty \qquad \text{on } \Gamma^{in},$$

while at the outflow boundary, we specify the value for the normal component of the stress tensor

$$\boldsymbol{T}(\boldsymbol{u}, p) \cdot \boldsymbol{n} = \begin{cases} 0 & Z \geq Z_{wl} \\ \rho^w g (Z_{wl} - Z) & Z < Z_{wl} \end{cases} \qquad \text{on } \Gamma^{out}$$

where $\rho^w$ is the water density and $Z_{wl}$ is the height of the undisturbed water free surface. A symmetry boundary condition, reading

$$\begin{aligned} u_n &= 0 \\ \frac{\partial \boldsymbol{u}_t}{\partial n} &= 0 \end{aligned} \qquad \text{on } \Gamma^{side}, \Gamma^{top}$$

is used in the domain truncation surfaces $\Gamma^{side}$. Finally, the no-slip condition is applied at the water basin bottom surface, namely

$$\boldsymbol{u} = \boldsymbol{V}_\infty \qquad \text{on } \Gamma^{bot}.$$

It is well known that for high Reynolds numbers, $Re$, in presence of turbulent flow regime, a suitable discretization of Navier–Stokes equations requires a computational grid with space and time dimensions small enough to capture the smallest turbulent scales. In the rowing boat problem, where $Re \simeq 10^7$, the solution of the Navier–Stokes equations, called Direct Numerical Simulation (DNS), would result in a discretized system having several billions of unknowns, and impractical resolution times.

Another possible approach is to reduce the number of unknowns needed by the flow simulations and model the smallest scales. This approach, namely, the Large Eddy Simulation (LES), is based on the observation that the large turbulent structures are dependent on the

flow boundary conditions, while the smaller eddies are more isotropic and independent of the mean flow features. Thus, the large scales are computed, while the smaller ones are accounted for by means of a sub-grid scale model obtained by filtering the Navier–Stokes equations with respect to the time or space variables. Even if the computational effort is substantially reduced with respect to DNS, LES has been devised to provide a level of detail in the flow description, which is far too high for the problem considered here. In particular, the high computational needs in the boundary layer regions surrounding the boat surface, make LES too expensive for our application.

Because they are based on time or space averaging of the Navier–Stokes equations, the Reynolds Averaged Navier–Stokes (RANS) equations only require the computation of the mean flow. The turbulence effects at all scales are then modeled using empirical relations and coefficients. As such, RANS based simulations are a good compromise between computational cost and needed details. In such a procedure (see (24)), the fluid dynamic variables are split into their mean value (which becomes the new unknown of the problem) and turbulent fluctuations, namely, $\boldsymbol{u} = \overline{\boldsymbol{u}} + \boldsymbol{u}'$ and $p = \overline{p} + p'$, with the overbar indicating the mean components, and the $'$ symbol indicating the fluctuating components. The continuity and momentum equations (expressed for clarity's sake in tensor notation) become

$$\frac{\partial \overline{u}_i}{\partial X_i} = 0 \tag{3.3}$$

$$\rho \frac{\partial \overline{u}_i}{\partial t} + \rho \overline{u}_j \frac{\partial \overline{u}_i}{\partial X_j} = -\frac{\partial \overline{p}}{\partial X_i} + \frac{\partial}{\partial X_j} \left[ \underbrace{\mu \left( \frac{\partial \overline{u}_i}{\partial X_j} + \frac{\partial \overline{u}_j}{\partial X_i} \right)}_{\text{Visc. Stress Tens.}} - \underbrace{\rho \left( \overline{u_i' u_j'} \right)}_{\text{Reynolds Stress Tens.}} \right]. \tag{3.4}$$

In these equations, the only term containing fluctuation terms is the Reynolds stress tensor $\tau_{ij} = \rho \overline{u_i' u_j'}$. To adequately close the problem, it is necessary *to model* this tensor in terms of the gradients of the mean velocity —the other unknowns in the system of equations. The turbulence model, chosen here, is the standard $k - \epsilon$ model, based on the Boussiniesq assumption (see (25)), namely

$$\tau_{ij} = \mu_T \left( \frac{\partial \overline{u}_i}{\partial X_j} + \frac{\partial \overline{u}_j}{\partial X_i} \right) - \frac{1}{3} \rho k \delta_{ij}, \tag{3.5}$$

where the turbulent viscosity $\mu_T$ is computed by means of the following equation

$$\mu_T = C_\mu \frac{k^2}{\epsilon}$$

based on the turbulent kinetic energy, $k$, and turbulent dissipation, $\epsilon$. These quantities are obtained by solving the corresponding transport equations

$$\rho \frac{\partial k}{\partial t} + \rho \overline{u}_j \frac{\partial k}{\partial X_j} = \tau_{ij} \frac{\partial \rho \overline{u}_i}{\partial X_j} - \epsilon + \frac{\partial}{\partial X_j} \left[ \left( \mu + \frac{\mu_T}{\sigma_k} \right) \frac{\partial k}{\partial X_j} \right] \tag{3.6}$$

$$\rho \frac{\partial \epsilon}{\partial t} + \rho \overline{u}_j \frac{\partial \epsilon}{\partial X_j} = C_{\epsilon 1} \frac{\epsilon}{k} \tau_{ij} \frac{\partial \rho \overline{u}_i}{\partial X_j} - C_{\epsilon 2} \frac{\epsilon^2}{k} + \frac{\partial}{\partial X_j} \left[ \left( \mu + \frac{\mu_T}{\sigma_\epsilon} \right) \frac{\partial \epsilon}{\partial X_j} \right], \tag{3.7}$$

where the closure coefficients assume the values

$$C_{\epsilon 1} = 1.44, \quad C_{\epsilon 2} = 1.92, \quad C_\mu = 0.09, \quad \sigma_k = 1, \quad \sigma_\epsilon = 1.3.$$

Another complication in modeling the flow past a rowing boat, is the presence of two different fluids around the boat. Accounting for the presence of the air-water interface and its interaction with the hull is crucial for accurate estimation of the fluid-structure interaction forces, as the water waves induced by the motion of the boat represent a significant part of the rowers energy dissipated by the surrounding fluid. In the RANS simulations, the presence of both air and water is modeled by means of a Volume of Fluid (VOF) technique. This method consists of a front capturing strategy in which an additional scalar variable, the fraction of volume $C$, is used to determine if a point is in the water ($C = 1$) or in the air ($C = 0$). The two considered fluids are then treated as a single system having discontinuous physical properties defined as

$$\rho = C\rho_{water} + (1 - C)\rho_{air}$$

$$\mu = C\mu_{water} + (1 - C)\mu_{air}.$$

To compensate for the additional unknown $C$, the system is complemented by an additional transport equation, namely

$$\frac{\partial C}{\partial t} + \overline{u}_j \frac{\partial C}{\partial X_j} = 0. \tag{3.8}$$

### 3.2.1 Numerical solution

The Reynolds Averaged Navier–Stokes equations described in the previous sections have been solved by means of the commercial software Fluent, which is based on a finite volumes discretization method (26). In such a method, algebraic discretized equations are obtained first by integrating the governing equations on cells (or finite volumes) composing the computational domain. The resulting integral equations contain both volume and surface (or flux) integrals, that are evaluated by means of a mid point quadrature rule, to obtain a set of algebraic equations. Since the unknowns of the discretized problem are the discrete values assumed by the variables in the geometrical centers of the cells, the face center values of the variables, coming form the flux integrals, are expressed in terms of the cell center values by means of a second order upwind interpolation scheme.

In computing the fraction of volume, $C$, the choice of the interpolation scheme used to obtain the face centroids values from cell centered values is particularly important. On one hand, upwind schemes are too diffusive and lead to an unwanted smearing of the interface region; on the other hand, less diffusive schemes, such as centered finite difference schemes, produce non physical oscillations. For this reason, the face values of $C$ are interpolated with a special treatment, which includes corrections to guarantee that the flux through a face is lower or equal with respect to the one coming form the upwind cell, and to avoid the wrinkling of the interface in case of a parallel convective velocity.

Observing the system of partial differential equations given by equations 3.3, 3.4, 3.6 and 3.7, we notice the lack of an evolution equation for $p$. From a mathematical point of view, the pressure behaves in the system as a Lagrangian multiplier for the incompressibility constraint. This implies that the velocity field can be obtained from the momentum equation, only after a pressure field has been prescribed. The correct pressure field is the one yielding a velocity which fulfills the continuity equation, which can thus be considered the lacking pressure equation. Applying a so called *SIMPLE* algorithm (27), the solver for each iteration computes a correction $p'$ to the initial pressure $p^*$, so that the resulting velocity field fulfills the continuity equation.

### 3.2.2 Time advancing scheme

The RANS fluid dynamic model is coupled with the rowing boat dynamical system by means of an explicit coupling. Starting from an initial velocity and position, for each time step, the fluid dynamic solver computes the fluid dynamic forces. Before the beginning of the ensuing time step, the rowing boat dynamical system solver is called, to compute the new velocity and position of the hull. After the hull is moved into the new position, the fluid dynamic mesh is deformed and smoothed, in order to perform a new RANS solver time step.

As for the reference frame used for the high fidelity simulations, the best possible choice would be the inertial reference frame translating in the $X$-direction with a velocity equal to the mean surge speed. In such a reference frame, the hull is constantly oscillating around an equilibrium position. Unfortunately, the oscillations on the surge degree of freedom are too high and cause the mesh to deform excessively during the computation. This is further complicated by the fact that the mean surge velocity (which is a result of the computation) cannot be easily computed *a priori*. Thus, the reference frame used is a non inertial reference frame which follows the boat motion in the surge direction. As a result, a source term representing the inertial forces acting on each control volume, and due to the reference frame horizontal acceleration is added to the right hand side of the RANS equations. So, in the high fidelity simulations, the boat is not moving in the $X$-direction, whereas it moves freely in all the other degrees of freedom. Because all these motion have practically null average velocities, and relatively small amplitudes of oscillations, the mesh can be deformed without impairing the computations.

It is finally important to note that, for each $\Delta t$, the rowing boat dynamics solver considers the fluid dynamic forces to be constant and equal to the last value computed by the RANS solver. For of this reason, and because the coupling is performed using an explicit Forward Euler time advancing scheme, the size of the time step has to remain particularly low, so as to avoid instabilities. An implicit coupling would allow for sensibly higher time steps, which would make the simulations consistently faster. Since the solver used is a commercial software though, an implicit coupling is not possible.

Table 3.1: Values of the input parameters used for the setup of the symmetric and non symmetric rowing boat dynamics simmulations.

| $r$ | $m_{r\ 1}$ | $m_{r\ 2}$ | $m_{r\ 3}$ | $m_{r\ 4}$ |
|---|---|---|---|---|
| 36 $\frac{\text{strokes}}{\text{min}}$ | 80 Kg | 80 Kg | 80 Kg | 80 Kg |

| Case | $F_{X_{max}\ 1}$ | $F_{Z_{max}\ 1}$ | $F_{X_{max}\ 2}$ | $F_{Z_{max}\ 2}$ | $F_{X_{max}\ 3}$ | $F_{Z_{max}\ 3}$ | $F_{X_{max}\ 4}$ | $F_{Z_{max}\ 4}$ |
|---|---|---|---|---|---|---|---|---|
| Symm. | 1200 N | 200 N | 1200 N | 200 N | 1200 N | 200 N | 1200 N | 200 N |
| Non Symm. | 1212 N | 202 N | 1200 N | 200 N | 1200 N | 200 N | 1200 N | 200 N |

### 3.2.3 High fidelity simulation results

Fig. 3.2 shows the time series of the surge, pitch and heave motions obtained by coupling the rowing boat dynamical system with the RANS fluid dynamic model. The simulations reproduce the dynamics of a coxless four pushing at a pace of 36 $\frac{\text{strokes}}{\text{min}}$. Each of the four rowers is assumed to have a height of 1.80 m and a body mass of 80 kg (see Table 3.1). On this sweep boat, the athletes are positioned so that the oarlocks of the first and third rowers are placed on the starboard side of the boat, while the second and fourth rowers are rowing on the port side. The simulations were started from a fully developed steady-state solution in which the boat surge velocity was set to 5.3 m/s, and the boat sinkage was fixed at the hydrostatic value (*i.e.*, the hull barycenter initial vertical position is located 3.05 cm under the undisturbed water level). The initial $Y$ position, and all the Euler angles were set to zero. At the time $t = 0$ s, when the first oars stroke starts, the boat hull is left free to move under the action of the computed fluid dynamic and rowers induced forces. The simulation was carried on for 15 s, needing a completion time of about 60 h on six parallel 2.6 GHz Intel Zion quad core processors of a Linux cluster.

In the first, symmetric, test case considered, the maximum horizontal and vertical oarlock forces of each rower are set to 1200 N and 100 N respectively, as shown in Table 3.1. Fig. 3.2 shows the motions of the center of mass of the boat in the three degrees of freedom contained in the symmetry plane, for the final 5 s of the simulation, in which the system has nearly reached a steady-state solution. Given the rowing pace of 36 $\frac{\text{strokes}}{\text{min}}$, which corresponds to a stroke period of 1.667 s, this time window contains exactly 3 complete strokes. The

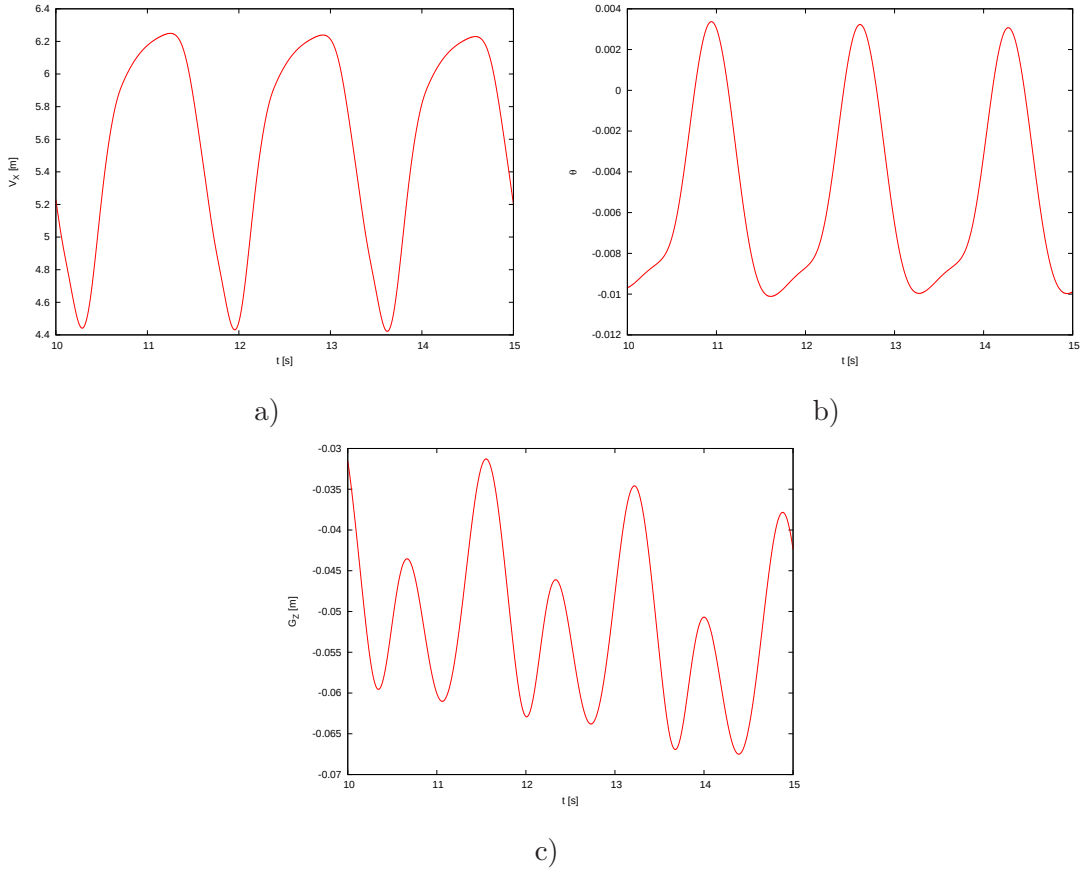


Figure 3.2: Computed time histories of boat motions in the vertical plane as obtained from coupling RANS model and rowing boat dynamical model. Plot a) shows the time history of the boat surge velocity, plot b) depicts the time evolution of the pitch Euler angle, and plot c) shows the time history of the hull vertical position.

time history of the hull gravity center horizontal velocity (Fig. 3.2 (a)) indicates how the hull forward motion is characterized by strong accelerations and decelerations caused by the rowers periodical displacement and forces on the hull. In a single stroke, the velocity oscillates around a mean value of 5.5924 m/s, with a minimum value of 4.4 m/s and a maximum value of 6.3 m/s. In particular, it should be noted that, in this boat class, the peak speed is not obtained during the stroke, but during the recovery phase, in which the four rowers (having a total mass of 320 kg) are moving backwards with respect to the hull, (which only weights 50 kg) and is propelled forward by conserving the linear momentum. The hull velocity in fact

drastically drops when the rowers end their backward motions and push on the footboards with their feet.

Fig. 3.2 (b), shows the time history of the pitch angular Euler angle $\theta$. As expected, the pitch angle is negative during the catch phase of each stroke, in which the rowers centers of gravity are located backwards, with respect to the hull barycenter. This motion produces a moment that lifts the hull bow. When the rowers are fully extended, right before the beginning of the recovery phase, the pitch angle is positive and reaches its peak values. For this 12 m long boat, the computed $\theta$ values result in bow and stern vertical displacements that are in the range of $\pm 5$ cm. These displacements are compatible with the ones observed during races. The average pitch angle is $-0.0051$ rad. This negative value is considered by designers to be a good characteristic for a rowing boat, as a hull advancing with a slightly lifted bow typically results in a lower front pressure; hence, in a lower drag.

Finally, the vertical motion of the hull center of gravity is presented in Fig. 3.2 (c). The plot shows that the oscillation frequency for the vertical motion is twice that of the rowers frequency of motion. This is due to the fact that, during a stroke, the rowers move back and forth only once, whereas they lift and lower their center of mass twice, a first time during the active phase of the stroke, and a second during the recovery phase. The average vertical position of the hull center of gravity is $-5.15$ cm, which is a couple of centimeters lower than the hydrostatic equilibrium position. This is explained by the fact that when hydrodynamic effects are considered, the lift force provided by the water is slightly reduced in comparison with the hydrostatic case. The acceleration of the fluid around the boat, produces a velocity increase that causes a slight reduction in the pressure under the boat. The plot also shows that the vertical motion has not reached a steady-state solution after 15 s. This is probably due to the presence of a small non physical wave which develops on the free surface. This wave is caused by the source term added on the right hand side of the momentum equation, to enable us to perform the computations in the non inertial reference frame.

Fig. 3.3 shows a height contour of the water free surface computed at the 15th second of the RANS simulation. The plot clearly shows a parasite wave due to the momentum equation source term. The wave has an amplitude of $\pm 2$ cm (in the RANS simulation the undisturbed free surface has a height of $-10.44$ cm) and a wavelength that is comparable to the length

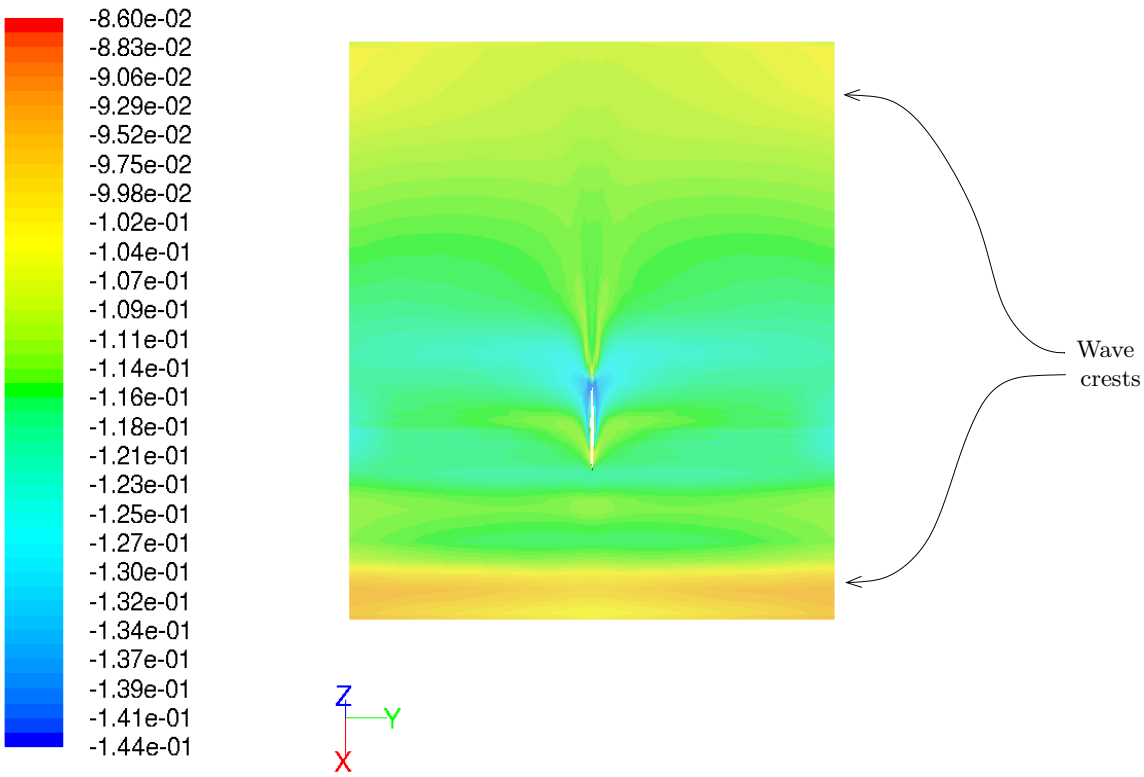


Figure 3.3: Free surface height (in meters) fields obtained from the RANS simulations using Fluent at 15 s. The presence of a low-amplitude parasite wave is evident in the region far from the boat.

of the computational domain. It is therefore possible that this parasite wave is not affecting the boat pitch and the estimated water forces on the boat, but is simply modifying the boat vertical position, preventing it from settling to a steady-state solution. The presence of this parasite wave could, in principle, be avoided by performing the simulations in the inertial reference frame surging with a constant speed equal to the boat mean surge velocity. Unfortunately, as mentioned above, this kind of approach leads to an excessive deformation of the computational mesh, which causes the simulations to diverge. In fact, the hull mean surge velocity is a result of the computation, and, as such, it cannot be estimated *a priori* with sufficient accuracy, the boat progressively diverges from the original position during the simulations, which strains the mesh until negative volumes appear.

To test the effect of the human control model, as discussed in Section 2.4, and analyze the

behavior of the boat in six degrees of freedom, a non symmetrical test case is also considered. As shown in Table 3.1, the non symmetrical force configuration is obtained by increasing first rower maximum horizontal oarlock force to 1212 N, and vertical oarlock force to 202 N. All other simulation parameters, and in particular all other rowers forces, are kept at the same values as in the symmetrical case discussed above. This difference between forces on the oarlocks of the starboard and port sides yields nonzero mean values for both roll and

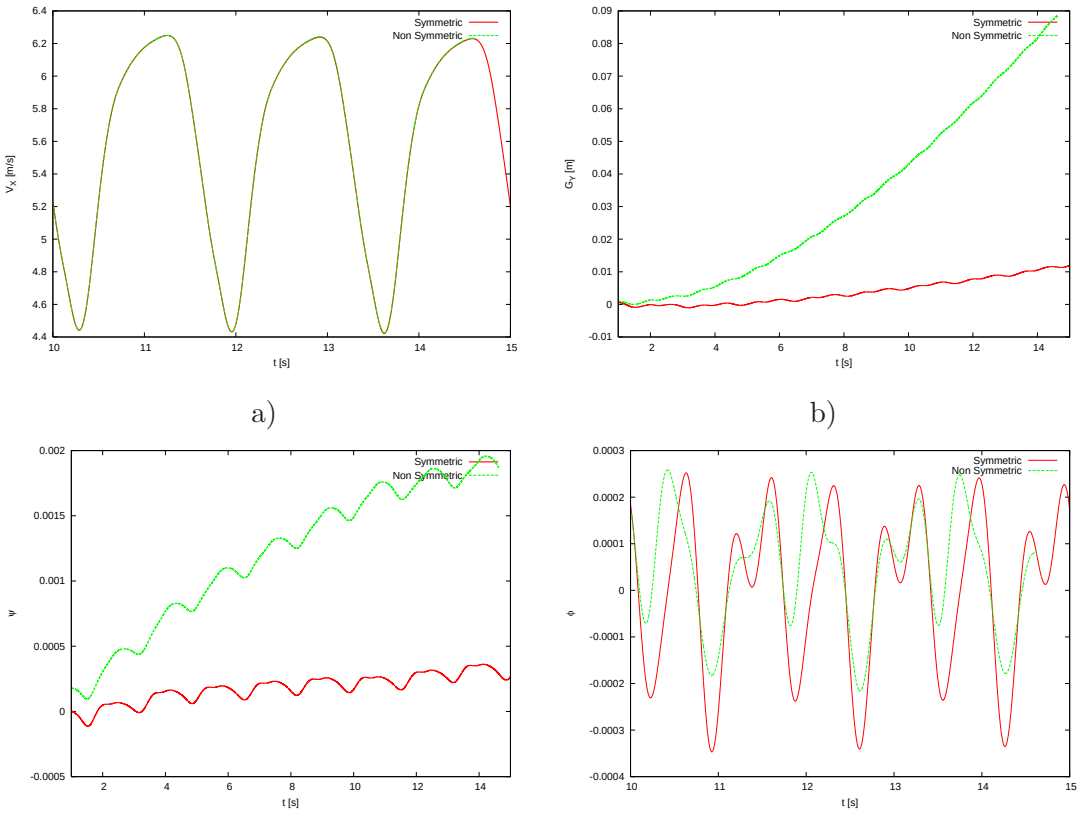


Figure 3.4: Comparison of time histories of boat motions obtained with symmetric forces (—) and with non symmetric forces (—) as imposed by the rowers in a coxless four case. All the motions are computed by coupling RANS solution of fluid flow with the dynamical system discussed in Chapter 2. Plot a) shows the last 5 s of the surge velocity time history, plot b) depicts the full time history of the boat sway motion, plot c) shows the full time history of the yaw Euler angle, and plot d) shows the last 5 s of the roll angle time history.

yaw motions. It will also result in a thrust that is not aligned with the $X$ direction, and in a sway motion. The value of the force unbalance between the two sides of the boat was kept low in order to limit the sway motion and the yaw angle to values which would not lead to excessive deformation of the computational grid.

Fig. 3.4 depicts a comparison of the motions of the rowing boat when subjected to symmetrical and non symmetrical forces. Fig. 3.4 (a) compares the surge velocity time history in the last 5 s of the simulation. The difference between the two results is very small. Yet, it is observed that the boat is faster in the non symmetrical case, in which the computed mean surge velocity is 5.5969 m/s, against the 5.5926 m/s of the symmetrical case. A horizontal force increase of 0.25% resulted in a velocity increase of 0.08%. A partial explanation for this, is that part of the energy introduced in the system is dissipated into the lateral motion, as illustrated in Fig. 3.4 (b). This figure shows that in the non symmetrical case, the force unbalance yields a lateral displacement of about 9 cm in 15 s, in comparison to approximatively 1 cm over the same period in the symmetrical test case. It is noted here that the presence of a non-negligible, but small (in 15 s the boat advances of 84 m and sways of 1 cm) lateral motion even in the symmetrical test cases, could be due to numerical errors related to a non perfectly symmetric discretization of the boat surface or of the domain in the RANS simulation, which are amplified by the non negligible lateral lift that the hull is subjected to whenever a yaw angle is present. Fig. 3.4 (c), shows a comparison of time histories of the yaw angle for both symmetrical and non symmetrical cases. The results show that even in the symmetrical case, the system settles to a very small yaw angle, so that the hull produces a lateral lift, behaving just as a symmetrical airfoil at a non zero angle of attack. The plots also show that even for the 0.5% force unbalance considered, the hull yaw angle reaches values that are approximatively one order of magnitude higher than those of the symmetrical test case, confirming that the non zero yaw angle observed in the symmetrical forces case is due to propagation of numerical errors.

Fig. 3.4 (d) shows the time history of the roll angle for both symmetrical and non symmetrical test cases. As expected, in the symmetrical test case the mean roll angle is nearly null, settling to a value of $1.03 \cdot 10^{-6}$ rad. In the non symmetrical case, as the vertical downward forces exerted by the rowers on the oarlocks are slightly higher on the

starboard side than on the port one, the resulting mean roll angle settles on a positive value of $2.75 \cdot 10^{-4}$ rad.

It is finally useful to note that the equilibrium yaw and roll angle values obtained in the simulations depend on the values of gain coefficients in the control scheme, discussed in Sec. 2.4. Higher gain values would result in lower equilibrium angles, and consequently less sway. As the lateral force and the yaw fluid dynamic moment assume significant values in the RANS simulations, the gain coefficients were kept to high values, in order to minimize the yaw and lateral motion of the boat, which would affect the computational mesh quality, and impair successful simulations.

## 3.3 3D Potential model

The vorticity in the flow field past a slender hull like that of a rowing boat is confined to the boundary layer and to a thin wake following the boat. Thus, the assumption of irrotiational flow is fairly accurate, and the viscous effects can be recovered by other means such as empirical algebraic formulas, or —better— by the interface with a suitable boundary layer model. In presence of an incompressible fluid such as water, and of a simply connected domain, the irrotational flow assumption results in a velocity field admitting a scalar potential function $\Phi(x, y, z, t)$, namely

$$\boldsymbol{V} = \boldsymbol{\nabla}\Phi \qquad \text{in } \Omega.$$

In such a case, the continuity equation simplifies to the Laplace's equation for the flow potential

$$\Delta\Phi = 0 \qquad \text{in } \Omega,$$

and the momentum equation reduces to the Bernoulli's equation

$$\frac{p}{\rho} + \frac{\partial\Phi}{\partial t} + gz + \frac{1}{2}|\boldsymbol{\nabla}\Phi|^2 = C(t) \qquad \text{in } \Omega. \tag{3.9}$$

In this framework, the unknowns of the problem $\Phi$ and $p$ are uncoupled. So, it is possible to solve Laplace's equation, to obtain the velocity field, and employ the Bernoulli's equation to

get the pressure field.

Typically, Laplace equation is solved in the water domain, the shape of which is time dependent. Consequently, the boundary represented by the water free surface will be a moving boundary, and two boundary conditions will be needed to compute the boundary position and potential values. These are

$$\frac{D\boldsymbol{X}}{Dt} = \boldsymbol{\nabla}\Phi \qquad \text{on} \quad \Gamma^w \tag{3.10}$$

and

$$\frac{D\Phi}{Dt} = -\frac{p_a}{\rho} - g\eta + \frac{1}{2}|\boldsymbol{\nabla}\Phi|^2 \qquad \text{on} \quad \Gamma^w \tag{3.11}$$

where $\frac{D}{Dt} = \frac{\partial}{\partial t} + \boldsymbol{\nabla}\Phi \cdot \boldsymbol{\nabla}$ is the material derivative and $\eta(x, y, t)$ is used to represent the water surface elevation function. The first condition is a representation of the fact that the free surface is a stream surface for the flow. The second condition is derived from the unsteady Bernoulli's equation (3.9), and expresses the fact that the pressure on the water surface must be equal to the ambient pressure $p_a$.

Due to the nonlinearities in the boundary conditions (3.10) and (3.11), the potential problem is nonlinear. Typically, it is solved by means of a Mixed Eulerian–Lagrangian (MEL) approach, which consists of solving the Laplace equation at each time instant, through the imposition of a Dirichlet boundary condition on the free surface boundary, and then employing the computed solution in conditions (3.10) and (3.11), to update the surface position and potential for the next time step. Despite their accuracy in the simulation of the dynamics of water waves, a fully nonlinear potential simulations using MEL cannot benefit from the application of the principle of superposition of effects, which in the case of a rowing boat would have allowed for a useful decomposition of the flow into components due to the boat's mean and secondary motions.

To obtain a linear governing problem, it is possible to apply perturbation theory and linearize the free surface boundary condition. Under the assumption of small wave slope $\epsilon$ we write

$$\Phi(x, y, z, t) = \epsilon\Phi_1(x, y, z, t) + \epsilon^2\Phi_2(x, y, z, t) + \dots \tag{3.12a}$$

$$\eta(x,y,t) = \epsilon\eta_1(x,y,t) + \epsilon^2\eta_2(x,y,t) + \dots \tag{3.12b}$$

and

$$p(x,y,z,t) = p_0(x,y,z,t) + \epsilon p_1(x,y,z,t) + \epsilon^2 p_2(x,y,z,t) + \dots \tag{3.12c}$$

in which the potential $\Phi_0$ and wave elevation function $\eta_0$ corresponding to the hydrostatic conditions are both null and have been omitted, while the hydrostatic pressure is given by $p_0(x,y,z,t) = \rho g z$, which is simply obtained by plugging $\Phi_0$ and $\eta_0$ in Bernoulli's equation.

Expanding (3.10) and (3.11) with respect to the vertical coordinate $z$ above the point $z = 0$ (we can do it under the assumption of small wave slope), we obtain

$$\left(\frac{\partial\eta}{\partial t} + \boldsymbol{\nabla}\Phi\cdot\boldsymbol{\nabla}\eta\right)_{z=0} + \eta\frac{\partial}{\partial z}\left(\frac{\partial\eta}{\partial t} + \boldsymbol{\nabla}\Phi\cdot\boldsymbol{\nabla}\eta\right)_{z=0} = \left(\frac{\partial\Phi}{\partial z}\right)_{z=0} + \eta\left(\frac{\partial^2\Phi}{\partial z^2}\right)_{z=0} \tag{3.13a}$$

$$\eta = -\frac{1}{g}\left(\frac{\partial\Phi}{\partial t} - \frac{p_a}{\rho} + |\boldsymbol{\nabla}\Phi|^2\right)_{z=0} + -\frac{\eta}{g}\frac{\partial}{\partial z}\left(\frac{\partial\Phi}{\partial t} - \frac{p_a}{\rho} + |\boldsymbol{\nabla}\Phi|^2\right)_{z=0}. \tag{3.13b}$$

The linearized boundary conditions are obtained by substituting the expansion (3.12) into equations (3.13), and grouping the first order terms, which yields

$$\frac{\partial\eta_1}{\partial t} = \frac{\partial\Phi_1}{\partial z} \qquad \text{on} \quad \overline{\Gamma}^w \tag{3.14}$$

and

$$\eta_1 = -\frac{1}{g}\frac{\partial\Phi_1}{\partial t} \qquad \text{on} \quad \overline{\Gamma}^w \tag{3.15}$$

where $\overline{\Gamma}^w$ is the undisturbed free surface. Equations (3.14) and (3.15) are combined to eliminate $\eta_1$ and obtain a boundary condition for the linearized potential problem, namely

$$\frac{\partial^2\Phi_1}{\partial t^2} + g\frac{\partial\Phi_1}{\partial z} = 0.$$

The free surface elevation can be computed from

$$\eta_1 = -\frac{1}{g}\frac{\partial\Phi_1}{\partial t}, \tag{3.16}$$

while the pressure $p_1$ is obtained from the linearization of the Bernoulli's equation (3.9)

$$p_1 = -\rho\frac{\partial\Phi_1}{\partial t}. \tag{3.17}$$

Using the principle of superimposition, the potential $\Phi_1$ obtained from the linearization can be decomposed into a diffraction potential $\varphi$, accounting for the effects of the mean surge motion, and a radiation potential $\psi$, accounting for the effects of the secondary oscillations of the boat. The potential and the corresponding forces and moments decomposition read

$$\begin{aligned} \Phi &= \varphi + \psi \\ \mathbf{F}^w &= \boldsymbol{F}^h + \boldsymbol{F}^m + \boldsymbol{F}^s \\ \mathbf{M}^w &= \boldsymbol{M}^h + \boldsymbol{M}^m + \boldsymbol{M}^s \end{aligned}$$

where $\varphi + \psi = \epsilon\Phi_1$, $\boldsymbol{F}^h$ and $\boldsymbol{M}^h$ are the hydrostatic forces and moments components, $\boldsymbol{F}^m$ and $\boldsymbol{M}^m$ are the forces and moments due to the hull mean motions, and $\boldsymbol{F}^s$ and $\boldsymbol{M}^s$ are the forces and moments due to the secondary motions.

The low fidelity linear model used in this work employs algebraic relationships obtained from offline steady-state RANS computations to estimate the forces and moments due to the boat mean motion, $\boldsymbol{F}^m$ and $\boldsymbol{M}^m$ respectively. On the other hand, the forces due to the secondary motions $\boldsymbol{F}^s$ and the corresponding moments $\boldsymbol{F}^s$, are estimated by solving a radiation problem for a boat set in harmonic oscillations in still water. As it turns out, the latter problem results in frequency dependent damping and added mass matrices that can be computed offline, and would be introduced in the time dependent dynamical system equations (2.1) by means of a convolution term.

### 3.3.1 Hydrostatic forces

The hydrostatic forces and moments are modeled by

$$\boldsymbol{F}^h(t) = -\rho g \int_{\Gamma^b(t)} (h_0 - Z)\mathbf{N} d\gamma, \tag{3.18}$$

and

$$\boldsymbol{M}^h(t) = -\rho g \int_{\Gamma^b(t)} (\boldsymbol{X} - \boldsymbol{G}^h) \times (h_0 - Z)\mathbf{N} d\gamma, \tag{3.19}$$

where $\mathbf{N}$ is the unit vector normal to the boat surface $\Gamma^b(t)$, expressed in the absolute reference frame. It is straightforward to show that the hydrostatic force has only a vertical component,

while the hydrostatic moment has a null yaw component. These integrals are computed by means of a surface mesh of the boat hull, which is displaced in the instantaneous position using the updated values of hull mass center displacement and Euler angles.

### 3.3.2 Forces due to mean motions

In our approximation, the forces and moments due to the mean surge motion are represented by a pure drag, namely

$$\boldsymbol{f}^m = -R\boldsymbol{e}_X, \qquad \boldsymbol{M}^m = 0, \tag{3.20}$$

where the resistance $R \geq 0$. To determine the resistance $R$, we employ empirical formulas, which depend on few parameters. The main terms used to compute $R$ are

$$R = \frac{1}{2}\rho|\Gamma^b_X(t)||V_X|V_X + \frac{1}{2}\rho C_v|\Gamma^b(t)||V_X|V_X + \frac{1}{2}\rho|\Gamma^b_Z(t)||V_X|V_X \tag{3.21}$$

where the three terms on the right hand size respectively represent the shape, viscous and wave drag. The drag coefficients, which are referred to the boat surface area $|\Gamma^b(t)|$ and to its projections in the $X$ direction $|\Gamma^b_X(t)|$ and in the $Z$ direction $|\Gamma^b_Z(t)|$, have either been taken from the literature (28) or computed by fitting a series of offline Reynolds Averaged Navier–Stokes Equations computations on the boat moving at different configurations and with constant speed (29).

### 3.3.3 Forces due to secondary motions: 3D potential model for wave radiation

The governing equation for this flow is

$$\Delta\psi = 0 \ \text{ on } \Omega \ \text{ and } \forall t.$$

To express the potential problem in a compact form, we introduce the following notation. As the boat is set in its reference static equilibrium position, we denote with $\boldsymbol{v} = [v_1, v_2, v_3, v_4, v_5, v_6]^T = [\dot{G}^s_X, \dot{G}^s_Y, \dot{G}^s_Z, \dot{\psi}^s, \dot{\theta}^s, \dot{\phi}^s]^T$ the vector containing the secondary motion velocities (the unknowns of our problem) and with $\mathcal{N} = [\mathcal{N}_1, \mathcal{N}_2, \mathcal{N}_3, \mathcal{N}_4, \mathcal{N}_5, \mathcal{N}_6]^T = [n_x, n_y, n_z, yn_x - xn_y, -xn_z + zn_x, -yn_z + zn_y]^T$ the *generalized normal vector*(13), whic permits us to adopt the same expression for the the linear and angular momentum equations.

We also consider a periodic motion resulting from the sum of harmonic components characterized by an angular speed which is a multiple of the angular speed of the fundamental component. Hence, we can consider a generic component with angular speed $\omega$ and write

$$v_s(t) = \mathrm{Re}(\Upsilon_s e^{-i\omega t}), \quad s = 1,2,3,4,5,6 \qquad \psi(t,\mathbf{X}) = \mathrm{Re}\left(\Psi(\mathbf{X})e^{-i\omega t}\right), \tag{3.22}$$

where $i = \sqrt{-1}$, while $\Upsilon_s$ and $\Psi$ are complex valued functions depending only on the spatial coordinates. $\mathrm{Re}(z)$ and $\mathrm{Im}(z)$ denote the real and imaginary part of the complex number $z$, respectively.

The total complex potential $\Psi$ is then written as the sum of six terms which are proportional to the velocity components of the secondary motion $\Upsilon_s$, i.e.

$$\Psi = \sum_{s=1}^{6} \Upsilon_s \Psi_s. \tag{3.23}$$

In the numerical domain $\Omega$, representing the portion of water surrounding the boat hull, the complex potential $\Psi_s$ satisfies the following differential equation and boundary conditions (13)

$$-\Delta\Psi_s = 0 \qquad \text{in } \Omega \tag{3.24a}$$

$$\frac{\partial \Psi_s}{\partial Z} = 0 \qquad \text{on } \Gamma^{bot} \tag{3.24b}$$

$$\frac{\partial \Psi_s}{\partial Z} - \frac{\omega^2}{g}\Psi_s = 0 \qquad \text{on } \overline{\Gamma}^{w} \tag{3.24c}$$

$$\frac{\partial \Psi_s}{\partial n} = \mathcal{N}_s \qquad \text{on } \Gamma^{b} \tag{3.24d}$$

$$\frac{\partial \Psi_s}{\partial n} = -i\kappa\Psi_s \qquad \text{on } \Gamma^{\infty} \tag{3.24e}$$

where, as illustrated in Fig. 3.5 the hull surface $\Gamma^b$ has been set in the reference position, $\overline{\Gamma}^w$ represents the undisturbed free surface, $\Gamma^{bot}$ denotes the bottom surface of the water basin, and $\Gamma^{\infty}$ is the surface at which the far field radiation boundary condition is applied.

Equation (3.24d) relates $\Psi_s$ to the geometry of the hull. Condition (3.24e) is the decay condition at infinity where $\kappa$ is the wave number which is the only real root of the dispersion relation

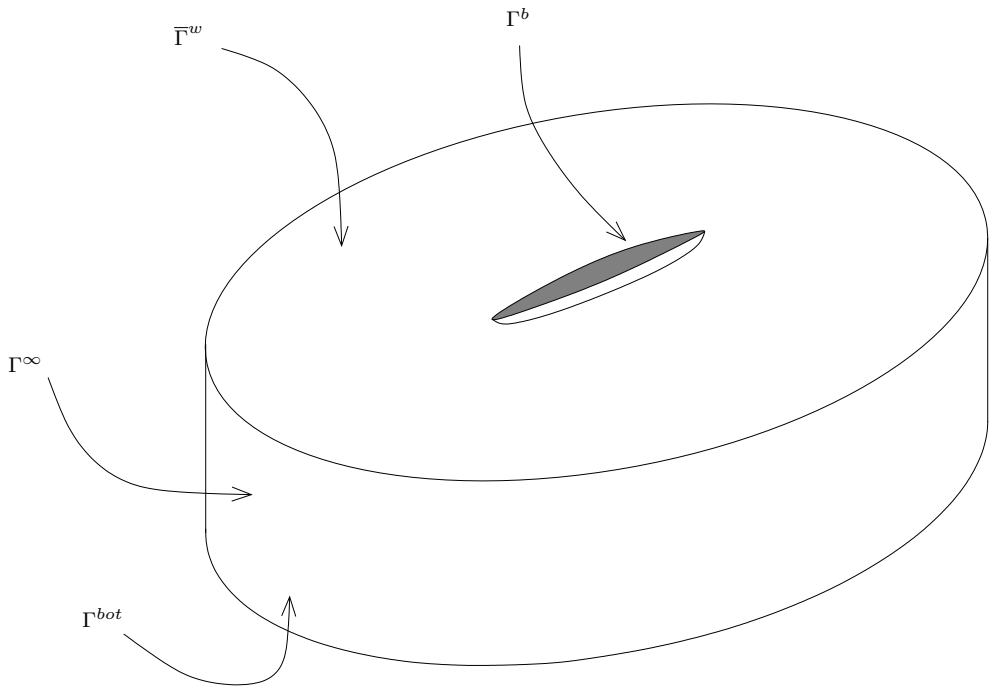


Figure 3.5: A sketch of the numerical domain employed in the 3D radiation potential computation.

$$\kappa \tanh(\kappa H) = \frac{\omega^2}{g}. \tag{3.25}$$

Assuming that $\kappa H = \frac{2\pi H}{\lambda} >> 1$ (the wavelengths of the generated which are small with respect to the depth of the basin, $H$), we obtain

$$\kappa = \frac{\omega^2}{g}. \tag{3.26}$$

Denoting by $L_b$ the length of the boat and assuming that the wave length of the generated gravity waves $\lambda \simeq L_b$ and that their amplitude $A << L_b$, the dynamic pressure $p_d$ induced by secondary motions is approximated by means of the linearized Bernoulli equation (3.17). The forces and moments generated by the dynamic pressure on the hull are then contained in the *restoring force vector* $\mathcal{F}^d = [F_X^d, F_Y^d, F_Z^d, M_X^d, M_Y^d, M_Z^d]$, which is computed by

$$\mathcal{F}^d = -\rho \int_{\Gamma_0^h} \frac{\partial \psi}{\partial t} \mathcal{N} \, d\gamma, \tag{3.27}$$

where the scull has been considered again in the reference position and with the undisturbed free surface. Once computed, the potentials $\Psi_s$ ($s = 1, 2, 3$) are plugged in equation (3.22) and (3.27) to yield the forces $\mathcal{F}^d$. We first define the *restoring force matrix*

$$f_{st} = i\rho\omega \int_{\Gamma_0^h} \Psi_s \mathcal{N}_t \, d\gamma, \tag{3.28}$$

with each component of this matrix representing the hydrodynamic reaction in the direction $t$ due to an oscillation of the boat in the direction $s$.

Using the implicit summation notation for repeated indices, we write the $t$-th component of the restoring force vector as

$$\begin{aligned} \mathcal{F}_t^d &= \mathrm{Re}(\Upsilon_s f_{st} e^{-i\omega t}) = \mathrm{Re}\left[(\mathrm{Re}\, f_{st} + i\,\mathrm{Im}\, f_{st})\, \Upsilon_s e^{-i\omega t}\right] \\ &= \mathrm{Re}\left[\left(i\rho\omega \int_{\Gamma_0^h} \mathrm{Re}\, \Psi_s \mathcal{N}_t \, d\gamma - \rho\omega \int_{\Gamma_0^h} \mathrm{Im}\, \Psi_s \mathcal{N}_t \, d\gamma\right) \Upsilon_s e^{-i\omega t}\right] \\ &= -\left(\rho \int_{\Gamma_0^h} \mathrm{Re}\, \Psi_s \mathcal{N}_t \, d\gamma\right) \dot{v}_s(t) - \left(\rho\omega \int_{\Gamma_0^h} \mathrm{Im}\, \Psi_s \mathcal{N}_t \, d\gamma\right) v_s(t). \end{aligned} \tag{3.29}$$

So, the restoring force vector is split into two terms, one proportional to the boat secondary accelerations, and one proportional to the secondary velocities. From a physical standpoint, the forces due to the secondary motions have a double effect on the dynamics of the scull, and can be interpreted as the sum of an added mass term, which effectively increases the boat mass, and a damping term, accounting for dissipative effects.

The resulting added mass and the damping matrices (13), are here indicated by $\mathcal{M}^s$ and $\mathcal{S}^s$, respectively. Their elements are defined as

$$\mathcal{M}_{st}^s = \rho \int_{\Gamma_0^h} \mathrm{Re}\,(\Psi_s)\mathcal{N}_t d\gamma, \quad s, t = 1, \ldots, 6 \tag{3.30}$$

$$\mathcal{S}_{st}^s = \rho\omega \int_{\Gamma_0^h} \mathrm{Im}\,(\Psi_s)\mathcal{N}_t d\gamma, \quad s, t = 1, \ldots, 6. \tag{3.31}$$

These matrices are both symmetric and positive definite (13), and only depend on the boat geometry. For this reason, they can be conveniently computed "off-line", and successively introduced in the system of governing equations (2.4). The non dimensionalized added mass and damping heave coefficients for an immersed hemisphere, computed with the methodology

described above are presented in Fig. 3.6. The results for this test case are compared with the corresponding curves obtained by Havelock ((1)). The agreement is satisfactory, especially in the middle range of frequencies, which corresponds to the typical frequencies of motion of the rowers.

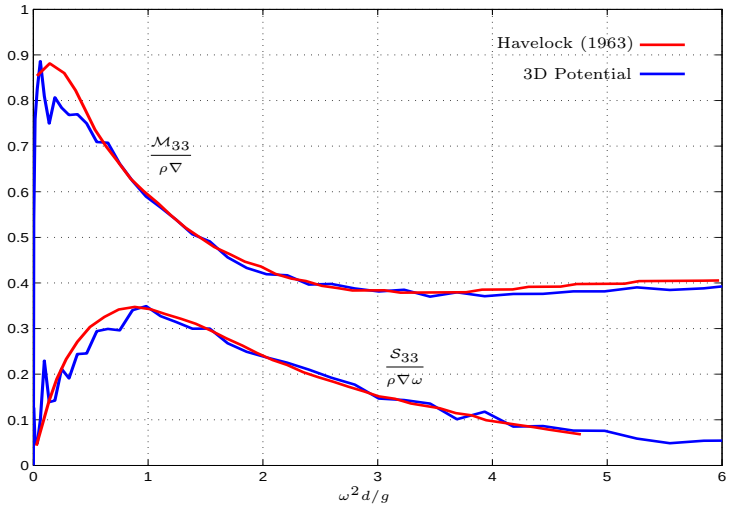


Figure 3.6: Non dimensionalized damping and added mass heave coefficients for an immersed hemisphere as a function of non dimensional frequency. The red curves in the plot are the result of Havelock (1), while the blue curves are the results obtained using codes developed in this work .

Because the coefficients in the added mass and the damping matrices depend on the frequency of the rowing action $\omega$, one should shift to the frequency domain in order to account for the effects of the added mass and of the damping on the dynamics of the scull. This leads to the presence of convolution integrals in the equations of motion, as pointed out by Newman (30). To account for the frequency dependence of added mass and damping matrices, we used a technique discussed by Fossen in (31). The added mass matrix in the time domain is written as

$$\mathcal{M}^s(t) = \lim_{\omega \to \infty} \mathcal{M}^s(\omega),$$

while, the damping forces are computed by means of the following convolution integral

$$\boldsymbol{F}_d(t) = \mathcal{S}^s(\infty)\boldsymbol{u} + \int_0^\infty K(\tau)\boldsymbol{u}(t-\tau)d\tau,$$

where $\boldsymbol{u} = \{\dot{\mathbf{G}}^h, \boldsymbol{\omega}\}^T$ and the convolution kernel matrix is given by

$$K(t) = \frac{1}{\pi}\,\mathrm{Re}\left(\int_{-\infty}^{\infty}(\mathcal{S}^s(\omega) - \mathcal{S}^s(\infty))e^{i\omega t}d\omega\right). \tag{3.32}$$

Nevertheless, a large number of ship dynamics computations performed in the time domain (*e.g.*: maneuvering problems) are based on the assumption that the dynamics of a ship is dominated by a single characteristic frequency (usually the frequency of the sea waves around the ship), and that the damping and added mass matrices coefficients can be considered constant. Although this assumption is not correct, it is a reasonable approximation for the rowing boat problem. In most of the computations we will then use the assumptions of constant $\mathcal{M}^s$ and $\mathcal{S}^s$. To determine the effects of such an assumption, we will compare this computations with those from a simulation in which the convolution integral is used.

### 3.3.4 Time advancing strategy

The final dynamical system (2.4) now becomes

$$\dot{\boldsymbol{y}} = \left(\widehat{M}(t)\right)^{-1}\widehat{\boldsymbol{F}}(\boldsymbol{y}, t). \tag{3.33}$$

where

$$M(t) = \begin{bmatrix} [I] & 0 \\ 0 & [\mathcal{M}(t) + \mathcal{M}^s] \end{bmatrix}, \qquad \boldsymbol{y} = \begin{Bmatrix} \mathbf{G}^h \\ \boldsymbol{u} \end{Bmatrix}, \qquad \widehat{\boldsymbol{F}}(\boldsymbol{y}, t) = \begin{Bmatrix} \dot{\mathbf{G}}^h \\ \widehat{\boldsymbol{f}} \end{Bmatrix}$$

When the assumption of constant $\mathcal{S}^s$ and $\mathcal{M}^s$ is made, one obtains

$$\mathcal{M}^s = \mathcal{M}^s(\tilde{\omega}), \qquad \widehat{\boldsymbol{f}}(\boldsymbol{y}, t) = \boldsymbol{f}^i + \begin{Bmatrix} \boldsymbol{F}^m \\ \boldsymbol{M}^m \end{Bmatrix} + \mathcal{S}^s(\tilde{\omega})\boldsymbol{u}$$

where $\tilde{\omega}$ is the rowers motion frequency, $\boldsymbol{f}^i$ is the sum of all the inertial forces and moments acting on the hull, defined in equation (2.3), and $\{\boldsymbol{F}^m\boldsymbol{M}^m\}^T$ is the vector of the forces related to the mean motion, as defined in equation (3.20).

On the other hand, whenever the damping and added mass matrices are not considered constant in the frequency domain, the coefficients of the system read

$$\mathcal{M}^s = \lim_{\omega \to \infty} \mathcal{M}^s(\omega), \qquad \widehat{\boldsymbol{f}}(\boldsymbol{y}, t) = \boldsymbol{f}^i + \left\{ \begin{array}{c} \boldsymbol{F}^m \\ \boldsymbol{M}^m \end{array} \right\} + \mathcal{S}^s(\infty)\boldsymbol{u} + \int_0^\infty K(\tau)\boldsymbol{u}(t-\tau)d\tau \quad (3.34)$$

with the convolution kernel $K(\tau)$ defined in equation (3.32). The latter is computed using a set of damping matrices obtained by the resolution of system (3.24) for a suitable range of frequencies. The computation is performed using an Inverse Fast Fourier Transform algorithm. The resulting convolution kernel matrix is defined in the time domain on a set of $N_{conv}$ equally spaced points $0 \leq t_i \leq T_{conv}$ , $i = 1, \ldots, N_{conv}$, where the time $T_{conv}$ is chosen so that $k(T_{conv}) \simeq 0$. In practice, the value of $T_{conv}$ typically is 5 s, while the number $N_{conv}$ of employed points is usually 1024.

Because the mesh points on which the convolution kernel, $k(t_i)$ are defined in the time domain does not necessarily coincide with the computational points of the Runge–Kutta–Fehlberg 45 time advancing scheme that is used here, it is necessary to interpolate the convolution kernel and obtain its values at each time step previously computed. The resulting values are multiplied by the corresponding velocity values, and finally integrated by means of the trapezoidal rule, to compute the integral in equation (3.34).

### 3.3.5 Validation

Fig. 3.7 illustrates the frequency dependence of the added mass and damping heave coefficients for a four rowers hull. The curves shown are characterized by a non physical large high frequency oscillation, which is most likely due to the kind of far field Sommerfeld radiation boundary condition (3.24e). Such a condition is devised for planar wave dampers, and can work correctly for an axisymmetric case (such as the immersed hemisphere case discussed above), but appears to be not suitable for the case of a very elongated body like a rowing boat. The oscillations, which are also present in all other elements of the matrices, are not particularly high in the range of frequencies at which the athletes normally row. In fact, the range of rowing cadence between $r = 30 \ \dfrac{\text{strokes}}{\text{min}}$ and $r = 40 \ \dfrac{\text{strokes}}{\text{min}}$ roughly corresponds to the region between $\omega = 3$ rad/s and $\omega = 4$ rad/s in the plots. Over this range, the high

frequency oscillations seem to have a lower amplitude. For this reason, it is still possible to use the matrices computed by solving Equation (3.24), as constant values to be plugged in the rowing boat equations of motion. On the other hand, due to the presence of the high frequency oscillations, the impulse response function obtained from the damping matrix is not correct, so that the convolution term in Eq. (3.34) cannot be evaluated accurately, resulting in diverging simulations. Thus, in the simulations using this model, that will be presented in this work, the assumption of constant damping and added mass matrices is always made.

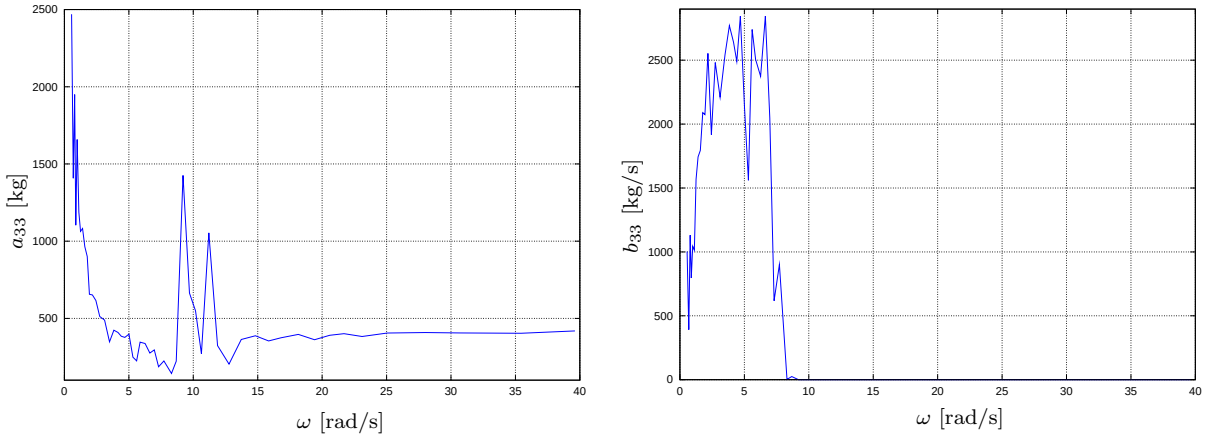


Figure 3.7: Heave added mass (left plot) and damping (right plot) coefficients for a four hull, as a function of the angular frequency $\omega$.

To validate the dynamical model described above, we simulated actual World Championship races for two different boat classes. The first case is that of a female light-weight single scull, with the rower having a mass of 60 Kg. For this test, the horizontal and vertical components of the oarlock forces are set to realistic values of 1100 N and 100 N respectively, and the stroke rate is set to 30 strokes per minute. The computed mean surge velocity is 4.51 m/s, which results in a time of $7:24$ mins needed to complete a 2000 m race. This time is 3% less than $7:36$ mins; the time of the winner of this boat class in the 2009 World Championship in Poznan, Poland. The second test case is that of a coxless four. For this boat, we considered four rowers of 85 Kg each, rowing at the pace of 36 strokes per minute with horizontal and vertical components of the oarlock force set at 1300 N and 100 N respectively. The resulting mean surge velocity is 5.52 m/s, corresponding to a race completion time of

6 : 02 mins, within 1% of 6 : 07 mins which is the time of the winning crew in the 2009 World Championship.

### 3.3.6 Simulation results

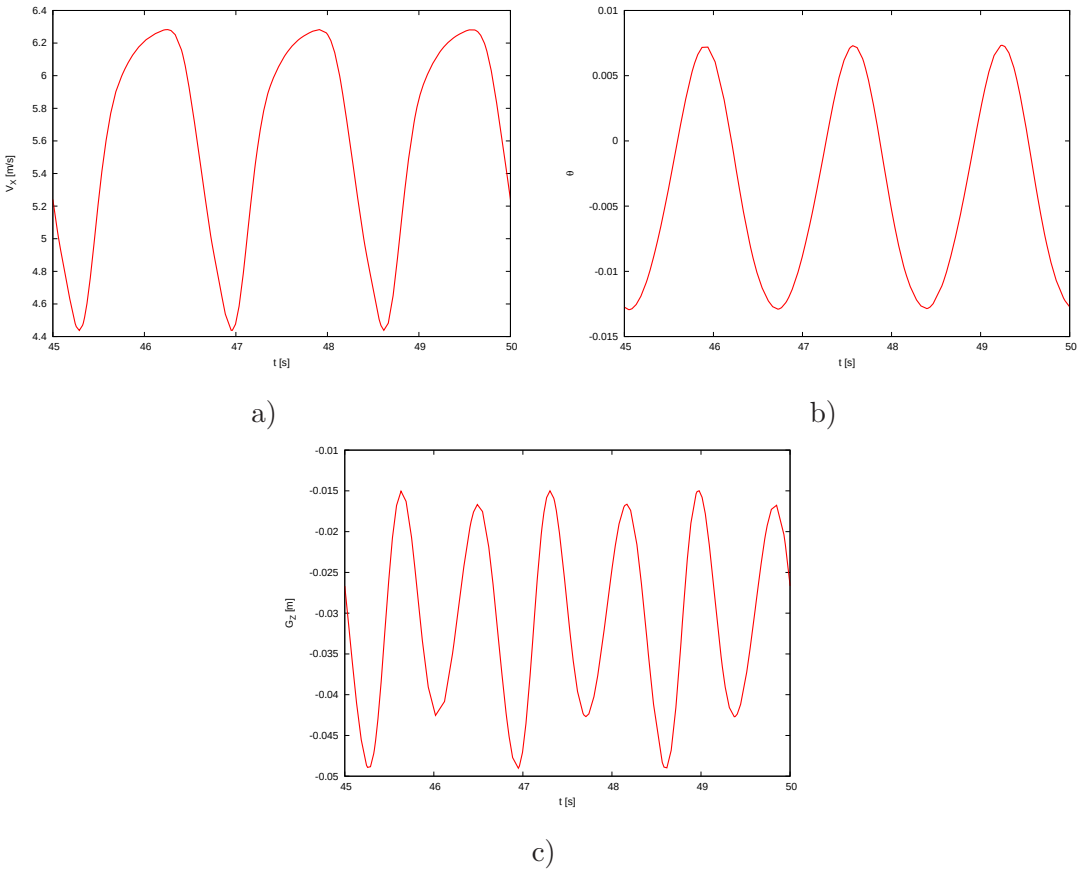


Figure 3.8: Computed time histories of boat motions in the vertical plane as obtained from coupling 3D potential model and rowing boat dynamical model. The plots show the boat motions in the symmetrical degrees of freedom. Plot a) shows the time history of the boat surge velocity, plot b) depicts the time evolution of the pitch Euler angle, and plot c) shows the time history of the hull vertical position.

Results from a coxless four case are presented in Fig. 3.8. In this simulation, the system parameters are set to the same values considered in the RANS symmetrical simulations. The coxless four is pushed at the pace of 36 $\frac{\text{strokes}}{\text{min}}$ by athletes having a body mass of 80 kg

each. The maximum horizontal and vertical components of the oarlock forces of each rower are set to 1200 N and 200 N respectively. The qualitative behavior is in good agreement with the previous RANS simulations (detailed comparisons will be presented in Section 3.5). Fig. 3.8 (a) shows the the time history of the boat surge velocity. As in the case of the RANS simulations, the velocity oscillates between a minimum value of 4.4 m/s and a maximum value of 6.3 m/s, and the peak speed is obtained during the recovery phase, in which the rowers are moving backwards with respect to the hull. Fig. 3.8 (b), shows the time history of the pitch angular Euler angle $\theta$. Also, with this reduced-order model, the computed pitch angle is negative during the catch phase of each stroke, in which the rowers reach the backward limit of their motion on the boat, causing the bow of the hull to move upwards. The computed $\theta$ values result in bow and stern vertical displacements in the range of $\pm 7$ cm, which are also close to values observed during races. The average pitch angle computed with the reduced-order model is $-0.0038$ rad. The time history of the vertical motion of the hull center of gravity is shown in Fig. 3.8 (c). The plot shows that the oscillation frequency for the heave motion is twice that of the rowers frequency of motion, which is in agreement with the results obtained with the RANS computations. The average heave position of the hull center of gravity is $-3.08$ cm, which is particularly close to the hydrostatic equilibrium position. This model, in fact, does not account for hydrodynamic effects that cause the boat to have a higher sinkage as in the case of the RANS simulations.

The simulations performed with the reduced order model described above take significantly less time then the high fidelity RANS simulation. For a four rowers boat, the simulation of a one minute portion of a race takes less then 5 minutes on a normal laptop, while the time needed to perform the same computation with the RANS model is of the order of a week on six parallel processors of a Linux cluster. Nonetheless, the predicted race completion times are accurate, showing that the reduced order model can be used for quick evaluation of the effect of several parameters on the overall performances.

## 3.4 A potential model based on Strip Theory Approximation

### 3.4.1 Strip theory

The damping and added mass coefficients obtained from the resolution of the three-dimensional potential problem (3.24), have an excessive sensitivity on the oscillation frequency, which makes it particularly difficult to compute the kernel for the convolution term in the equations of motion of the rowing boat. To address this issue and understand the effects of frequency dependent damping and added mass matrices on the boat dynamics, we use a different method, based on the strip theory approximation, for the computation of the damping and added mass coefficients of a boat hull. In the framework of this approximation, the force acting on any section of the hull normal to its longitudinal axis, does not depend on the shape of the boat at all the other sections. The strip theory is based on the observation that, for very elongated hulls, the waves radiated from the ship surface at any section, do not have hydrodynamic interaction with the adjacent sections. Thus, this approximation is accurate for slender boats, and can be reasonably applied to the study of rowing boats.

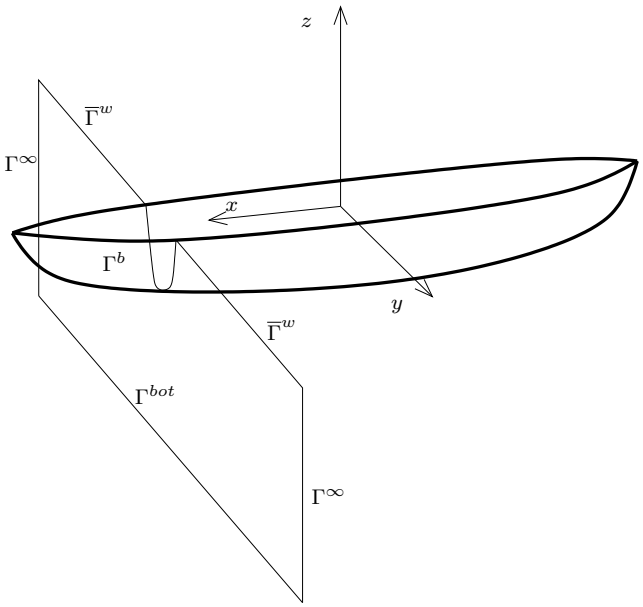


Figure 3.9: A sketch of the numerical domain used in the 2D radiation potential computation.

To compute the radiation forces acting on the hull, the flow domain is decomposed into

a finite set of two dimensional sections as illustrated in Fig. 3.9. For each of these sections, the radiation potential problem (3.24) is solved in a two dimensional domain, reducing the the model's number of unknowns and avoiding the problems with the radiation boundary condition.

### 3.4.2 PDStrip testing and implementation

The two dimensional radiation potential problems have been solved by means of the open source software PDStrip, which employs a patch method for the discretization of the Laplace equation ((14; 32)), based on the superimposition of the elementary potential fields due to point wise sources, placed in proximity of the domain boundary. The intensities of the sources are chosen so that the potential resulting from the sum of the potential due to each source, fulfills the boundary conditions of the radiation problem. Once the potential is known, the radiation forces on the body are computed in a similar manner to the three-dimensional case.

In the framework of the strip theory, the boat surface in each two dimensional section can only move along three degrees of freedom, namely the sway ($y$ motion), heave ($z$ motion) and roll ($\phi$ rotation) motions. All other three-dimensional motions are either not contained in the section plane ($x$ motion) or can be recast in the three degrees of freedom described above ($\theta$ and $\psi$ rotations). Thus, the results of the two dimensional problems computation are $3 \times 3$ damping and added mass matrices with coefficients that depend on the $x$ coordinate, namely

$$A^{2D} = \begin{bmatrix} a_{22}^{2D} & a_{23}^{2D} & a_{24}^{2D} \\ a_{32}^{2D} & a_{33}^{2D} & a_{34}^{2D} \\ a_{42}^{2D} & a_{43}^{2D} & a_{44}^{2D} \end{bmatrix} \qquad \text{and} \qquad B^{2D} = \begin{bmatrix} b_{22}^{2D} & b_{23}^{2D} & b_{24}^{2D} \\ b_{32}^{2D} & b_{33}^{2D} & b_{34}^{2D} \\ b_{42}^{2D} & b_{43}^{2D} & b_{44}^{2D} \end{bmatrix},$$

in which the indices of the matrices components coincide with the indices used for the three-dimensional case. The two dimensional damping and added mass coefficients obtained for each section must be integrated over the boat length $L$ to obtain the three-dimensional coefficients, which in the case of the added mass matrix read

$$\mathcal{M}^s = \begin{bmatrix} 0 & 0 & 0 & 0 & 0 & 0 \\ 0 & \int_0^L a_{22}^{2D}(x)dx & \int_0^L a_{23}^{2D}(x)dx & \int_0^L a_{24}^{2D}(x)dx & \int_0^L a_{23}^{2D}(x)xdx & \int_0^L a_{22}^{2D}(x)xdx \\ 0 & \int_0^L a_{32}^{2D}(x)dx & \int_0^L a_{33}^{2D}(x)dx & \int_0^L a_{34}^{2D}(x)dx & \int_0^L a_{33}^{2D}(x)xdx & \int_0^L a_{32}^{2D}(x)xdx \\ 0 & \int_0^L a_{42}^{2D}(x)dx & \int_0^L a_{43}^{2D}(x)dx & \int_0^L a_{44}^{2D}(x)dx & \int_0^L a_{43}^{2D}(x)xdx & \int_0^L a_{42}^{2D}(x)xdx \\ 0 & \int_0^L a_{32}^{2D}(x)xdx & \int_0^L a_{33}^{2D}(x)xdx & \int_0^L a_{34}^{2D}(x)xdx & \int_0^L a_{33}^{2D}(x)x^2dx & \int_0^L a_{32}^{2D}(x)x^2dx \\ 0 & \int_0^L a_{22}^{2D}(x)xdx & \int_0^L a_{23}^{2D}(x)xdx & \int_0^L a_{24}^{2D}(x)xdx & \int_0^L a_{23}^{2D}(x)x^2dx & \int_0^L a_{22}^{2D}(x)x^2dx \end{bmatrix}, \quad (3.35)$$

and

$$\mathcal{S}^s = \begin{bmatrix} 0 & 0 & 0 & 0 & 0 & 0 \\ 0 & \int_0^L b_{22}^{2D}(x)dx & \int_0^L b_{23}^{2D}(x)dx & \int_0^L b_{24}^{2D}(x)dx & \int_0^L b_{23}^{2D}(x)xdx & \int_0^L b_{22}^{2D}(x)xdx \\ 0 & \int_0^L b_{32}^{2D}(x)dx & \int_0^L b_{33}^{2D}(x)dx & \int_0^L b_{34}^{2D}(x)dx & \int_0^L b_{33}^{2D}(x)xdx & \int_0^L b_{32}^{2D}(x)xdx \\ 0 & \int_0^L b_{42}^{2D}(x)dx & \int_0^L b_{43}^{2D}(x)dx & \int_0^L b_{44}^{2D}(x)dx & \int_0^L b_{43}^{2D}(x)xdx & \int_0^L b_{42}^{2D}(x)xdx \\ 0 & \int_0^L b_{32}^{2D}(x)xdx & \int_0^L b_{33}^{2D}(x)xdx & \int_0^L b_{34}^{2D}(x)xdx & \int_0^L b_{33}^{2D}(x)x^2dx & \int_0^L b_{32}^{2D}(x)x^2dx \\ 0 & \int_0^L b_{22}^{2D}(x)xdx & \int_0^L b_{23}^{2D}(x)xdx & \int_0^L b_{24}^{2D}(x)xdx & \int_0^L b_{23}^{2D}(x)x^2dx & \int_0^L b_{22}^{2D}(x)x^2dx \end{bmatrix}. \quad (3.36)$$

The first row and column of both matrices are composed of zeros, since in the strip theory approximation the longitudinal forces acting on the hull are completely neglected.

As the output generating part of the PDStrip source code was completely rewritten to obtain more manageable output files, a simple test case with results available from the literature was performed to understand the output conventions of PDStrip, and to check the correctness of the re-implemented source code parts, as well as the accuracy of the software solution. The test case considered is the study of heave radiative properties of an infinite cylinder having a rectangular section with a beam over draft ratio, $B/T = 2$. Experimental results for this geometry have been provided by Vugts (2). Fig. 3.10 (a) shows a comparison between computed (blue line) and measured (red line) heave added mass coefficients of an infinite cylinder. Fig. 3.10 (b) depicts the same comparisons for the heave damping coefficients. In both plots, the computed curves are in good qualitative and quantitative agreement with the experimental ones.

The next geometry considered is that of a Wigley hull, a hull shape defined according to the following analytical equation

$$Y_{Wh}(X,Z) = \frac{B}{2}\left(1-\left(\frac{Z}{T}\right)^2\right)\left(1-\left(\frac{2X}{L}\right)^2\right) \qquad -L/2 \leq X \leq L/2, \quad -T \leq Z \leq 0,$$

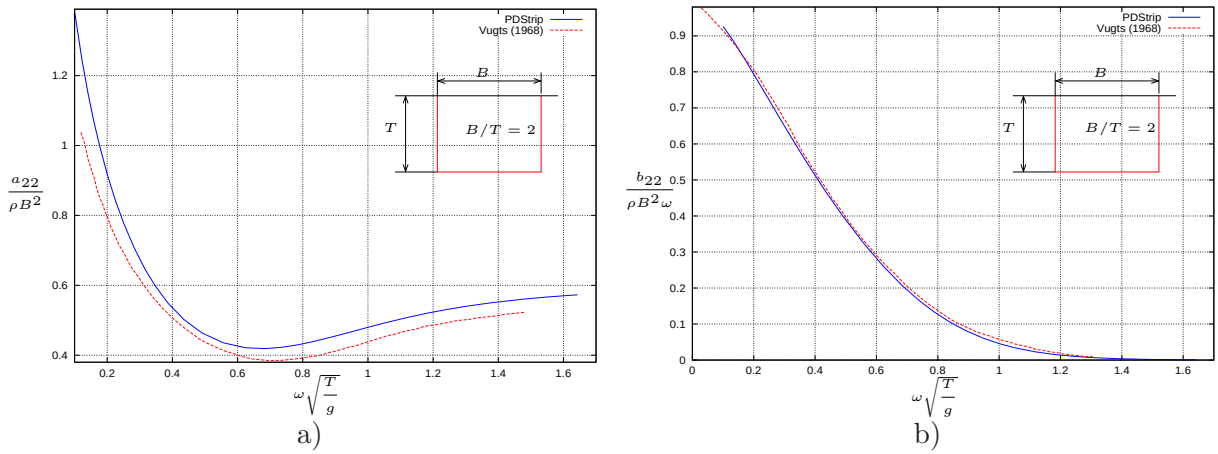


Figure 3.10: Heave added mass (a) and damping (b) coefficients for an infinite square section cylinder. The blue curves refer to the present work, while the red curves refer to results from experiments of Vugts (2).

where $L$ is the length of the hull, $B$ is its breadth and $T$ is its draft. Due to its simple geometrical definition, the Wigley hull is commonly used as a benchmark for numerical methods for the resolution of equations describing the ship induced waves. The radiation properties of a Wigley hull have been measured in experiments conducted by Gerritsma (3), providing a basis for comparing numerical results. In the experiments, the length, beam and draft of the boat were respectively $L = 5$ m, $B = 0.5$ m and $T = 0.3125$ m. A sketch of the 25 sections in which the Wigley hull has been divided is presented in Fig. 3.11.

Fig. 3.12 shows comparisons of the experimental data (red dots) with results obtained form PDStrip (blue continuous curves). Fig. 3.12 (a) depicts plots of non dimensionalized added mass coefficients for the heave motion as a function of non dimensionalized frequency. The agreement with the measurements appears qualitatively good, with smaller quantitative differences over the higher frequencies. The heave damping coefficient comparison presented in Fig. 3.12 (b) shows that the strip theory solution substantially overpredicts the experimental data. Yet, it is able to reproduce the qualitative behavior and the slope of the experimental curve. The pitch added mass coefficients illustrated in Fig. 3.12 (c) show once again a satisfying qualitative agreement with the experimental data, but an under prediction of the latter. Finally, as it is the case with the heave damping coefficient, the pitch damping

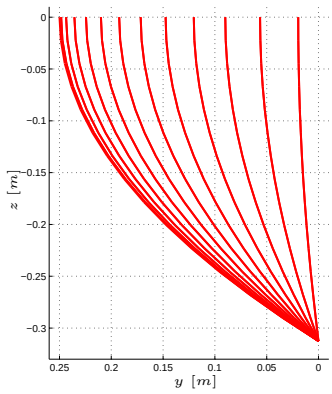


Figure 3.11: A front view of the 25 strips dividing the surface of a Wigley hull.

coefficient is also over predicted, as shown in Fig. 3.12 (d). Thus, the results are qualitatively good, although quantitative differences are evident. Nonetheless, the curves computed with strip theory are in closer agreement with equivalent numerical results presented by Newman in 1991 (33), in which both heave and pitch experimental added mass coefficients are slightly under predicted, while the corresponding damping coefficients are over predicted. Quantitative differences with the experimental data could also be explained with the fact that, in the experiments by Gerritsma, the Wigley hull was advancing in the water at a constant speed. The influence of the wave field due to the surge motion, on the radiation properties of the boat are in fact not accounted for in a linearized model such as the strip theory.

Fig. 3.13 presents a comparison between the Wigley hull heave damping and added mass coefficients computed with PDStrip and by solving the 3D radiation potential problem (3.24). The heave added mass plot (Fig. 3.13 (a)) shows that the values computed with the two methods are somehow similar, with the 3D potential problem solution showing the high frequency oscillations as noticed for the rowing boat hull case previously discussed. Also, the heave damping coefficient values presented in Fig. 3.13 (b) show that the frequency dependence of the 3D potential solution is not correctly predicted, while the strip theory solution presents a smoother behavior. It is worth noting that for the frequency range used by the athletes in their rowing action (which is between $r = 30\ \dfrac{\text{strokes}}{\text{min}}$ and $r = 40\ \dfrac{\text{strokes}}{\text{min}}$, corresponding to to the region between $\omega\sqrt{L/g} = 2$ and $\omega\sqrt{L/g} = 3$ in the plots), both

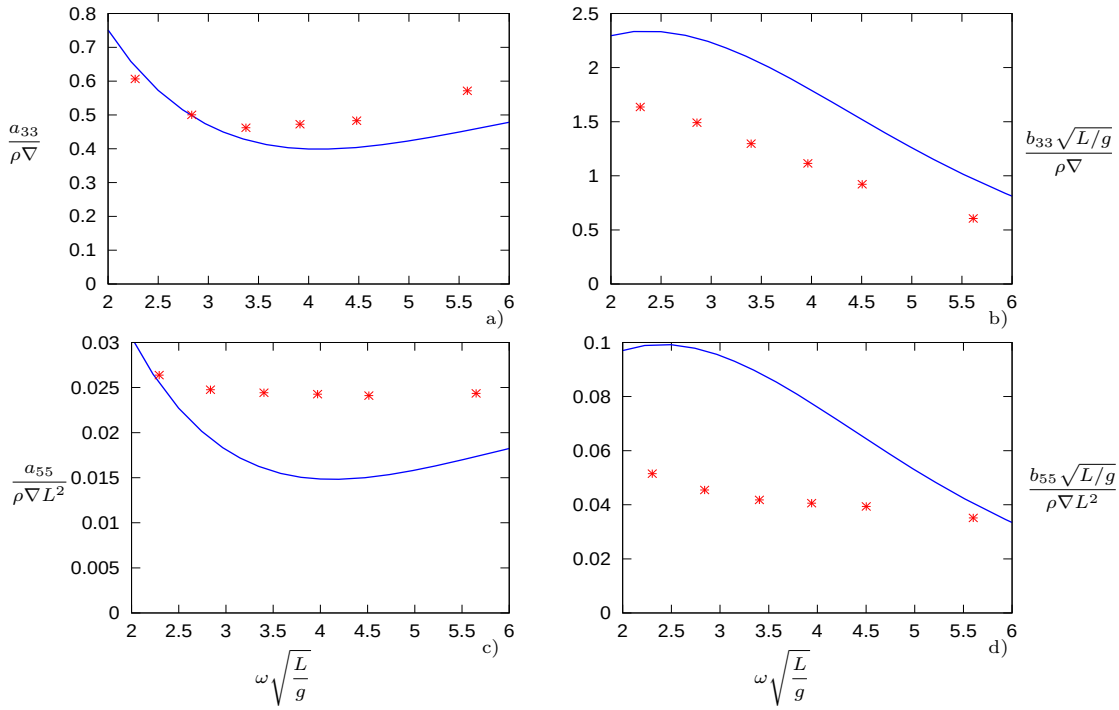


Figure 3.12: Comparison of a Wigley hull heave and pitch added mass and damping coefficients obtained by strip theory computation and by experiments (3). The four plots depict: a) Heave added mass; b) Heave damping; c) Pitch added mass; d) Pitch damping. The colors indicate: * Experiments, — Strip Theory.

the damping and added mass values obtained with the 3D potential are particularly close to the corresponding strip theory values. For this reason, under the assumption of constant added mass and damping matrices, it is reasonable to use the 3D potential values in the resolution of the rowing boat dynamical system. On the other hand, to analyze the effects of the frequency dependence of the radiative coefficients, it is necessary to use values obtained with the strip theory, which allow for the computation of the kernel for the convolution term in the rowing boat dynamical system.

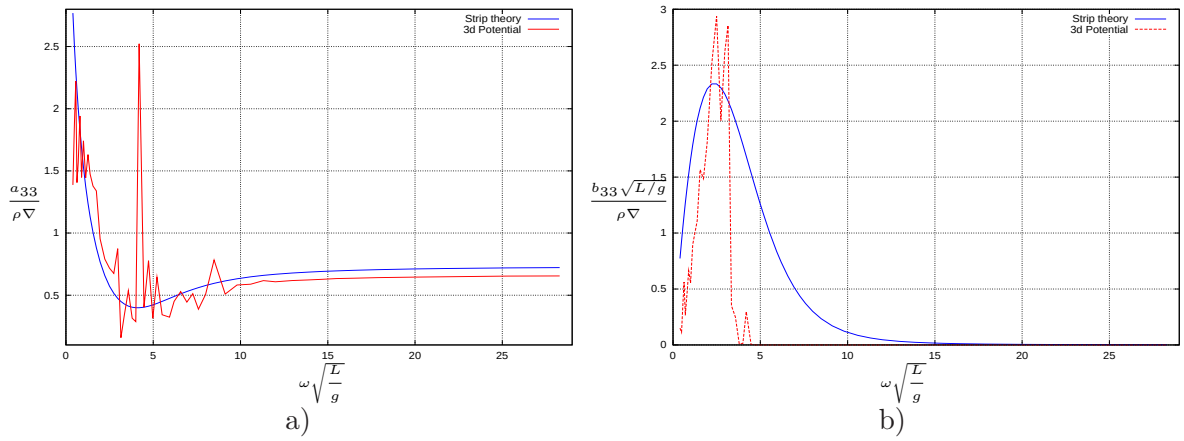


Figure 3.13: Comparison of non dimensionalized Wigley hull heave and pitch added mass and damping coefficients by strip theory computation and by experiments (3). Plot a) depicts non dimensional heave added mass coefficient as a function of non dimensional frequency. Plot b) shows non dimensional heave damping coefficients as a function of non dimensional frequency. The colors indicate: — Strip Theory, — 3D Potential.

### 3.4.3 Simulations combining PDStrip and dynamical system

As hull radiative coefficients computed with strip theory present a smooth dependence on the oscillation frequency, they can be conveniently used for the computation of the convolution integral in Equation (3.34). For this reason, the rowing boat hull damping and added mass coefficients computed with PDStrip have been used to investigate how accounting for memory effects of fluid dynamic forces affects the predicted motions of the boat. As in the case previously considered with the RANS model in Sec. 3.2.3, the symmetric simulations reproduce the dynamics of a coxless four pushed at a pace of 36 $\frac{\text{strokes}}{\text{min}}$ by four rowers each with a height of 1.80 m and a body mass of 80 kg. For each rower, the maximum horizontal and vertical oarlock force is set to 1200 N and 200.0 N respectively.

Fig. 3.14 shows a comparison between the boat motions computed assuming frequency dependent damping and added mass matrices (red curves), and assuming constant radiative coefficients. The surge velocity plot in Fig. 3.14 (a) suggests that the two solutions have very similar mean forward speeds. The convolution solution has in fact a slightly lower mean velocity value, 5.6207 m/s, in comparison with the 5.6232 m/s velocity computed with

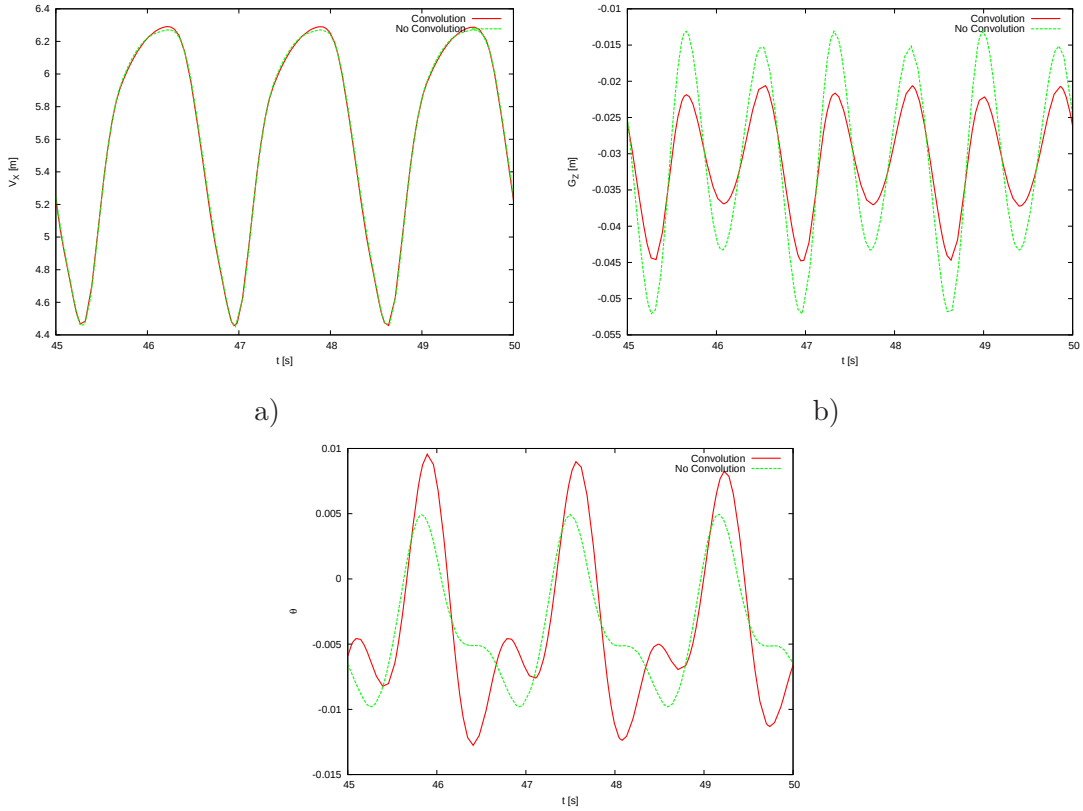


Figure 3.14: Comparison of a coxless four symmetric motion computed with convolution (—) and no convolution (—). Plot a) shows the surge velocity time history. Plot b) depicts the hull center of gravity vertical motion. Plot c) shows the time history of the hull pitch Euler angle.

constant added mass and damping matrices. The time history of the vertical position of the hull gravity center (Fig. 3.14 (b)) shows that, when memory effects are considered, the amplitude of the heave motion is substantially reduced with respect to the constant radiative coefficients simulations. This reduced amplitude of motion on the heave degree of freedom is not due to an increase of the damping in the system, but to the fact that part of the energy taken from the heave motion is passed to the pitch motion. Fig. 3.14 (c), depicting the time history of the pitch Euler angle, shows that the convolution solution presents a significantly higher amplitude of motion on this degree of freedom. In addition, the convolution integral

seems to be introducing a slight delay in the water force reacting to the pitch motion. It is particularly evident in the lower portion of the plot, how the delay in the hydrodynamic reaction results in a slightly different time history.

## 3.5 Comparison of model results

To assess the performances of all the fluid dynamic models discussed, we compare time histories of motions from the different models. Particularly, we evaluate to what extent the solutions obtained with the low fidelity models are able to accurately reproduce motions predicted with the high fidelity. In fact, the RANS equations are accounting for all the most important physical features of the flow past a rowing boat, and the solutions obtained with such model will be used as a benchmark to validate the other reduced order models.

The test case considered is that of the coxless four under symmetrical load configuration discussed in Sec. 3.2.3, Sec. 3.3.6, and Sec. 3.4.3, in which the four rowers, each with a weight of 80 kg, row at the pace of 36 $\frac{\text{strokes}}{\text{min}}$ with maximum horizontal and vertical oarlock force is set to 1200 N and 200.0 N respectively. For this case, the coefficients for the drag due to the mean motion in Equation (3.21), have been calibrated by means of a steady state RANS simulation with fixed vertical position corresponding to the hydrostatic sinkage. The resulting drag coefficients have been obtained using the hydrostatic wet surface as the reference surface in Equation (3.21).

Results from different simulations are displayed in Fig. 3.15, which contains plots of the time histories of the motions of the three degrees of freedom in the symmetry plane. The red curves in the plot show results obtained using the RANS fluid dynamic model, the green curves show results of the 3D potential model, the blue curves show the results obtained with strip theory, and the magenta curves show the results obtained by means of the strip theory and the computation of the convolution integral.

The surge velocity plots (Fig. 3.15 (a)) show good agreement among all methods considered. As can be seen in the graph, the velocity predicted with the RANS model is slightly lower than those obtained with the the reduced order model. The mean velocity, as computed between the 10th and the 15th second of the RANS simulations is in fact 5.5926 m/s, while

the corresponding values for the reduced order models are 5.6323 m/s for the 3D potential, 5.6305 m/s for the strip theory model, and 5.6275 m/s for the strip theory model with convolution. The differences among the mean velocity values predicted with RANS model, and those obtained with reduced order models are all lower then 0.7%. As the forward velocity is the most important performance parameter, it is very encouraging to realize that all low fidelity models considered are able to reproduce in computations of few minutes the results of high fidelity simulations lasting several days.

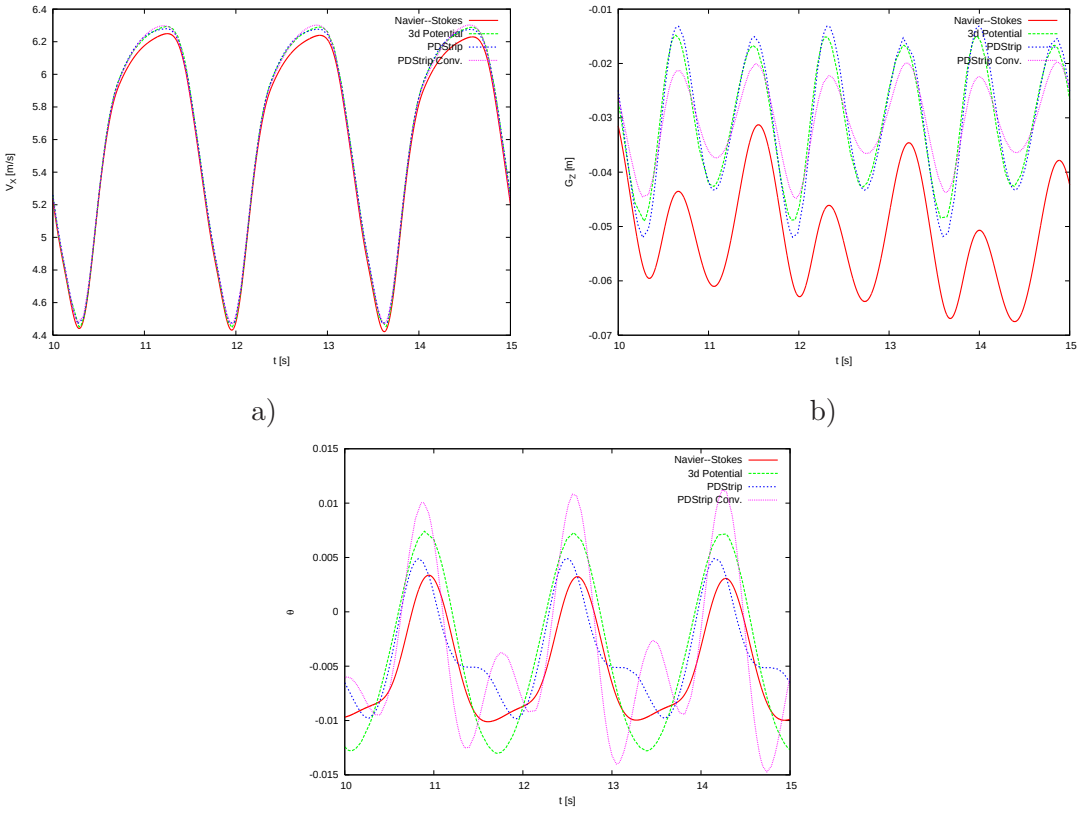


Figure 3.15: Comparison a coxless four symmetric motion computed with the different fluid dynamic models considered in this work. The curves represent: — RANS, – – 3D potential, - - - Strip theory, · · · Strip theory with convolution. Plot a) shows the time history of the the surge velocity. Plot b) depicts the vertical motion of the hull center of gravity. Plot c) shows the time history of the hull pitch Euler angle.

Fig. 3.15 (b) shows plots of the time history of the vertical position of the hull gravity center. Here all the curves seem to have similar amplitudes, but the agreement between RANS and reduced-order model values is less evident. In particular, the RANS heave curve seems to settle around vertical positions which are approximatively 1.5 cm lower then the corresponding positions computed with the reduced-order models. This difference is somehow expected, as in the reduced-order models the vertical force is purely a hydrostatic buoyancy force, while the RANS model also accounts for hydrodynamic effects. Due to the acceleration of the flow past the obstacle, and the associated pressure drop. This hydrodynamic effect leads to a reduction in the lift, and to an equilibrium position characterized by a higher sinkage. The boat is then advancing in the water with a lower vertical position, and a higher wet surface, which could also explain why the RANS simulation predicts sightly higher drag, and slightly lower velocities. Another factor which might contribute to the lower vertical equilibrium position observed in the RANS simulations, is the presence of the parasite wave discussed in Sec. 3.2.3. In the presence of such a low frequency wave, the boat vertical response basically tracks the wave height, which as can be seen in Fig. 3.3, for $t = 15$ s is approximatively 1 cm lower than the undisturbed free surface. Thus, the two effects described might combine and lead to the prediction of lower values for the boat vertical position, when the RANS model is used.

The time histories of the pitch Euler angle, presented in Fig. 3.15 (c), show similar values of average pitch angles. In fact, the mean pitch angle obtained with the RANS simulation is $-0.0051$ rad, while the corresponding values obtained from the reduced-order models are $-0.0038$ rad for the 3D potential model, $-0.0036$ rad for the strip theory model, and $-0.0037$ rad for the strip theory model with the convolution integral. The higher absolute value of the mean pitch angle predicted with RANS model is not surprising, as this model accounts for the presence of the mean motion wave field, generating a negative pitch moment which is neglected in the linearized models. Nonetheless, the predictions of the reduced-order models are not far from the RANS predictions. As for the amplitudes of the pitch angle curves, all the reduced-order models somehow over predict the RANS results. This could be related to the fact that the RANS model accounts for viscous damping, which becomes particularly significant when the bow and extremely sharp stern of the boat enter in the

water. The reduced order models, by neglecting this non vanishing viscous damping term, end up overestimating the pitch amplitude of motion. In addition, as can be seen in the lower part of the plot, corresponding to the moment in which the stern is immersed in the water surface, these models are not able to effectively damp the forces exerted by the rowers, and the pitch angle curves present oscillations that are not present in the corresponding RANS model plots.

The other test case considered is that of the coxless four under non symmetrical load configuration as discussed in Sec. 3.2.3. Here, the crew is composed of four rowers, each with a weight of 80 kg, and rowing at the pace of 36 $\frac{\text{strokes}}{\text{min}}$. The first rower maximum horizontal oarlock force is set to 1212 N, and the vertical oarlock force to 202 N, while the maximum horizontal and vertical forces of the other rowers are set to 1200 N and 200 N respectively. Since in this sweep boat, the first rower is rowing on the starboard side of the boat, the load configuration described results in a force unbalance between the two sides of the boat, yielding nonzero values of mean yaw and roll angles and sway motion.

Fig. 3.16 shows a comparison of the boat motions with non symmetrical oarlock forces as computed with the different fluid dynamic models discussed above. Fig. 3.16 (a) compares the surge velocity time history in the last 5 s of the simulation. As in the symmetric case, the surge velocity history computed using reduced-order models is in close agreement with the corresponding history obtained with the high fidelity model. The mean forward velocity predicted using the 3D potential method is 5.6218 m/s, the corresponding value obtained with the strip theory model is 5.6323 m/s, while the velocity computed using the strip theory model with convolution is 5.6314 m/s. All these values are slightly higher than the 5.5969 m/s velocity predicted using the RANS model. Yet, once again the differences between high fidelity and reduced-order model results are all lower than 0.7%. Fig. 3.16 (b) shows plots of the full time history of the hull sway velocity computed. In this case, the agreement between time histories from RANS and reduced order models is less satisfactory. As expected, the RANS model simulation seems to result in a relatively higher sway velocity. This velocity yields, in the 15 s time span, a lateral displacement of 8.85 cm, which is considerably higher then the values of 2.59cm, 3.16cm, 0.46 cm respectively obtained with the 3D potential model, PDStrip, and PDstrip with convolution. This difference in the sway velocities is

consistent with the differences observed in the predicted yaw motion, as illustrated in Fig. 3.16 (c). In the plot, which shows the full time history of the hull yaw angle, it is evident that in RANS simulation the hull is evolving towards a sensibly higher yaw angle, with respect to the reduced order model. This is probably due to the fact that, in presence of a yaw angle, the boat hull generated a lateral force and a yaw moment, acting as a symmetric

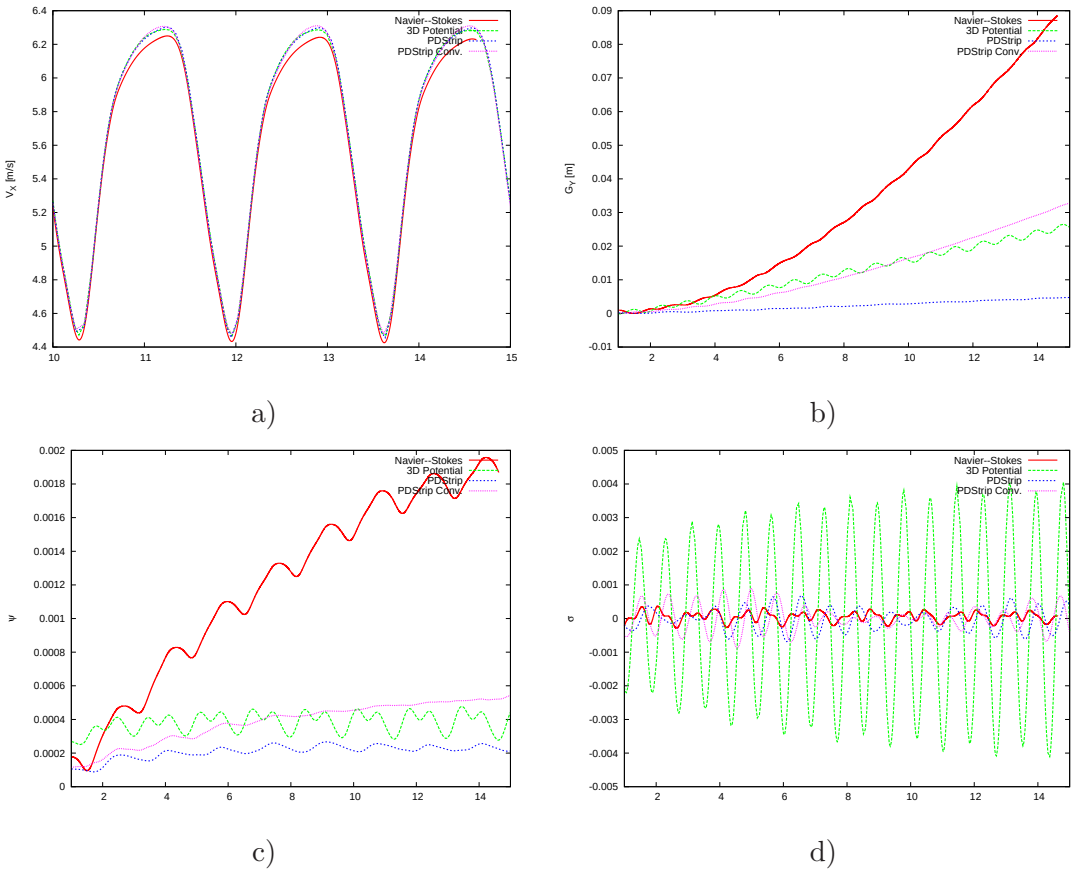


Figure 3.16: Comparison a coxless four time histories with non symmetric oarlock forces as computed with the different fluid dynamic models considered in this work. The curves represent: — RANS, – – 3D potential, - - - Strip theory, · · · Strip theory with convolution. Plot a) shows the last five seconds of the surge velocity time history. Plot b) depicts the full time history of the hull center of gravity sway motion. Plot c) shows the full time history of the hull yaw Euler angle. Plot d) shows the last five seconds of the time history of the hull roll Euler angle.

airfoil with a nonzero angle of attack. This mechanism is correctly reproduced in the RANS simulations, but is neglected in the reduced order models, in which the damping and added mass matrix are obtained setting the hull in oscillation in still water. Thus, we can infer that introducing forward speed correction factors (see (33)) to obtain radiation coefficients accounting for the boat surge motion, would improve the quality of the reduced order models results. Fig. 3.16 (d) shows the time history of the hull roll angle $\phi$ both for high fidelity and reduced-order simulations. The plot shows that most of the models considered present very similar amplitudes of motion in the roll degree of freedom. Only the 3D potential model time history has a considerably higher amplitude than histories obtained with the other models. In fact, this might be related to a possible over prediction of the roll and surge cross-coupling damping and added mass coefficients, which leads to an energy transfer from the surge mode, to the roll one. The mean roll angles computed with the reduce order models are $-7.37 \cdot 10^{-5}$ rad for the 3D potential model, $-4.20 \cdot 10^{-5}$ rad for the strip theory, and $-4.84 \cdot 10^{-5}$ rad. These value are consistently lower than the $2.75 \cdot 10^{-4}$ rad mean angle observed in the RANS simulation.

The comparisons presented above show that among the results obtained with the reduced order models, the ones that are consistently closer to the RANS values are those obtained with the 3D potential model, and with the strip theory using the convolution integral. This can be explained with the fact that the former model accounts for the longitudinal components of the damping and added mass matrices, which are disregarded in the strip theory models, with the latter accounting for the frequency dependence of the damping and added mass matrices of the hull. Thus, the results of the reduced order models might improve if the convolution integral was computed with radiative coefficients obtained from the 3D potential model. Due to the presence of the high frequency and high amplitude oscillations in the damping and added mass frequency curves, this strategy has not been applied here. Eliminating these oscillations and using the convolution integrals with the 3D potential damping and added mass matrices could be one of the most important areas for improving the reduced-order models.

## 3.6 Summary

In this chapter, multi-fidelity representation of the water forces and moments on the hull are implemented in the solution of the dynamical system formulated in Chapter 2. In summary,

- **The RANS model** has been coupled to the rowing boat dynamical system by means of a forward Euler explicit scheme. To ensure stability, the time steps used for the simulations were kept very small. This fluid dynamic model is able to simulate all the most important features of the flow past a rowing boat, but the simulations require computational times of the order of several days, which make this model not suitable for the a detailed sensitivity analysis and validation as performed in Chapter 4. In addition, the large amplitudes of oscillation of the boat in the surge degree of freedom, are not compatible with the very fine computational meshes needed for the computations. For this reason the RANS computations are performed in a non inertial reference frame which follows the boat only on the horizontal motion. The correspondent source term added to the equations leads to the presence of a parasite wave in the flow domain, which causes inaccurate predictions for vertical position of the boat. For all these reasons, the RANS model has been used in this work as a benchmark to cross-validate other reduced-order models to be used in the sensitivity analysis.

- **The linearized 3D potential** model is based on the decomposition of the fluid dynamic forces into contributions of mean and secondary motions. The former forces are computed by means of coefficients obtained from steady-state RANS simulations. The latter forces are computed by means of damping and an added mass matrices obtained by solving a 3D radiative potential problem. Due to the shape of the boat, the use of Sommerfeld truncation boundary condition does not yield the correct frequency dependence of the radiative coefficients. Thus, the radiative forces are not computed in the time domain problem by means of a convolution integral, accounting for flow memory effects, but have to be computed assuming constant damping and added mass matrices. Nonetheless, the results of this fluid dynamic model are encouraging. With simulations which last less than five minutes, this model is able to predict the values of the most important performance parameters that are in very close agreement with the

parameters obtained using the RANS model.

- **The strip theory model** is also based on the linearized potential model, so as to decompose the force into their mean and secondary motion contributions. In the framework of the strip theory though, the additional assumption of extremely elongated body is made, in order to compute hull radiative properties by means of a series of two dimensional problem, in which the truncation boundary condition is more easily enforced, and the computational cost is reduced. The resulting damping and added mass matrices present smooth frequency dependence and allow for the use of the convolution integral to compute the radiative forces in the time domain. For this reason, this model has been used to assess the importance of memory effects in the estimation of radiative forces. The results are very similar to the 3D potential model results. They also show that accounting for memory effects significantly improves the agreement between the strip theory and the RANS predictions. Further improvements could be obtained by introducing corrections to account for longitudinal radiative forces, which are completely neglected in the strip theory.

# Chapter 4

# Sensitivity analysis of rowing boat motions

A typical output obtained using the reduced-order models as described above, and that illustrates the dependency of the boat motion on input parameters, is presented in Fig. 4.1. In this figure, time histories of the forward and vertical velocities for two different configurations of a light-weight single boat are compared. In the first configuration, the maximum horizontal and vertical components of the oarlock force are set to 1100 N and 100 N respectively. In the second configuration, these forces are increased to 1200 N for the horizontal component and 120 N for the vertical one. The results show that the change in the input parameters has a significant influence on the forward velocity, and in particular on its mean value, which increases as the magnitude of the the forces is increased. In contrast, the vertical velocity does not seem to be significantly affected by the increase in the magnitude of the the forces.

More generally, the input parameters for this model would include boat geometry and hull shape, density of water, the rowers weights and heights, cadence of motion, and magnitudes of the forces exerted on the oarlocks. The effects of varying these parameters might combine nonlinearly. This combination renders the assessment of the importance of any of these parameters to the boat motions particularly difficult. To address this issue, the model for the rowing boat dynamics is complemented with a sensitivity analysis framework. In this framework, variations in the input parameters are introduced and propagated through the

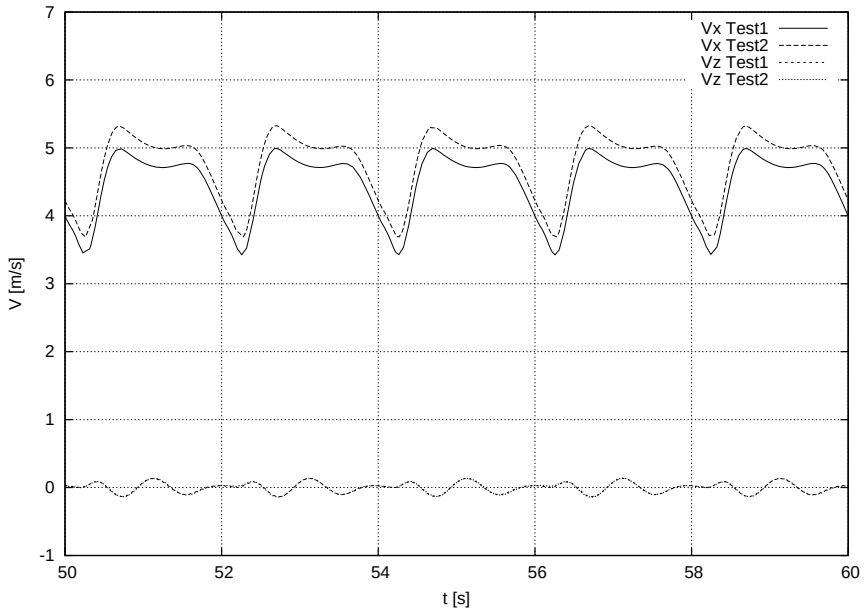


Figure 4.1: Examples of the outputs, representing the time histories of the horizontal and vertical velocities of a light-weight female single scull obtain in the original configuration (Test1), and when both the maximum horizontal and vertical oarlock forces are increased (Test2).

reduced-order model dynamical system, to determine the rate of variation of the output, such as the mean forward velocity or other performance parameters, with variations in input parameters as listed above.

In this chapter we introduce the polynomial chaos expansion (PCE) as the tool employed to perform sensitivity analysis. We also provide details of different implementation strategies of PCE. The case of a female single scull is used to evaluate the performance of these strategies. The PCE expansion provides a simple and yet accurate representation of the relationship between the input parameters and performance indices. This representation gives a better understanding of the physics of the system, and provides qualitative and quantitative information which can be used by rowing boat athletes and coaches in training to improve their performances.

## 4.1 The polynomial chaos expansion

### 4.1.1 Introduction to polynomial chaos expansion

Based on the Karhunen–Loève theorem (34), a stochastic process can be represented in a Fourier-like expansion as an infinite linear combination of random basis functions. Thus, any generic variable $\alpha^*$ can be expressed as follows:

$$\alpha^*(\boldsymbol{x}, t, \boldsymbol{\xi}) = \sum_{i=0}^{\infty} \alpha_i(\boldsymbol{x}, t)\Psi_i(\boldsymbol{\xi}), \tag{4.1}$$

where $\Psi_i(\boldsymbol{\xi})$ is the random basis function of the $i^{th}$ mode, and is a function of the independent random variables represented by the vector $\boldsymbol{\xi}$. $\alpha_i(t, \boldsymbol{x})$ is the $i^{th}$ fluctuation amplitude, that is a function of the deterministic variables $\boldsymbol{x}$ and $t$ (35; 36). We note that $\alpha^*$ is a function of independent deterministic variables $\boldsymbol{x}$ and $t$, and the $n$-dimensional random variable vector $\boldsymbol{\xi} = (\xi_1, ..., \xi_n)$ which has a specific probability distribution. In practical applications, we have to restrict ourselves to the finite-term summation in which the highest order terms of the polynomials are set according to the accuracy requirement, namely

$$\alpha^*(\boldsymbol{x}, t, \boldsymbol{\xi}) \simeq \sum_{i=0}^{P} \alpha_i(\boldsymbol{x}, t)\Psi_i(\boldsymbol{\xi}) \tag{4.2}$$

Many choices are possible for basis functions depending on the type of the probability distribution selected for the varying input (37). Hermite polynomials form an orthogonal set of basis functions in terms of Gaussian distribution (38). The scope of this work stresses the sensitivity analysis rather than evaluation of effects of variations in input parameters. As such, we assume a Gaussian distribution for the input and use multi-dimensional Hermite polynomials as the basis for the expansion functions. Hermite polynomials in a space with random dimension $n$ are given by (38)

$$H_q(\xi_1, ..., \xi_n) = (-1)^p e^{\frac{1}{2}\boldsymbol{\xi}^T\boldsymbol{\xi}} \frac{\partial^p}{\partial(\xi_1)^{c_1} \dots \partial(\xi_n)^{c_n}} e^{-\frac{1}{2}\boldsymbol{\xi}^T\boldsymbol{\xi}} \tag{4.3}$$

where $\sum_{k=1}^{n} c_k = q$ and $p$ is the degree of the polynomial. In an $n$-dimensional space, the Hermite polynomials up to grade $p$ are $P + 1 = \frac{(n+p)!}{n!p!}$. Table 4.1 provides the $P + 1 =$

$\frac{(4+2)!}{4!2!} = 15$ four-dimensional (i.e., with four varying parameters) Hermite polynomials up to the second order, and their variances (38).

Table 4.1: The $P+1 = \frac{(4+2)!}{4!2!} = 15$ Hermite Polynomials of order 0,1,2 in a four-dimensional space.

| m | p | $\Psi_m$ | $< \Psi_m^2 >$ |
|---|---|---|---|
| 0 | p=0 | 1 | 1 |
| 1 | p=1 | $\xi_1$ | 1 |
| 2 | | $\xi_2$ | 1 |
| 3 | | $\xi_3$ | 1 |
| 4 | | $\xi_4$ | 1 |
| 5 | p=2 | ${\xi_1}^2 - 1$ | 2 |
| 6 | | $\xi_1\xi_2$ | 1 |
| 7 | | $\xi_1\xi_3$ | 1 |
| 8 | | $\xi_1\xi_4$ | 1 |
| 9 | | ${\xi_2}^2 - 1$ | 2 |
| 10 | | $\xi_2\xi_3$ | 1 |
| 11 | | $\xi_2\xi_4$ | 1 |
| 12 | | ${\xi_3}^2 - 1$ | 2 |
| 13 | | $\xi_3\xi_4$ | 1 |
| 14 | | ${\xi_4}^2 - 1$ | 2 |

As mentioned, the Hermite polynomials of random variables having a Gaussian distribution form a complete orthogonal set of basis functions. If $\beta$ and $\gamma$ are functions of the standard Gaussian distributed variable $\boldsymbol{\xi}$, then the inner product takes the form

$$< \beta(\boldsymbol{\xi}), \gamma(\boldsymbol{\xi}) >= \frac{1}{\sqrt{(2\pi)^n}} \int_{-\infty}^{\infty} \dots \int_{-\infty}^{\infty} \beta(\boldsymbol{\xi})\gamma(\boldsymbol{\xi}) e^{-(\frac{\boldsymbol{\xi}^T\boldsymbol{\xi}}{2})} d\boldsymbol{\xi} \tag{4.4}$$

with the density function of the $n$ variate standard Gaussian distribution as weighting function. Note that the inner product of two basis functions is nonzero only when a basis is

multiplied by itself, namely

$$< \Psi_i, \Psi_j >=< \Psi_i^2 > \delta_{ij}. \tag{4.5}$$

### 4.1.2 Computation of the expansion coefficients

In the framework of the rowing boat dynamics problem, we employ the polynomial chaos expansion to analyze how the output of the system $\alpha^*(\boldsymbol{x}, t, \boldsymbol{\xi})$ depends on a set of varying input parameters $\boldsymbol{\xi}$, which follow Gaussian distributions. The polynomial representation of the output provided by the PCE expansion (4.2) is in fact an algebraic function of the input parameters. The explicit dependency on $\boldsymbol{\xi}$ can be exploited to analyze the behavior of the system, and in particular to compute the sensitivity of the output to variations of the input parameters, which can be obtained by derivatives of Equation (4.2) with respect to each of the components of $\boldsymbol{\xi}$.

For a given number of varying parameters $n$, all the $P + 1$ Hermite polynomials up to order $p$, appearing in the PCE expansion are known. Hence, to obtain the polynomial representation of the output, we need to compute the coefficients $\alpha_i$ in the expansion. To do this we first write the inner product between the output $\alpha^*$ and the $i$-th Hermite polynomial namely

$$< \alpha^*(\boldsymbol{x}, t, \boldsymbol{\xi}), \Psi_i(\boldsymbol{\xi}) >= \frac{1}{\sqrt{(2\pi)^n}} \int_{-\infty}^{\infty} \dots \int_{-\infty}^{\infty} \alpha^*(\boldsymbol{x}, t, \boldsymbol{\xi}) \Psi_i(\boldsymbol{\xi}) e^{-(\frac{\boldsymbol{\xi}^T \boldsymbol{\xi}}{2})} d\boldsymbol{\xi}. \tag{4.6}$$

Substituting Equation (4.1) into Equation 4.6, and using the linearity of the inner scalar product, we write

$$\begin{aligned} < \alpha^*(\boldsymbol{x}, t, \boldsymbol{\xi}), \Psi_i(\boldsymbol{\xi}) > &= \sum_{k=0}^{\infty} \alpha_k(\boldsymbol{x}, t) < \Psi_k(\boldsymbol{\xi}), \Psi_i(\boldsymbol{\xi}) > & (4.7) \\ &= \sum_{k=0}^{\infty} \alpha_k(\boldsymbol{x}, t) < \Psi_k^2 > \delta_{ik} & (4.8) \\ &= \alpha_i(\boldsymbol{x}, t) < \Psi_i^2 >, & (4.9) \end{aligned}$$

where we also exploited the orthogonality of the Hermite polynomials. As such, the PCE coefficients can be computed by means of the following equation

$$\alpha_i(\boldsymbol{x},t) = \frac{<\alpha^*(\boldsymbol{x},t,\boldsymbol{\xi}),\Psi_i(\boldsymbol{\xi})>}{<\Psi_i^2(\boldsymbol{\xi})>}. \tag{4.10}$$

The computation of the integral in the numerator of the right hand side of Equation 4.10 presents some complications. First, it is an $n$-dimensional integral, on a domain which has an infinite measure (in fact, such a domain is the whole $\mathbb{R}^n$ space). In addition, the function $\alpha^*(\boldsymbol{x},t,\boldsymbol{\xi})$, in the most general case, is not an explicit algebraic function of the varying parameters $\boldsymbol{\xi}$. Its values can only be computed on a limited set of sampling points $\boldsymbol{\xi}^j, \quad j=1,\dots,N$ in the parameters space. Consequently, the inner product between $\alpha^*$ and the Hermite polynomials can only be computed by means of a suitable numerical scheme.

Two common approaches are used to obtain approximations of polynomial expansion coefficients. These are the *sampling based* and *quadrature methods*. In sampling based methods, the PCE coefficients $\alpha_i$ are determined by computing $\alpha^*(\boldsymbol{x},t,\boldsymbol{\xi}^j)\Psi_i(\boldsymbol{\xi}^j)$ for each realization and then averaging to estimate $<\alpha^*(\boldsymbol{x},t,\boldsymbol{\xi}),\Psi_i(\boldsymbol{\xi})>$. This procedure yields

$$\alpha_i(\boldsymbol{x},t) \approx \frac{\dfrac{1}{N}\displaystyle\sum_{j=1}^{N}\alpha^*(\boldsymbol{x},t,\boldsymbol{\xi}^j)\Psi_i(\boldsymbol{\xi}^j)}{<\Psi_i^2>}, \tag{4.11}$$

where $N$ is the number of realizations. The simplicity of their implementation makes the sampling based methods widely used. However the inaccuracy in the evaluation of the PCE coefficients makes them substantially inefficient for strongly nonlinear systems. From a mathematical standpoint, the sampling based method is inconsistent, and therefore may not necessarily converge, since

$$\lim_{N\to\infty}\frac{1}{N}\sum_{j=1}^{N}\alpha^*(\boldsymbol{x},t,\boldsymbol{\xi}^j)\Psi_i(\boldsymbol{\xi}^j) \neq \frac{1}{\sqrt{(2\pi)^n}}\int_{-\infty}^{\infty}\dots\int_{-\infty}^{\infty}\alpha^*(\boldsymbol{x},t,\boldsymbol{\xi})\Psi_i(\boldsymbol{\xi})e^{-(\frac{\boldsymbol{\xi}^T\boldsymbol{\xi}}{2})}d\boldsymbol{\xi}. \tag{4.12}$$

To improve the accuracy in the estimation of the inner product of the PCE coefficients, quadrature methods can be used to evaluate the integrals in Equation (4.10). In the one-dimensional case, the $Q$-points Gauss–Hermite quadrature rule (39) is used. This rule reads as

$$\frac{1}{\sqrt{2\pi}}\int_{-\infty}^{\infty} f(\xi)\Psi_i(\xi)e^{-(\frac{\xi^2}{2})}d\xi = \sum_{q=1}^{Q} f(\xi^q)w^q, \tag{4.13}$$

where the quadrature points $\xi^q$, $q = 1,\dots,Q$, are the zeros of the $Q$-th order mono-dimensional Hermite polynomials $H_Q$, and the quadrature weights are given by

$$w^q = \frac{2^{Q+1}Q!\sqrt{\pi}}{Q^2 H_{Q-1}(\xi^q)}. \tag{4.14}$$

In a more general $n-$dimensional space, the $N = Q^n$ quadrature points and weights are obtained by the $n-$dimensional tensor product of a set of $Q$ one-dimensional Gauss–Hermite quadrature points $\xi^{q_i}$ and weights $w^{q_i}$, namely

$$\frac{1}{\sqrt{(2\pi)^n}}\int_{-\infty}^{\infty}\dots\int_{-\infty}^{\infty} f(\boldsymbol{\xi})e^{-(\frac{\boldsymbol{\xi}^T\boldsymbol{\xi}}{2})}d\boldsymbol{\xi} = \sum_{q_1=1}^{Q}\sum_{q_2=1}^{Q}\dots\sum_{q_n=1}^{Q} f(\xi_1^{q_1},\xi_2^{q_2},\dots,\xi_n^{q_n})w^{q_1}w^{q_2}\dots w^{q_n}, \tag{4.15}$$

so that the approximated $i$-th PCE coefficient assumes the form

$$\alpha_i(\boldsymbol{x},t) \approx \frac{\sum_{q_1=1}^{Q}\sum_{q_2=1}^{Q}\dots\sum_{q_n=1}^{Q}\alpha^*(\boldsymbol{x},t,\xi_1^{q_1},\xi_2^{q_2}\dots,\xi_n^{q_n})\Psi_i(\xi_1^{q_1},\xi_2^{q_2},\dots,\xi_n^{q_n})w^{q_1}w^{q_2}\dots w^{q_n}}{<\Psi_i^2>}. \tag{4.16}$$

The quadrature based method is significantly more accurate than the sampling based method. In particular, when the number of sampling points is increased, the approximated value of the integral converges to the exact one. This results in very accurate approximations of the PCE coefficients. Nonetheless, the accuracy increment with respect to the sampling based method, is obtained at the price of a loss of flexibility, since the sampling points must now coincide with the set of $n$-dimensional quadrature points used. Thus, the number of realizations grows exponentially with the number of varying parameters considered, increasing significantly the computational cost.

An alternative way to obtain the coefficients of the polynomial expansion $\alpha(\boldsymbol{x},t)$ has been presented by Hosder et. al (36). Such method is based on the following matrix equation

$$\begin{Bmatrix} \alpha_0^* \\ \alpha_1^* \\ \vdots \\ \alpha_N^* \end{Bmatrix} = \begin{bmatrix} \psi_1(\boldsymbol{\xi}^0) & \psi_2(\boldsymbol{\xi}^0) & \cdots & \psi_P(\boldsymbol{\xi}^0) \\ \psi_1(\boldsymbol{\xi}^1) & \psi_2(\boldsymbol{\xi}^1) & \cdots & \psi_P(\boldsymbol{\xi}^1) \\ \vdots & \vdots & \ddots & \vdots \\ \psi_1(\boldsymbol{\xi}^N) & \psi_2(\boldsymbol{\xi}^N) & \cdots & \psi_P(\boldsymbol{\xi}^N) \end{bmatrix} \begin{Bmatrix} \alpha_0 \\ \alpha_1 \\ \vdots \\ \alpha_P \end{Bmatrix} \tag{4.17}$$

which represents the discretized form of equation (4.2). If the number of samples $N$ is selected so as to coincide with the number $P+1$ of polynomials in the expansion, the matrix in equation (4.17) is square, and can be inverted to obtain the expansion coefficients $\alpha_i$ from the outputs $\alpha_i^*$.

A remarkable advantage of this strategy, is that the number of samples needed to obtain the coefficients of the expansion is very small, making the application of these Polynomial Chaos Expansion techniques possible also for the most time consuming computations. On the other hand, as pointed out in (36), due to arbitrariness of the sampling vectors $\boldsymbol{\xi}^j$ chosen, both the system matrix and the PCE coefficients vector are not uniquely defined.

A possible way to overcome this problem —at the price of an increase of the number of samples needed— is to use a number of samples $N$ higher than the number of polynomials in the expansion $P+1$ and to solve system (4.17) by minimizing the errors in the least squares sense, namely

$$\overrightarrow{\alpha} = \left(L^T L\right)^{-1} L^T \overrightarrow{\alpha^*} \tag{4.18}$$

where $L$, $\overrightarrow{\alpha}$ and $\overrightarrow{\alpha^*}$ indicate respectively the —now rectangular— system matrix, the PCE coefficients vector and the output vector appearing in the system. This strategy leads to the so called *linear regression methods*, which —differently from the quadrature based methods— allow for more flexibility in the choice of the sampling points, and give the possibility of using efficient sampling strategies such as Latin hypercube sampling (LHS) (40; 41).

### 4.1.3 Implementation of polynomial chaos expansion

The performance of each of the above PCE approaches is determined by applying them to the light-weight single scull case considered above. This is done by introducing variations in the number of strokes per minute (or cadence) $r$, the maximum horizontal and vertical

Table 4.2: The mean and standard deviation values used for each of the four parameters considered in the PCE expansion.

| Parameter | $r = \mu_1 + \sigma_1\xi_1$ | $F_{X_{max}} = \mu_2 + \sigma_2\xi_2$ | $F_{Z_{max}} = \mu_3 + \sigma_3\xi_3$ | $m_r = \mu_4 + \sigma_4\xi_4$ |
|---|---|---|---|---|
| $\mu_i$ | 30 strokes/min | 1100 N | 100 N | 60 Kg |
| $\sigma_i$ | 1.5 strokes/min | 55 N | 5 N | 3 Kg |

forces per each stroke, $F_{X_{max}}$ and $F_{Z_{max}}$ respectively, and the mass of the rower $m_r$. To generate samples, these variations are assumed to follow Gaussian distributions. The mean and standard deviation for each of the above parameters are presented in Table 4.2. It should be noted that, based on the assumed ranges of input parameters, the stability of the boat is guaranteed.

To test all the different approaches proposed for the evaluation of polynomial expansion coefficients, 256 sampling points result from the four-dimensional tensor product of a 4 point Gauss-Hermite quadrature rule. This choice restricts the PCE expansions obtained to the third degree polynomials (a 4 point quadrature exactly computes the integrals of third degree polynomials (39)).

For each simulation, after the steady-state solution was reached, a set of 15 strokes was used to compute two performance metrics (output parameters). The first is the the mean surge velocity $V_X$, defined as

$$V_X = \frac{1}{T_2 - T_1} \int_{T_1}^{T_2} \dot{G}_X^h(t) dt. \tag{4.19}$$

The second is a performance index defined as the ratio of the kinetic energy associated with the surge motion (usable in terms of wining the race) to the energy associated with secondary motions. This energy ratio is defined as

$$\eta = \frac{V_X}{\sum_{i=1}^{3} \frac{1}{T_2 - T_1} \left( \int_{T_1}^{T_2} (\dot{G}_i^h(t) - V_i)^2 dt \right)^{1/2} + \sum_{i=1}^{3} \frac{1}{T_2 - T_1} \left( \int_{T_1}^{T_2} (\rho_i \omega_i(t))^2 dt \right)^{1/2}} \tag{4.20}$$

where $\rho_i$ are the values of the boat hull radii of gyration.

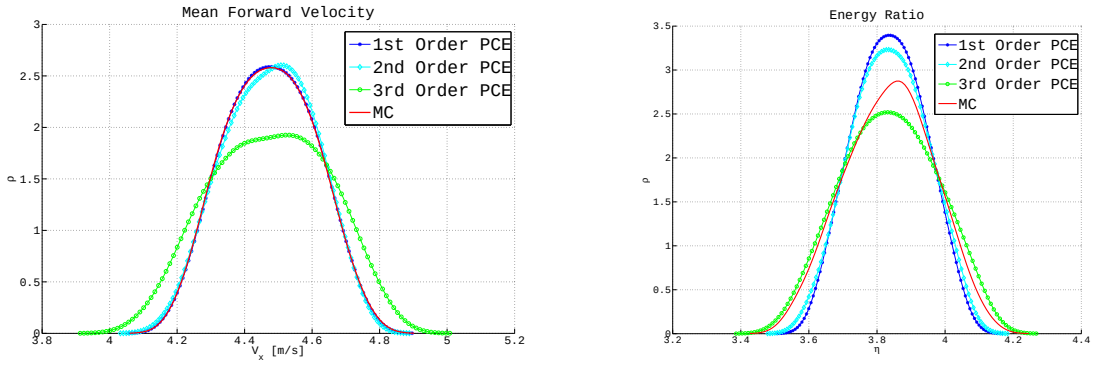


a) b)

Figure 4.2: Comparison of the probability distribution functions of mean velocity —a)— and energy ratio —b)— obtained with Monte Carlo simulations and PCE expansions of different orders by means of the sampling based method. The colors indicate: — 1st Order PCE, — 2nd Order PCE, — 3rd Order PCE, — Monte Carlo.

Fig.4.2 shows a comparison between the probability distribution of the output parameters computed from the 256 realizations based on original simulations (deterministic problem) and those determined from first, second and third order non-intrusive PCE performed by means of the sampling based method. It is clear from Fig.4.2 (a), which depicts the probability distribution function for the mean forward velocity, that the relation between the input parameters and $V_X$ is close to be linear. The sampling based method provides a good approximation of the first order expansion terms. Yet, its accuracy drastically drops when higher order terms are taken into account. On the other hand, Fig.4.2 (b) shows that the sampling based method fails to reproduce the strongly nonlinear relation between the input parameters and the energy ratio $\eta$. These conclusions are based on the observations that, in these figures, the probability distribution function for the velocity is nearly Gaussian, while that of the energy ratio is non Gaussian. As such, the sampling based method seems fairly accurate in the approximation of the zeroth and first coefficients of the first order PCE polynomials, but should not be used if a nonlinear input-output relationship is expected.

To improve the estimation of the energy ratio $\eta$, the quadrature based method is used

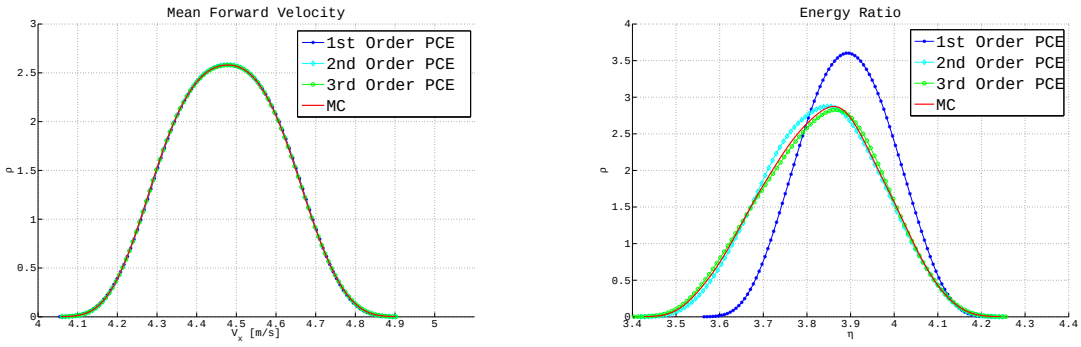


a) b)

Figure 4.3: Comparison of the probability distribution functions of mean velocity —a)— and energy ratio —b)— obtained with Monte Carlo simulations and PCE expansions of different orders by means of the quadrature based method. The colors indicate: — 1st Order PCE, — 2nd Order PCE, — 3rd Order PCE, — Monte Carlo.

to evaluate the PCE coefficients. Fig. 4.3 shows a comparison of probability distribution functions obtained with Monte Carlo simulations and with quadrature based PCE expansion. The results show that the quadrature based method improves the accuracy in the estimation of the integrals needed for the PCE projection. Clearly, the quadrature based method reproduces correctly the linear relationship between input parameters and mean forward velocity. Furthermore, it also yields good estimates of the (small) coefficients of the higher-order terms in the expansion. This method also yields good estimates of the PCE coefficients for the nonlinear energy ratio (see Fig. 4.3 (b)). For these estimates, the addition of the higher order terms is mandatory for a good approximation of the output. Finally, Fig. 4.4 shows analogous results obtained when the linear regression method is implemented. For this method, the relationship between input parameters and $V_X$ (Fig. 4.4 (a)) is accurately reproduced for first, second and third order expansions, while the approximation of $\eta$ requires the computation of second and third order terms.

To provide a quantitative evaluation of the effectiveness of methods used above, the $||\cdot||_\infty$ and $||\cdot||_2$ norms of the relative errors of the each expansion are computed (see Table 4.3) and depicted in Fig. 4.5. The plots clearly show that the sampling method is not suitable to

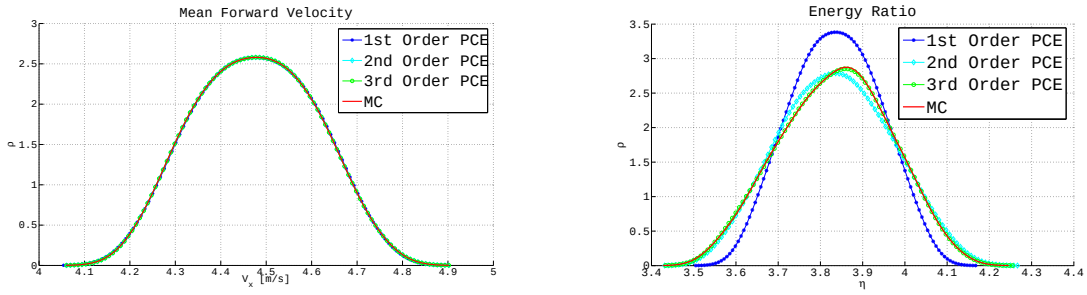


a) b)

Figure 4.4: Comparison of the probability distribution functions of mean velocity —a)— and energy ratio —b)— obtained with Monte Carlo simulations and PCE expansions of different orders by means of the linear regression method. The colors indicate: — 1st Order PCE, — 2nd Order PCE, — 3rd Order PCE, — Monte Carlo.

increase the order of the polynomial expansion, because the increased computational effort does not improve the approximation accuracy. Furthermore, although both the quadrature-based and linear regression methods yield comparable accuracies, the errors show that, in all considered cases, the linear regression method is more accurate. This is expected in the case of the $||\cdot||_2$ norm of the error, as the solution provided by the least squares method minimizes precisely this of error norm. It should be noted though, that in all the cases considered also the maximum error obtained with the linear regression was the lowest.

Table 4.3: $||\cdot||_\infty$ and $||\cdot||_2$ norm of the relative errors for each of the methods used to obtain the PCE expansion in the case of the energy ratio $\eta$.

| Method | Sampling based | | | Quadrature based | | | Linear regression | | |
|---|---|---|---|---|---|---|---|---|---|
| Order | 1st | 2nd | 3rd | 1st | 2nd | 3rd | 1st | 2nd | 3rd |
| $\|\|\boldsymbol{e}\|\|_\infty$ | $3.3 \cdot 10^{-2}$ | $2.6 \cdot 10^{-2}$ | $3.7 \cdot 10^{-2}$ | $5.5 \cdot 10^{-2}$ | $1.7 \cdot 10^{-2}$ | $9.4 \cdot 10^{-3}$ | $3.3 \cdot 10^{-2}$ | $1.0 \cdot 10^{-2}$ | $5.9 \cdot 10^{-3}$ |
| $\|\|\boldsymbol{e}\|\|_2$ | $3.9 \cdot 10^{-3}$ | $1.6 \cdot 10^{-3}$ | $2.0 \cdot 10^{-3}$ | $6.4 \cdot 10^{-4}$ | $2.5 \cdot 10^{-5}$ | $9.2 \cdot 10^{-6}$ | $3.8 \cdot 10^{-4}$ | $1.2 \cdot 10^{-5}$ | $3.5 \cdot 10^{-6}$ |

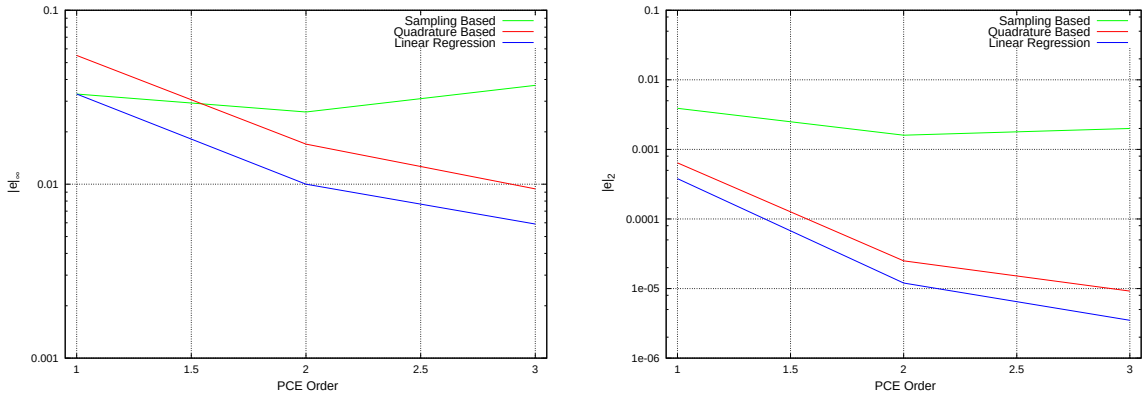


a) b)

Figure 4.5: $||\cdot||_\infty$ (plot a)) and $||\cdot||_2$ (plot b)) norm of the relative errors as a function of the PCE truncation order, for each of the methods used to obtain the PCE expansion in the case of the energy ratio $\eta$. The colors indicate: — Sampling based Method, — Quadrature Based Method, — Linear Regression Method.

## 4.2 Computation of sensitivities to input parameters

To illustrate how sensitivities are obtained from PCE expansion coefficients, we show an example of the single scull test case. As previously pointed out, for this boat configuration the first order PCE polynomials yield a good approximation of the functional dependency between the mean forward velocity and the input parameters. Thus, the first order terms in Table 4.2, namely

$$V_X(r, F_{X_{max}}, F_{Z_{max}}, m_r) = \alpha_1 + \alpha_2\xi_1 + \alpha_3\xi_2 + \alpha_4\xi_3 + \alpha_5\xi_4 \quad (4.21)$$

$$= \alpha_1 + \alpha_2\left(\frac{r-\mu_1}{\sigma_1}\right) + \alpha_3\left(\frac{F_{X_{max}}-\mu_2}{\sigma_2}\right) \quad (4.22)$$

$$+ \alpha_4\left(\frac{F_{Z_{max}}r-\mu_3}{\sigma_3}\right) + \alpha_5\left(\frac{m_r-\mu_4}{\sigma_4}\right) \quad (4.23)$$

provide a fairly accurate approximation of the effects of variations in input parameters on the boat surge velocity. The performance sensitivities with respect to changes in each input parameter are then obtained by computing the derivatives of this linear function with respect to $r, F_{X_{max}}, F_{Z_{max}}$ and $m_r$, namely

$$\frac{\partial V_X}{\partial r} = \frac{\alpha_2}{\sigma_1}, \qquad \frac{\partial V_X}{\partial F_{X_{max}}} = \frac{\alpha_3}{\sigma_2}, \qquad \frac{\partial V_X}{\partial F_{Z_{max}}} = \frac{\alpha_4}{\sigma_3}, \qquad \frac{\partial V_X}{\partial m_r} = \frac{\alpha_5}{\sigma_4}.$$

It is important to note here that, due to the linear approximation used, the sensitivity values here are constants; at least in the region of the random parameter space in which the expansion is an accurate approximation of the output $\alpha^*$. In a more general case, the relationship between input and output parameters may not be linear. For these cases, the local sensitivity of the output $\alpha^*$ to changes of the $i$-th input parameter $\xi_i$ would be computed by means of

$$\frac{\partial \alpha^*}{\partial \xi_i}(\boldsymbol{x}, t, \boldsymbol{\xi}) = \sum_{p=0}^{P} \alpha_p(\boldsymbol{x}, t) \frac{\partial \Psi_p(\boldsymbol{\xi})}{\partial \xi_i}. \tag{4.24}$$

The sensitivity analysis as detailed above, is applied in the following sections to study the performance of different kinds of Olympic boat classes, with the objectives of evaluating how input parameters affect the boat response and determining how they can be changed to enhance the boat's performance. The first boat class analyzed here is that of a light single scull with a female rower. The four varying input parameters include the number of strokes per minute, $r$, the maximum horizontal and vertical forces per each stroke, $F_{X_{max}}$ and $F_{Z_{max}}$ respectively, and the mass of the rower, $m_r$. The second boat class considered is that of a quad scull pushed by four male rowers. This test case is used as a benchmark to evaluate the performances of all the fluid dynamic models discussed in Chapter 3. The symmetrical rowing configuration is chosen so as to perform the sensitivity analysis also with the RANS model, which could be made unstable by the mesh deformation due to excessive sway motions. For the same reason, the number of varying parameters is, in this test case, reduced to two (*i.e.*: the first rower maximum horizontal force, $F_{X_{max}}$, and weight, $m_r$), limiting the number of realizations needed for the analysis. The third and final boat class considered is a male coxless four. Being a sweep boat, it undergoes full three-dimensional secondary motions, which can be minimized if the rowers forces are balanced. So, in order to understand the effects of slight variations in the rower forces, and which rower's position is the most critical for the overall crew performance, variations are introduced in the values of the rowers maximum horizontal

forces $F_{X_{max}\ 1}$, $F_{X_{max}\ 2}$, $F_{X_{max}\ 3}$, $F_{X_{max}\ 4}$, in the rowers masses $m_{r1}$, $m_{r2}$, $m_{r3}$, $m_{r4}$, and in the cadence $r$.

## 4.3 Sensitivity analysis for different boat classes

### 4.3.1 Female light-weight single scull

The computed sensitivity values for the mean velocity to variations in different parameters for the female light-weight single scull are presented in Table 4.4. In this case, given the fact that the relationship between input and output parameters is particularly close to a linear one (as illustrated in section 4.1.3), the sensitivity values are constant. The results indicate that increasing both the maximum horizontal oarlock force and the rowing cadence results in an increase of the forward mean velocity. Furthermore, as expected, increasing the weight of the rower leads to a reduction in the forward speed. The maximum vertical oarlock force on the other hand, does not seem to have significant effects on the boat performances.

Table 4.4: Sensitivity values of mean forward speed to variations in cadence $r$, maximum horizontal and vertical oarlock force, $F_{X_{max}}$ and $F_{Z_{max}}$, and mass of the rower, $m_r$.

| Parameter | $r$ | $F_{X_{max}}$ | $F_{Z_{max}}$ | $m_r$ |
|---|---|---|---|---|
| Sensitivity | $0.0438 \frac{\mathrm{m}}{\mathrm{s}} / (\frac{\mathrm{strokes}}{\mathrm{min}})$ | $0.0028\ \frac{\mathrm{m}}{\mathrm{s}}/\mathrm{N}$ | $0.0001\ \frac{\mathrm{m}}{\mathrm{s}}/\mathrm{N}$ | $-0.0230\ \frac{\mathrm{m}}{\mathrm{s}}/\mathrm{Kg}$ |

The ratios between the sensitivity values also provide important information, which can guide rowing athletes and coaches in their decisions concerning rowing techniques and training strategies. For instance, if the rowing cadence is reduced by 1 stroke/min, the rower will have to increase the maximum horizontal oarlock force by approximatively 15 N in order to obtain the same surge velocity. Likewise, if the mass of the rower is increased by 1 Kg, she will need to be able to generate a maximum force which is roughly 8 N higher in order to compensate for the increase in weight and keep the same surge velocity.

Since the relation between the energy ratio and input parameters is nonlinear, the sensitivity values for $\eta$ are not constant. Clearly, they depend on the point of the parameters

space in which the computation is performed. Fig. 4.6 displays contours of $\eta$ —Fig. 4.6 (a)— and of its sensitivities to the rowing cadence $r$ —Fig. 4.6 (b)— and to the maximum horizontal oarlock force $F_{Xmax}$ —Fig. 4.6 (c)— obtained by keeping the maximum vertical oarlock force and the rower mass at the constant values $F_{Zmax} = 100$ N and $m_r = 60$ Kg, respectively.

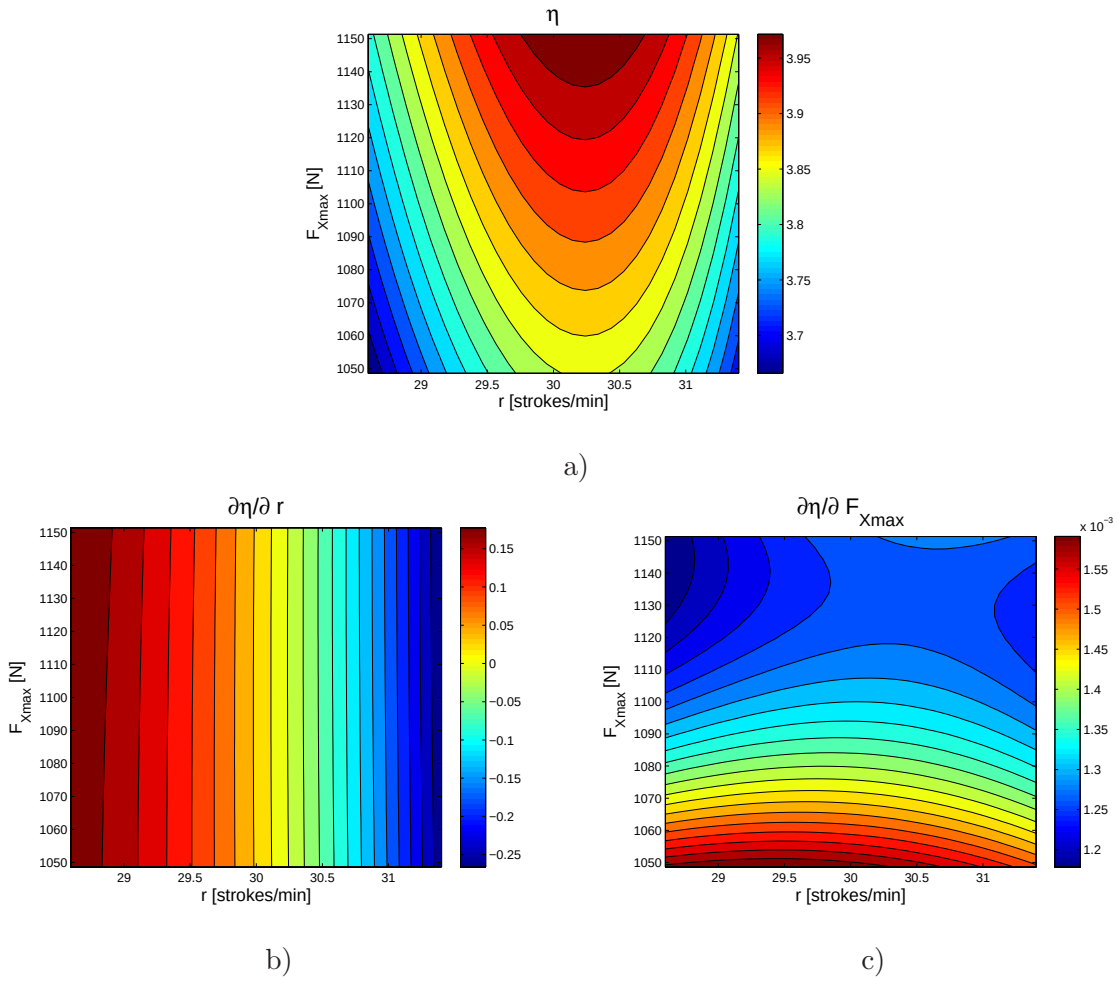


Figure 4.6: Plot a) depicts contours of the PCE expansion of the energy ratio for fixed weight and vertical oar force, and variable horizontal oar force and cadence. For the same range of values, the bottom plots represent the sensitivity values with respect to the cadence —b)— and the horizontal oar force —c)

As expected, the contour plot of the energy ratio in Fig. 4.6 (a) suggests that a higher

value of $F_{Xmax}$ leads to higher values of energy ratio, as increasing the horizontal force is the principal way to introduce energy in the surge motion. On the other hand, the plot shows that for a given force, there is a rowing cadence value that maximizes $\eta$. A look at the $\partial\eta/\partial r$ contour in Fig. 4.6 (b) confirms that the cadence sensitivity sign changes along an approximatively vertical line near $\overline{r} = 30.2\ \frac{\text{strokes}}{\text{min}}$, which is remarkably close to the cadence $30\ \frac{\text{strokes}}{\text{min}}$ of rowers in race conditions. Fig. 4.6 (c) shows instead that, for each rowing cadence considered, an increase in the maximum horizontal force $F_{Xmax}$, results in better performance. From the sensitivity values presented in Fig. 4.6 it is possible to compute that at the point ($r = 30\ \frac{\text{strokes}}{\text{min}}$, $F_{Xmax} = 1100$ N, $F_{Zmax} = 100$ N, $m_r = 60$ Kg) of the parameter space, a cadence increase of $1\ \frac{\text{stroke}}{\text{min}}$ is equivalent to an increase in the horizontal oarlock force of about 31 N. On the other hand, a mass increase of 1 Kg has to be compensated by a force increase of approximately 28 N. Thus, the rowing cadence and the rower weight impact the energy ratio more than the surge velocity.

### 4.3.2 Male quad scull: a benchmark for fluid dynamic models

A second sensitivity study is carried out for the test case of a quad scull. The aim of such study is to understand how the computed sensitivities to input parameters of the rowing boat dynamical system are affected by the fluid dynamic model chosen for the closure of Problem (2.1). Thus, a sensitivity analysis will be performed with each of the different fluid dynamic models discussed in Chapter 3.

The quad scull hull used for the numerical tests is approximatively 12 m long and has a mass of 50 kg. It is pushed by four rowers with a mass of 80 kg each, rowing at the pace of 36 strokes per minute. The maximum horizontal and vertical components of the oarlock force set at 1200 N and 200 N respectively. It is worth noting that in the symmetrical boat configuration of a scull, the rowers hold one oar per hand, and their force is applied symmetrically to the two oar handles. This setup has been preferred as a benchmark for the computation of the sensitivities to input parameters variations, as the presence of the sway motion in the non symmetrical test case would lead to an excessive mesh deformation in the high fidelity RANS model simulations, which results in unstable simulations. Symmetrical configurations yield no significant sway, and allow the use of the RANS model for the sensitivity analysis.

To perform the sensitivity analysis, we introduced variations in two input parameters, which are the weight and maximum oarlock force of the first rower (the one closest to the bow of the boat). The mean and standard deviation values for each to these variable parameters are reported in Table 4.5.

Table 4.5: Mean and standard deviations of varying parameters for the quad scull case. Only two parameters are varied because of limited time for computations using the RANS fluid dynamic model.

| Parameter | $F_{X_{max\ 1}} = \mu_1 + \sigma_1\xi_1$ | $m_{r\ 1} = \mu_2 + \sigma_2\xi_2$ |
|---|---|---|
| $\mu_i$ | 1200 N | 80 Kg |
| $\sigma_i$ | 60 N | 4 Kg |

The low number of varying parameters has been once again chosen so as to be able to perform the sensitivity analysis also with the high fidelity model. In fact, as previously pointed out, each RANS simulation takes approximatively 60 hours and the total numbers of simulations has to be limited. Using the Polynomial Chaos Expansion up to the second order results in a minimum number of realizations

$$n_{min} = \frac{(2+2)!}{2!+2!} = 6.$$

As the linear regression method is used to obtain the PCE coefficients, we used $n_{samples} = 9$ for each sensitivity analysis, distributing the sampling points in the parameters space by using the Latin Hypercube sampling strategy. Thus, nine different force and weight configurations were created for the first rower in the scull. For each configuration, a 15 s simulation is started, having identical initial conditions. The last 5 seconds of each simulations (which at the pace of 36 strokes per minute correspond to exactly 3 strokes) were used to compute the output parameters considered, which as in the previous cases are the mean surge velocity, $V_X$, and the energy ratio, $\eta$, as defined in Equation (4.20).

The sensitivities of the mean surge velocity to changes in the first rower force and weight are presented in Table 4.6. The results obtained with all the fluid dynamic models considered are similar. In particular, the sensitivities to changes in the rower's weight assume practically

the same values, whether computed with the high fidelity or with the reduced-order models. As for the sensitivity to variations in the maximum horizontal oarlock force, the value obtained with the RANS model is less then 10% different from each of the reduced-order model predictions. Considering that the 9 simulations needed for the sensitivity analysis take 40 mins when computed using the reduced-order models, and over 20 days when computed by means of the high fidelity model, the results of the reduced-order model are quite satisfactory.

Table 4.6: Sensitivities of the surge mean velocity $V_X$ to variations in the first rower's maximum horizontal oarlock force $F_{X_{max\ 1}}$ and weight $m_{r\ 1}$.

| Parameter | RANS | 3D Potential | PDStrip | PDStrip Conv. |
|---|---|---|---|---|
| $F_{X_{max\ 1}}$ | $8.27 \cdot 10^{-4}\ \frac{\mathrm{m}}{\mathrm{s}}/\mathrm{N}$ | $9.09 \cdot 10^{-4}\ \frac{\mathrm{m}}{\mathrm{s}}/\mathrm{N}$ | $9.35 \cdot 10^{-4}\ \frac{\mathrm{m}}{\mathrm{s}}/\mathrm{N}$ | $9.26 \cdot 10^{-4}\ \frac{\mathrm{m}}{\mathrm{s}}/\mathrm{N}$ |
| $m_{r\ 1}$ | $-0.0076\ \frac{\mathrm{m}}{\mathrm{s}}/\mathrm{kg}$ | $-0.0076\ \frac{\mathrm{m}}{\mathrm{s}}/\mathrm{kg}$ | $-0.0077\ \frac{\mathrm{m}}{\mathrm{s}}/\mathrm{kg}$ | $-0.0076\ \frac{\mathrm{m}}{\mathrm{s}}/\mathrm{kg}$ |

Sensitivities of the energy ratio with respect to variations of the first rower's weight and horizontal oarlock force are presented in Table 4.7. The values of the sensitivity to horizontal force obtained with the different fluid dynamic models are also in close agreement, as differences in the values obtained with the reduced order model and with high fidelity model are less then 6%. The results for the sensitivity of $\eta$ to variations in the weight of the first rower are not as satisfactory, as the difference between the values computed with the RANS simulations and the ones computed with the reduced order models can be as high as 39%. This is probably due to the fact that a weight increment increases the inertia of the system, and consequently the tendency of the boat to move away from the symmetry plane as a result of numerical errors or gyroscopic effects. In presence of a significant yaw angle, the reduced order models predictions —which are not accounting for the lateral lift force— become less accurate in predicting the sway motion. This does not affect the sensitivities of the mean surge velocity as the yaw angles remain small, but it affects sensitivities of the energy coefficient , which is accounting for the motions in all the six degrees of freedom.

More generally, among the results obtained with the reduced order models, the closest to the corresponding RANS values are the 3D potential results, which account for the longitu-

Table 4.7: The sensitivities of the surge mean velocity $\eta$ to variations in the first rower's maximum horizontal oarlock force $F_{X_{max\ 1}}$ and weight $m_{r\ 1}$.

| Parameter | RANS | 3D Potential | PDStrip | PDStrip Conv. |
|---|---|---|---|---|
| $F_{X_{max\ 1}}$ | $9.14 \cdot 10^{-4}$ 1/N | $9.01 \cdot 10^{-4}$ 1/N | $9.93 \cdot 10^{-4}$ 1/N | $9.70 \cdot 10^{-4}$ 1/N |
| $m_{r\ 1}$ | $-0.0152$ 1/kg | $-0.0109$ 1/kg | $-0.0092$ 1/kg | $-0.0100$ 1/kg |

dinal components of the damping and added mass matrices, disregarded in the strip theory models. Moreover, it is noted that when the convolution term in Equation (3.34) is used to account for the frequency dependency of the damping and added mass matrices of the boat, the predictions of the strip theory model slightly improve. These considerations suggest that the reduced order model can be improved by computing the convolution term also with radiative coefficients from the 3D potential model. This has not been possible so far, due to the presence of high frequency and high amplitude oscillations in the damping and added mass frequency dependence, and appears to be one of the most important improvements to be implemented in the future.

As with the single scull case previously analyzed, we can use ratios of the sensitivity values in Table 4.6 and Table 4.7 to quantify the trade off between the performance increments due to force and weight variations. When the mean surge velocity is the performance parameter considered, a body mass increase of 1 kg has to be compensated by a force increment of 9 N. On the other hand, if $\eta$ is considered, a 1 kg mass reduction is equivalent to 17 N force increase. These values are slightly higher than the ones obtained in the case of a single single scull, which suggests that a weight and force increase is not as convenient for a crew member of a four male scull, as it would be for a female athlete on a single scull.

### 4.3.3 Male coxless four

For this male four sweep boat, nine parameters were varied. These include each of the rowers maximum horizontal force and weight, and the rowing cadence. Because of the high number of parameters considered, the linear regression method is used to compute the polynomial chaos expansion coefficients. The sampling points in the input parameter space were chosen

Table 4.8: The mean and standard deviation values used for the parameters considered in the PCE expansion for the case of a four sweep boat

| Parameter | $F_{X_{max\ i}} = \mu_i + \sigma_i \xi_i$, i=1,...,4 | $m_{r\ i} = \mu_{i+4} + \sigma_{i+4} \xi_{i+4}$, i=1,...,4 | $r = \mu_9 + \sigma_9 \xi_9$ |
|---|---|---|---|
| $\mu_i$ | 1200 N | 80 Kg | 32.5 strokes/min |
| $\sigma_i$ | 60 N | 4 Kg | 1.625 strokes/min |

according to the Latin hypercube sampling strategy, imposing the mean and standard deviation values reported in Table 4.8. Considering nine parameters, the minimum number of samples needed to obtain a fourth order expansion is

$$n_{min} = \frac{(9+6)!}{9!+6!} = 5005.$$

The number of samples was then set to $n_{samples} = 10000$.

The probability distribution functions of the mean surge velocity and of the energy ratio $\eta$ are presented respectively in the a) and b) plots of Fig. 4.7. Looking at the plots, it is possible to appreciate how, for the mean surge velocity, the polynomial reconstruction provides a very good approximation of the output, in particular when higher order terms are included. On the other hand, the plot of the energy ratio, shows that, even if the expansions get more accurate with the addition of higher order terms, the fourth order expansion PDF curve is still not overlapped to the curve obtained with Monte Carlo simulations.

The values of the sensitivity computed at the origin of the parameter space $\boldsymbol{\xi} = \{0\}$ (the sensitivities cannot be considered constant if, as in the case at hand, the relationship between input and output parameter is not linear) are reported in Table 4.9. At this specific point, the mean velocity sensitivities with respect to the maximum horizontal forces variations of all the athletes have similar values, with the rower in the front having a slightly higher sensitivity than the others. Also, when the weight is considered, the velocity sensitivities show small differences between the different rowers. It is interesting to note, however, that with this boat, to compensate a mass increase of 1 kg, each rower has to be able to increase his maximum horizontal force of about 8 N, a value that is similar to the one found analyzing the female single scull. In addition, the effect of an increase in the pace of one stroke per

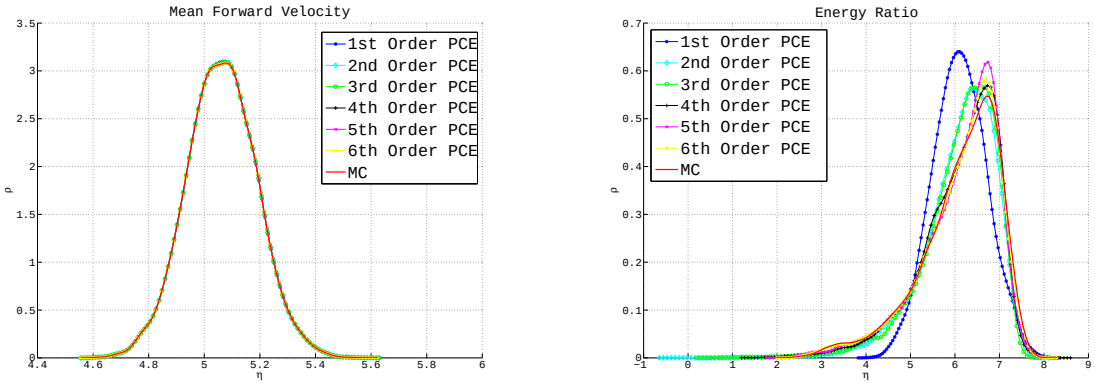


a) b)

Figure 4.7: Comparison of the probability distribution functions of mean velocity —a)— and energy ratio —b)— obtained with Monte Carlo simulations and PCE expansions of different orders for the four boat. The colors indicate: — 1st Order PCE, — 2nd Order PCE, — 3rd Order PCE, — 4st Order PCE, — 5nd Order PCE, — 6rd Order PCE, — Monte Carlo.

minute on the velocity, is equivalent to an increase of approximatively 40 N in the maximum force. The higher value with respect to the single case, seems to indicate that brute force is less important in this boat class, than it is for the single scull case.

The sensitivities of the energy ratio to variations in input parameters have more complex characteristics. From the values obtained, it appears that one possible way to increase $\eta$ would be to reduce the rowing pace $r$, as the value of $\partial\eta/\partial r$ is negative. An energy ratio increase, would be also obtained by decreasing the weight of the first rower. In fact, the sensitivity to the first rower weight is approximatively twice that of the second and third rower, and four times that of the fourth rower. Thus, it is reasonable to assume, from an energetic standpoint, that it is better to place the heaviest rowers behind the boat barycenter, at seats three or four, while lighter rowers should be kept closer to the boat bow. The sensitivities to variations of the rowers maximum oarlock forces seem to confirm that the first three rowers have a higher influence on the boat energetic efficiency than the fourth one. The values presented in the table show in fact that the fourth maximum oarlock force sensitivity value is five to six time lower than the corresponding values of each of the first three rowers.

Table 4.9: Sensitivity values obtained for each of the nine parameters considered in the PCE expansion, at the point $\boldsymbol{\xi} = \{0\}$ of the parameters space

| Input Param. | $V_X$ sensit. | $\eta$ sensit. |
|---|---|---|
| $F_{X_{max\ 1}}$ | $8.38 \cdot 10^{-4}\ \frac{\mathrm{m}}{\mathrm{s}}/\mathrm{N}$ | 0.0014 1/N |
| $F_{Z_{max\ 2}}$ | $8.41 \cdot 10^{-4}\ \frac{\mathrm{m}}{\mathrm{s}}/\mathrm{N}$ | 0.002 1/N |
| $F_{X_{max\ 3}}$ | $8.34 \cdot 10^{-4}\ \frac{\mathrm{m}}{\mathrm{s}}/\mathrm{N}$ | 0.0015 1/N |
| $F_{Z_{max\ 4}}$ | $8.37 \cdot 10^{-4}\ \frac{\mathrm{m}}{\mathrm{s}}/\mathrm{N}$ | 0.0003 1/N |
| $m_{r\ 1}$ | $-0.0066\ \frac{\mathrm{m}}{\mathrm{s}}/\mathrm{Kg}$ | $-0.0287$ 1/Kg |
| $m_{r\ 2}$ | $-0.0064\ \frac{\mathrm{m}}{\mathrm{s}}/\mathrm{Kg}$ | $-0.0176$ 1/Kg |
| $m_{r\ 3}$ | $-0.0065\ \frac{\mathrm{m}}{\mathrm{s}}/\mathrm{Kg}$ | $-0.0142$ 1/Kg |
| $m_{r\ 4}$ | $-0.0063\ \frac{\mathrm{m}}{\mathrm{s}}/\mathrm{Kg}$ | $-0.0086$ 1/Kg |
| $r$ | $0.0343\ \frac{\mathrm{m}}{\mathrm{s}}/(\frac{\mathrm{strokes}}{\mathrm{min}})$ | $-0.1589\ 1/(\frac{\mathrm{strokes}}{\mathrm{min}})$ |

## 4.4 Summary

In the first part of the chapter, polynomial chaos expansions (PCE) are implemented to approximate the solution of the dynamical system formulated in Chapter 2. Three different methods have been used to obtain the PCE coefficients from the outputs generated by the system at each sampling point. Their performance on the test case of a female light-weight single scull showed that

- In **the sampling based method** the computation of the PCE coefficients is based on the average of the system output values at the sampling points. This method has a very straightforward implementation, but being based on an inconsistent numerical scheme, the integral expressing the inner product of the Hermit polynomials and the output function does not converge with increasing the number of samples. Consequently, the results obtained with this method show that it only provides accurate approximations of the zeroth and first order polynomial coefficients. Thus, its use is convenient only in systems in which a linear relationship between input and output parameters is expected.

- In **the quadrature based method** as implemented here, the sampling points used are Gauss–Hermite quadrature points. The integral expressing the inner product of

the Hermit polynomials and the output function is hence approximated by means of a Gauss–Hermite quadrature rule. The results show that this method significantly improves the accuracy, with respect to the sampling based method, and is able to provide reliable approximations higher order PCE coefficients. On the other hand, since the number of quadrature points grows exponentially with the dimension of the space spanned by the integral (*i.e.*, the number of varying input parameters), this method suffers of the so called *curse of dimensionality*, which makes its use not convenient in problems with a high number of varying parameters.

- In **the linear regression method** the PCE coefficients are obtained by solving the linear system representing the discretized form of the Karhunen–Loève expansion. If the number of samples is equal to the number of polynomials of the expansion, the matrix of the system is square and can be inverted to solve the system. As the samples location is arbitrary, this might lead to an arbitrariness in the PCE coefficients. To limit the problem, in our implementation the number of sample points generated is higher than the number of polynomials of the expansion, and the system is solved in the least squares sense. The results obtained show that this method provides a very good approximation of the PCE coefficients, even of high order. In addition, the number of samples needed for the expansion is not growing exponentially with the number of varying input parameters. For this reason, this method is used for the sensitivity analysis presented in the next chapter.

The sensitivity analysis based on polynomial chaos expansions, is then applied to the solution of dynamical system formulated in Chapter 2. From a mathematical standpoint, the polynomial chaos expansion is an algebraic relationship between the varying input parameters and the output. Taking the derivatives of such a relationship with respect to the varying input parameters, yields the sensitivities of the approximated output parameters to variations of each of the inputs. Clearly, the accuracy of the computed sensitivities depends on the accuracy of the PCE expansion, hence on the polynomial degree at which the expansion series is truncated. In the sensitivity analysis discussed, the output parameters considered are the boat mean surge velocity and energy ratio, as defined in Equations (4.19) and (4.20)

respectively. The varying input parameters in the analysis are related to the rowers oarlock and inertial forces, and depend on the specific test case analyzed. The three test cases considered are a light-weight female single scull, a male quad scull a coxless four.

# Chapter 5

# Conclusions

In this work, a multidisciplinary approach for the modeling and analysis of the performance of Olympic rowing boats is presented. The goal is to establish methodologies and tools that would determine the effects of variations in applied forces and rowers motions and weights on mean surge speed and oscillatory boat motions. The coupling between the rowers motions with the hull and water forces is modeled with a system of equations. This model can consider different rowing techniques. It can account for different boat geometries, hull shapes and rowers distributions, heights and weights. The output of the model consists of the full three-dimensional motions of the boat.

One of the important inputs to the model is the water forces. These forces are computed using several fluid dynamic models that have different levels of accuracy and computational cost. The viscous and turbulent flow of both water and air past a rowing boat is simulated to a satisfactory level of detail by solving the Reynolds Averaged Navier–Stokes equations, complemented by a Volume of Fluid method, to compute the evolution of the water free surface. This model is considered as the high fidelity fluid dynamic model that helps tuning and validating low fidelity models which can provide quicker but sufficiently accurate answers needed for the design and training processes. In a second model, a linearized 3D potential approach, that is based on the decomposition of the fluid dynamic forces into the contributions due to mean and secondary motions, is used for the prediction of water forces. It is found that due to the elongated shape of the boat, the use of Sommerfeld truncation boundary

condition does not yield the correct frequency dependence of the radiative coefficients. Thus, the radiative forces are not computed in the time-domain problem by means of a convolution integral, accounting for flow memory effects, but were computed assuming constant damping and added mass matrices. Nonetheless, the results of this fluid dynamic model when coupled with the rowing boat dynamical system are encouraging. With simulations that last for few minutes, this model is able to predict values of the most important performance parameters which are in very close agreement with the RANS model.

To obtain a smoother frequency dependence of the damping and added mass matrices, the radiative problem is also solved by means of the strip theory approximation. The results are very close to the 3D potential model. They also show that accounting for memory effects significantly improves the agreement between the strip theory and the RANS predictions. Further improvements could be obtained by introducing corrections to account for longitudinal radiative forces, which are completely neglected in the strip theory.

The coupled dynamical system and the multi-fidelity fluid models were then used to perform a sensitivity analysis of boat motions to variations in rowers weights, exerted forces and cadence of motion. The sensitivity analysis is based on the polynomial chaos expansion, which is used to approximate the output parameters of the rowing boat dynamical system as a linear combination of Hermite polynomial basis functions, depending on the selected input parameters, which vary following a Gaussian distribution. The coefficients of each random basis in the polynomial chaos expansion are computed using a non-intrusive strategy. Three different methods have been used to obtain the these coefficients from the outputs generated by the system at each sampling point. Their performance on the test case of a female light-weight single scull shows that the sampling based method has a very straightforward implementation, but, being based on an inconsistent numerical scheme, may not necessarily converge. Its use is convenient only in systems in which a linear relationship between input and output parameters is expected. The quadrature based method significantly improves the accuracy, in comparison to the sampling based method, and is able to provide reliable approximations higher order PCE coefficients. On the other hand, since the number of quadrature points grows exponentially with number of varying input parameters, the use of this method is not convenient in problems with a high number of varying parameters. The

linear regression method, in which the PCE coefficients are obtained by solving —in the least square sense— a suitable linear system, provides a very good approximation of the PCE coefficients, even of those associated with high order polynomial. In addition, the number of samples needed for the expansion, does not grow exponentially with the number of varying input parameters. For this reason, this method has been used for performing the sensitivity analysis.

The sensitivity of output parameters, as approximated by the PCE expansion, to variations in selected input parameters of the system, are obtained taking the derivatives of the expansion with respect to each input parameter. Three test cases are considered: a lightweight female single scull, a male quad scull, and a male coxless four. For all these cases detailed results that relate the effects of variations in rowers weights, amplitudes of exerted forces and cadence of rowing on mean boat speed and energy ratio, defined as the ratio of kinetic energy of the forward motion to that of the oscillatory motions, are presented. Such results should be useful in the design of rowing boats as well as in the training of rowers.

# Bibliography


[1] Havelock, T. H. (1963) Collected Papers, U. S. Government Printing Office, Washington, DC.

[2] Vugts, J. H. (1968) The hydrodynamic coefficients of swaying, heaving and rolling cylinders in a free surface. *International Shipbuilding Progress,* **15**, 251–276.

[3] Gerritsma, J. Motions, wave loads, and added resistance in waves for two wigley hull forms. Technical Report Rep. no. 804 Technical University of Delft (1988).

[4] Kleshnev, V. (2000) In *Proceedings of XVIII International symposium on biomechanics in sports, Hong Kong, Department of Sports Science and Physical Education. The Chinese University of Hong Kong* pp. 662–666.

[5] Kleshnev, V. (2006) In *Scientific proceedings. XXII International Symposium on Biomechanics in Sports, Salzburg* pp. 104–107.

[6] Alexander, F. H. (1925) In *Proceedings of the University of Durham Philosophical Society volume VI.*

[7] Atkinson, W. C. Modeling the dynamics of rowing. `www.atkinsopht.com/row/rowabstr.htm` (2002).

[8] Dudhia, A. The physics of rowing. `www.atm.ox.ac.uk/rowing/physics` (2001).

[9] vanHolst, M. On rowing. `http://home.hccnet.nl/m.holst/RoeiWeb.html` (2004).

[10] Lazauskas, L. A performance prediction model for rowing races. Technical Report L9702 Dept. of Appl. Math. University of Adelaide, Australia (1997).

[11] Elliott, B., Lyttle, A., and Burkett, O. The rowperfect ergometer: A training aid for on-water single scull rowing. `http://www.rowperfect.com.au` (2004).

[12] Rekers, C. J. N. Verification of the RowPerfect ergometer. `www.rowperfect.com/tek19021` (October, 1993).

[13] Mei, C. C. (1989) The applied dynamics of ocean surface waves, World Scientific Publishing, Singapore.

[14] Bertram, V. (2000) Practical ship hydrodynamics, Butterworth–Heinemann, Oxford (UK).

[15] Formaggia, L., Miglio, E., Mola, A., and Montano, A. (2008) A model for the dynamics of rowing boats. *Int. J. Numer. Methods Fluids,* **6**, 119–143.

[16] Mola, A. Models For Olympic Rowing Boats PhD thesis Dipartimento di Matematica, Politecnico di Milano (2009).

[17] Formaggia, L., Miglio, E., Mola, A., and Parolini, N. (2008) Fluid-structure interaction problems in free surface flows: Application to boat dynamics. *Int. J. Numer. Methods Fluids,* **56**, 965–978.

[18] Azcueta, R. (2002) Computation of turbulent free-surface flows around ships and floating bodies. *Ship Technology Research,* **49**, 46–69.

[19] NASA Man-system interaction standards – volume 1. Technical Report NASA-STD-3000 NASA Technical Standards (1995).

[20] Grassi, G. P., Santini, T., Lovecchio, N., Turci, M., Ferrario, V. F., and Sforza, C. (2005) Spatiotemporal consistency of trajectories in gymnastics: a three-dimensional analysis of flic-flac. *International Journal of Sports Medicine,* **26**, 134–138.

[21] Steer, R. R., McGregor, A. H., and Bull, A. M. J. (2006) A comparison of kinematiks and performance measures of two rowing ergometers. *Journal of Sports Science and Medicine,* **5**, 52–59.

[22] Karamcheti, K. (1966) Principles of ideal fluid aerodynamics, Wiley, New York (USA).

[23] Quarteroni, A., Sacco, R., and Saleri, F. (2000) Numerical mathematics, Springer Verlag, Heidelberg, Germany.

[24] Wilcox, D. C. (1998) Turbulence modeling for CFD, DCW Industries, La Cañada (USA).

[25] Boussinesq, J. (1987) Théorie de l'écoulement tourbillonnant et tumulteueux des liquides dans les lits rectilignesè grandes sectiones, Gautiers–Villars, Paris.

[26] Patankar, S. V., Karki, K. C., and Kelkar, K. M. Handbook of numerical fluid dynamics chapter Section 27:Finite volume method CRC Press (1966).

[27] Patankar, S. V. (1980) Numerical Heat Transfer and Fluid Flow, Taylor & Francis, London, United Kingdom.

[28] Adler, J. B. Coefficients for iinternational towing tank conference 1957 model-ship correlation line. Technical report David Taylor Model Basin Washington D.C. (1958).

[29] Pandini, S. Simulazione numerica della dinamica di imbarcazioni da canotaggio. Master's thesis Dipartimento di Matematica, Politecnico di Milano (2004).

[30] Newman, J. N. (1977) Marine Hydrodynamics, The MIT Press, Cambridge, Massachussets.

[31] Fossen, T. I. (2005) A nonlinear unified state-space model for ship maneuvering and control in a seaway. *International Journal of Bifurcation and Chaos,* **15**, 2717–2746.

[32] S oding, H. (1993) A method of accurate force calculation in potential flow. *Ship Technology Research,* **40**, 176–186.

[33] Newman, J. N. (1991) The quest for a three-dimensional theory of ship-wave interactions. *Philosophical Transactions: Physical Sciences and Engineering,* **334**, 213–227.

[34] Loève, M. (1978) Probability theory. Vol. II, Springer Verlag, Heidelberg, Germany.

[35] Reagan, M., Najm, H. N., Ghanem, R. G., and Knio, O. M. (2003) Uncertainty quantification in reacting flow simulations through non-intrusive spectral projection. *Combustion and Flame,* **132**, 545–555.

[36] Hosder, S., Walters, R. W., and Rafael, P. A non-intrusive polynomial chaos method for uncertainty propagation in cfd simulations. AIAA Paper 2006-891 AIAA (2006) 44th AIAA Aerospace Sciences Meeting and Exhibit, Reno, Nevada.

[37] Xiu, D. and Karniadakis, G. E. (2003) Modeling uncertainty in flow simulations via generalized polynomial chaos. *Journal of Computational Physics,* **187**, 137–167.

[38] Ghanem, R. G. and Spanos, P. D. (2003) Stochastic Finite Elements: A Spectral Approach, Dover Publications, Inc., .

[39] Abramowitz, M. and Stegun, I. A. (1964) Handbook of Mathematical Functions with Formulas, Graphs, and Mathematical Tables, Dover, New York.

[40] Helton, J. C. and Davis, F. J. (2000) In *Sensitivity Analysis* chapter 6 Sandia National Laboratories, Albuquerque, NM.

[41] Helton, J. C. and Davis, F. J. (2003) Latin hypercube sampling and the propagation of uncertainty in analyses of complex systems. *Reliability Engineering and System Safety,* **81**, 23–69.